ABSTRACT

Title of Dissertation: NON-EQUILIBRIUM PROPERTIES OF QUANTUM CHROMODYNAMICS ON THE LATTICE

Yukari Yamauchi
Doctor of Philosophy, 2022

Dissertation Directed by: Professor Thomas Cohen
Department of Physics

Heavy-ion collisions performed at the Large Hadron Collider and the Relativistic Heavy Ion Collider have given us a tremendous insight into both the equilibrium and non-equilibrium properties of strongly coupled nuclear matter. This thesis details two theoretical frameworks for addressing particularly the non-equilibrium nature of such nuclear systems governed by quantum chromodynamics.

Lattice QCD has offered non-perturbative access to observables in quantum chromodynamics. However, not much progress has been made in non-equilibrium calculations via lattice QCD compared to lattice QCD in equilibrium due to the so-called sign problem, stating that such calculations naively require a computational resource that scales exponentially with the size of the lattice. Quantum computing has the promise of performing first-principles simulations of the time-evolution of nuclear systems without such an exponential cost. This thesis details quantum algorithms for evaluating observables that are essential for understanding heavy-ion collisions: the parton distribution functions and the hydrodynamic transport coefficients.

Quantum simulation of nuclear system naively requires a large-scale quantum computer which is not available at the moment. Thus it is of practical importance to pursue methods to solve sign problems and expand the frontier of the classical lattice QCD calculation of non-equilibrium observables. The second topic of this thesis is a novel approach to address sign problems, which will be referred to as complex normalizing flows. This method belongs to a family of manifold deformation methods, a long-standing approach to alleviate sign problems. The applicability of complex normalizing flows to lattice calculations of our interest, non-equilibrium QCD, will be discussed. Given that complex normalizing flows are likely to solve sign problems in bosonic theories out of equilibrium, numerical algorithms based on machine learning to solve such sign problems in the framework of complex normalizing flows will be discussed.

NON-EQUILIBRIUM PROPERTIES OF QUANTUM CHROMODYNAMICS ON THE LATTICE

by

Yukari Yamauchi

Dissertation submitted to the Faculty of the Graduate School of the
University of Maryland, College Park in partial fulfillment
of the requirements for the degree of
Doctor of Philosophy
2022

Advisory Committee:
Professor Thomas Cohen, Chair/Advisor
Professor Kaustubh Agashe
Professor Paulo Bedaque
Professor Abolhassan Jawahery
Professor Alice Mignerey

Acknowledgments

I had five years full of the joy of physics in graduate school thanks to all of my collaborators. I am thankful to Scott Lawrence, Henry Lamm, Tom Cohen, Travis Dore, Isaac Long, Debora Mroczek, Jacquelyn Noronha-Hostler, Boris Gelman, and Yiming Cai for wonderful collaborations, which have made me who I am today.

If there is anything I have accomplished in the last decade, that could not happen without the aid and encouragement of the series of mentors. In chronological order, I am deeply indebted to Naoki Yamamoto, Richard Furnstahl, and my Ph.D. advisor Tom Cohen.

That this thesis exists is down to the collaboration with Scott Lawrence. I am grateful to him for the continuous advising and encouragement throughout the course of the PhD program.

I was very fortunate to have wonderful and thoughtful faculties around me to ask for discussion on physics and advice for life. I greatly appreciate Paulo Bedaque, Tom Cohen, Zohreh Davoudi, Daniel Harlow, Henry Lamm, and Paul Romatschke for their support.

Life at the University of Maryland could not be so fun without my fellow graduate students. I am especially thankful to Dan Zhang, Batoul Banihashemi, Yingyue Zhu, Yixu Wang, DinhDuy Vu, and Saurabh Kadam for our friendship. I also thank my laptops for giving me company and having executed all the hardest tasks in the past projects that made this thesis possible.

Lastly, for their ceaseless encouragement throughout my life, I am deeply grateful to my family: Miyoshi Osanai, Takatsugu Yamauchi, Miyuki Yamauchi, and Taizo Yamauchi.

Table of Contents

List of Tables

List of Figures

Chapter 1: Introduction

1.1 Overview

Quantum chromodynamics (QCD) is the first-principles description of the strong interaction governing the nature of quarks, hadrons and nuclei [1, 2]. Many aspects of nuclear matter have been explained by QCD, and yet there remains more to be explored. For example, asymptotic freedom of QCD [3, 4] is one of the characteristic features of QCD. It has justified the partonic picture of hadrons in high-energy collisions [5], which has enabled us to study the structure of hadrons from first-principles calculations in QCD. As another example, there have been numerous efforts to explain confinement of quarks and gluons in the hardons in the low-temperature phase of nuclear matter from QCD [6]. In the same vein, low-energy bound states of light nuclei have been studied from their fundamental constituents and interactions among them in various ways, *e.g.* [7, 8, 9, 10], and we expect that QCD will explain the structure of even larger nuclei. QCD is also expected to provide the equation of motion of nuclear matter. In particular, the time-evolution of strongly coupled quark matter with temperature around the confinement temperature $T_c = 200$ MeV is of great interest as that has experimentally observed. In experiment, such strongly interacting quark matter has been indirectly observed in heavy-ion collisions performed, for example, at the Large Hadron Collider (LHC) and the Relativistic Heavy Ion Collider (RHIC). Theoretical frameworks, utilizing both first-principles calculations and effective theories of QCD,

have been studied extensively in the last couple of decades to explain results from these experiments, *e.g.* [11, 12]. Particularly for strongly interacting nuclear matter observed at RHIC, it has been suggested that relativistic hydrodynamics provides a good effective description of the system theoretically. In all such frameworks, QCD serves as the guiding principle. Effective field theories are established while respecting certain symmetries in QCD, and their low energy constants (LECs) need to be derived from first-principles, *i.e.* quantum chromodynamics.

This thesis concerns the construction of first-principles calculations of QCD observables numerically on the lattice in the path integral formalism and Hamiltonian formalism. To begin, in the next section, I review the construction of QCD, its fundamental fields, symmetries, and the Lagrangian which will serve as the guiding principles when we develop methods to study strongly coupled QCD matter in the rest of this thesis. In Sec. 1.3, the "naive" QCD action in continuum spacetime will be discretized — a lattice field theory of QCD is constructed such that it will recover QCD in the continuum limit (*i.e.* in the limit of zero lattice spacing) after a proper renormalization. The energy-momentum tensor of the bosonic part of QCD, *i.e.*, the $SU(3)$ gauge theory will also be discretized to put on the lattice in Sec. 1.3.2, as a preparation for the later chapters. In Sec. 1.4, relativistic hydrodynamics is briefly introduced. Relativistic hydrodynamics serves as a powerful effective theory of QCD in the strongly coupled regime of QCD scanned by heavy-ion collisions. The purpose of this section is to derive relations between their LECs, the shear viscosity and bulk viscosity, and real-time correlators of the energy momentum tensor. Such relations will guide us towards the first-principles calculations of viscosities from QCD on the lattice as will be discussed in Sec. 2.5.

Quantum simulations of lattice gauge theories are discussed in Chapter 2. Quantum computers, once built, promise to be very powerful tools for performing non-perturbative QCD calculations

and revealing non-equilibrium aspects of QCD. After an overview of quantum simulations for QCD is given in Sec. 2.1, general methods for simulating gauge theories are discussed in Sec. 2.2 and Sec.2.3 based on [13]. As an example of such quantum simulations, quantum algorithms for computing important inputs to heavy-ion physics are discussed: the parton distribution functions and the hadronic tensor in Sec. 2.4 based on [14] and hydrodynamic transport coefficients in Sec. 2.5 based on [15].

Quantum algorithms discussed in Chapter 2 reveal the reality — a large-scale quantum computer, which is not available at the moment, will be required to perform quantum simulations which can give us insights into non-perturbative nature of QCD. While we wait for such a large-enough quantum computer to be built, it is of practical importance to push the frontier of lattice QCD calculations on classical computers. Lattice QCD calculations of the non-equilibrium properties of QCD possess the so-called sign problem, which means that an exponentially scaling (in the size of the lattice) computational resource is required for such lattice calculations. Chapter 3 is devoted to investigate methods for solving sign problems in QCD. Firstly, Sec. 3.1 introduces and defines the real-time sign problem which appears in Minkowski lattice QCD calculations, which is probably essential for studying aspects of QCD out of equilibrium. The so-called manifold deformation method [16], a long-standing method to alleviate sign problems, is reviewed in Sec. 3.2. In Sec. 3.3, we introduce another view of the manifold deformation method — the *complex normalizing flows* [17]. The applicability of manifold deformation methods, and equivalently complex normalizing flows to various sign problems, especially the real-time sign problem, will be discussed in Sec. 3.4 with examples. Finally in Sec. 3.5, numerical methods based on machine learning to address sign problems in the framework of complex normalizing flows will be demonstrated.

To conclude this thesis, in Chapter 4, I will give an overview of future work that will follow from projects described in Chapter 2 and Chapter 3.

1.2 Quantum chromodynamics

The degrees of freedom in QCD are, first of all, quarks. Let us denote a quark field at spacetime x as $\psi(x)$. Each quark field has three indices: Dirac index, color index (which will be denoted with a, b), and flavor index f. The naive kinetic Lagrangian of three Dirac fermions $\mathcal{L} = \sum_{f=1}^{3} \bar{\psi}_f \left(i\gamma^\mu \partial_\mu - m\right) \psi_f$ is invariant under a global $SU(3)$ transformation:

$$\psi_a \to \psi'_a = U(\vec{\alpha})_{ab}\psi_b, \qquad U(\alpha) = e^{i\alpha^i T^i} \tag{1.1}$$

where T^i $(i = 1, \cdots, 8)$ denote eight generators of the $SU(3)$ group in the fundamental representation called Gell-Mann matrices. Generators T^i are orthonormalized as

$$\mathrm{Tr}\left(T^i T^j\right) = \delta_{ij}, \quad i, j = 1, \cdots, 8\,. \tag{1.2}$$

Each element $U(\vec{\alpha}) \in SU(3)$ is parameterized by the eight real numbers denoted as $\vec{\alpha} = (\alpha^1, \cdots, \alpha^8)$.

We now proceed and impose a local gauge invariance on the Lagrangian of Dirac fermions. In other words, the naive Lagrangian will be modified so that it will be invariant under a spacetime-dependent rotation

$$\psi(x) \to \psi'(x) = U(\vec{\alpha}(x))\psi(x) \tag{1.3}$$

Note that the parametrization of elements of the $SU(3)$ group is now spacetime dependent, i.e.,

$\vec{\alpha}(x)$. For the Lagrangian to achieve such a local symmetry, its kinetic term, $\bar{\psi}\,\gamma^{\mu}\,\partial_{\mu}\,\psi$, needs a "comparator" of fields at different points in spacetime called the Wilson line:

$$W_P(x,y) = P\left[\exp\left(ig_s\int_y^x dz^{\mu}\ A^i_{\mu}(z)T^i\right)\right]. \tag{1.4}$$

Here the gauge fields $A_{\mu} = A^i_{\mu}T^i$ are introduced. The index μ denotes the direction in spacetime. In the rest of this thesis, when a gauge field is written without a superscript i, that gauge field is contracted with the Gell-Mann matrices. The strong coupling constant is denoted as g_s. The path-ordered operator P is inserted because the generators T^i at different points do not commute. Under a local gauge transformation, the Wilson line transforms as

$$W_P(x,y) \to W'(x,y) = U^{-1}(x)W_P(x,y)U(y) = e^{-i\alpha^i(x)T^i}W_P(x,y)e^{i\alpha^i(y)T^i} \tag{1.5}$$

so that the covariant derivative

$$D\psi(x) = \lim_{a\to 0}\frac{\psi(x+a) - W(x+a)\psi(x)}{a} \tag{1.6}$$

transforms as $D_{\mu}\psi(x) \to U(x)D_{\mu}\psi(x)$. The kinetic term of quarks, when constructed with the covariant derivative as $\bar{\psi}(x)D\psi(x)$, is locally gauge invariant. The infinitesimal expansion of the Wilson line gives the covariant derivative in terms of local gauge fields as

$$D_{\mu} = \partial_{\mu} - igT^iA^i_{\mu}. \tag{1.7}$$

and thus the gauge fields should transform in the following way:

$$A^i_\mu(x) \to A^i_\mu(x) + \frac{1}{g}\partial_\mu \alpha^i(x) + i f^{ijk}\alpha^j(x) A^k_\mu(x) \; . \tag{1.8}$$

Here the structure constants f^{ijk} are defined as $[T^i, T^j] = i f^{ijk} T^k$. The covariant derivative helps us construct a kinetic term of the gauge fields. Let us introduce the field strength tensor $F^a_{\mu\nu}$ as

$$F_{\mu\nu} = F^i_{\mu\nu} T^i = \frac{i}{g}\left[D_\mu, D_\nu\right] = \partial_\mu A_\nu - \partial_\nu A_\mu + ig\left[A_\mu, A_\nu\right] \tag{1.9}$$

which transforms in the adjoint representation as $F_{\mu\nu}(x) \to U(x) F_{\mu\nu}(x) U^{-1}(x)$. To summarize, with the kinetic term $-\frac{1}{4}\,\mathrm{Tr}\left[F_{\mu\nu}F^{\mu\nu}\right]$, a locally $SU(3)$ invariant Lagrangian density of quarks and gluons is constructed as

$$\mathcal{L} = -\frac{1}{4} F^i_{\mu\nu} F^{\mu\nu,i} + \sum_{a,b=1}^{3} \bar{\psi}_a \left(i\gamma^\mu \partial_\mu \delta_{ab} + g\gamma^\mu A^i_\mu T^i_{ab} - m\delta_{ab} \right) \psi_b \tag{1.10}$$

where the color indices a, b are explicitly written down. The corresponding Hamiltonian of QCD can be derived by starting from the QCD Lagrangian above and employing the Legendre transformation or the transfer matrix as will be discussed in Sec. 2.3. The Lagrangian and Hamiltonian provide us with different formalisms to compute observables of our interests in QCD. The path integral defined with the Lagrangian has been the major formalism to address observables in the context of lattice QCD on a classical computer. In the next section, I introduce the path integral formalism of QCD and its discretization on the lattice.

1.3 Lattice quantum chromodynamics

1.3.1 Path integral on the lattice

Path integrals [18] provide us a formalism to compute expectation values of observables in a quantum theory by taking all the possible "paths" for the quantum fields in spacetime. To build the most general form of the path integral, let us suppose that we would like to compute the thermal expectation value (at an inverse temperature β) of a Hermitian observable $\mathcal{O}(t_0)$ at time $t = t_0$ in QCD. Starting from the Hamiltonian formulation with the QCD Hamiltonian $\hat{H}$, we derive the path integral as

$$\langle \mathcal{O}(t_0) \rangle = \mathrm{Tr}\left[e^{-\beta \hat{H}} \mathcal{O}(t_0)\right] = \mathrm{Tr}\left[e^{-\beta \hat{H}} e^{i\hat{H}t_0} \mathcal{O} e^{-i\hat{H}t_0}\right] \tag{1.11}$$

$$= \int \mathcal{D}\left[\bar{\psi}, \psi, A\right](x) e^{-S} \mathcal{O}(\bar{\psi}(t_0), \psi(t_0), A(t_0)). \tag{1.12}$$

Here the configuration of quark fields $\bar{\psi}$ and ψ should be anti-periodic and the gauge fields A should be periodic due to the trace in the first line. "Time" t can be real (for the real-time evolution) or imaginary to introduce the finite temperature β. The contour that time t takes in its complex plane is called the Schwinger-Keldysh contour, and its shape depends on how one orders the 'time-evolution' in the first line in Eq. (1.11). In the order of the equation above, the contour is the "L contour" as is shown in Figure 1.1. Another contour shown in Figure 1.1 is the "S contour", which corresponds to ordering the time evolution as $\mathrm{Tr}\left[e^{-\frac{\beta}{2}H} e^{i\hat{H}t_0} \mathcal{O} e^{-\frac{\beta}{2}H} e^{-i\hat{H}t_0}\right]$. When on the imaginary time axis, the action S should be the Euclidean action of QCD. When on the real-time axis, the weight should be e^{iS} instead with the Minkowski action of QCD.

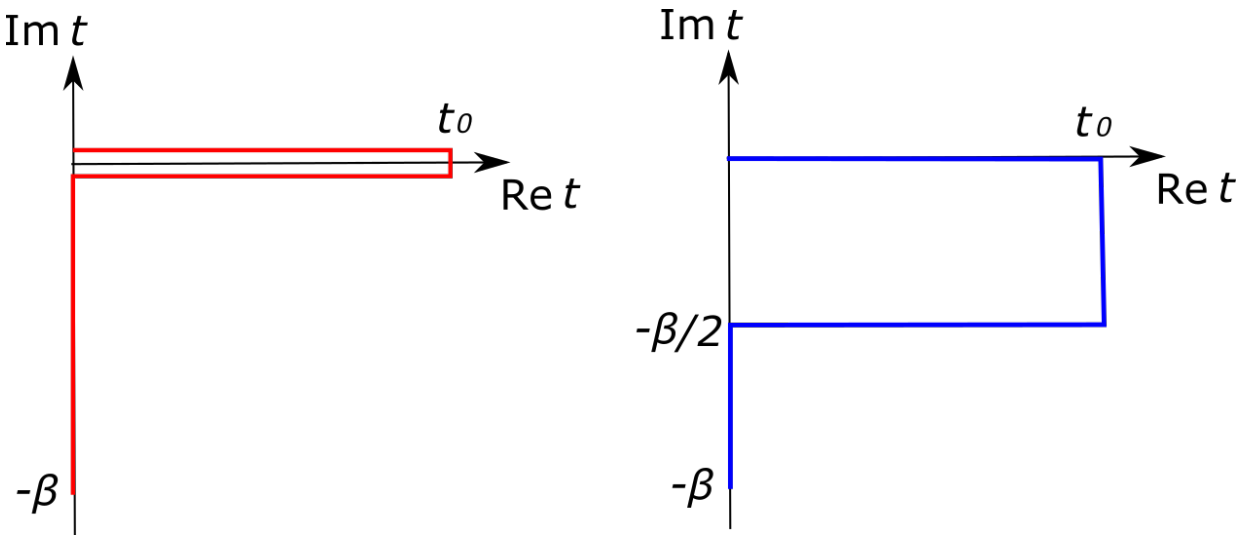

Figure 1.1: Schwinger-Keldysh L contour on the left and S contour on the right.

Lattice QCD is a non-perturbative numerical method to compute the path integral — a very high-dimensional integral — without any perturbative expansions [6, 19, 20, 21]. To evaluate the path integral numerically using a classical computer, we first need to regulate the theory to only a finite number of degrees of freedom. Thus, we discretize space and time via a lattice. On the lattice, quark fields live on lattice sites. Gauge fields, which connect quark fields to achieve local gauge symmetry, are represented by links. In the rest of the thesis, I denote the gauge link starting at site n and extending in the μ direction as $U_{n,\mu}$, and let it represent the Wilson line on the link:

$$U_{n,\mu} = \exp\left(ig_s A^i_\mu(n) T^i\right). \tag{1.13}$$

Using gauge links and quark fields on sites, we construct the action of QCD on the lattice, which becomes the naive continuum action in Eq. (1.10) in the continuum limit where we take the lattice spacing to zero: $a \to 0$. Thus the QCD action on the lattice should preserve the local gauge symmetry. To construct such an action, it is useful to study the smallest local and gauge-

invariant object on the lattice. One such object that is constructed purely by gauge links is the trace of a plaquette $P_{\mu\nu}(n)$ shown in Figure 1.2:

$$P_{\mu\nu}(n) = U_{n,\mu} U_{n+\hat{\mu},\nu} U^{\dagger}_{n+\hat{\nu},\mu} U^{\dagger}_{n,\nu} \ . \tag{1.14}$$

To see what this plaquette represents, we express the plaquette in terms of gauge fields A^i_μ at the center of the plaquette $x_0 = n + \hat{\mu}/2 + \hat{\nu}/2$. Gauge fields on lattice sites on the plaquette are written via the Taylor expansion in lattice spacing a_μ (the lattice spacing in $\hat{\mu}$ direction) as

$$A^i_\mu(n) = A^i_\mu(x_0) - \frac{a_\mu}{2}\partial_\mu A^i_\mu(x_0) - \frac{a_\nu}{2}\partial_\nu A^i_\mu(x_0) + O(a^2) \tag{1.15}$$

and so on. The plaquette is written in terms of the field $A(x_0)$ at the center of the plaquette x_0 as [22]

$$\begin{aligned} P_{\mu\nu}(n) &= \exp\left(ig_s A_\mu(n)\right) \exp\left(ig_s A_\nu(n+\hat{\mu})\right) \exp\left(-ig_s A_\mu(n+\hat{\nu})\right) \exp\left(-ig_s A_\nu(n)\right) \\ &= \exp\left(ig_s a_\mu a_\nu F_{\mu\nu}(x_0) + O(a^4)\right) \end{aligned} \tag{1.16}$$

By expanding with the lattice spacing a, the plaquette bocomes

$$P_{\mu\nu}(n) = 1 + ig_s a_\mu a_\nu F_{\mu\nu}(x_0) - \frac{g_s^2 a_\mu^2 a_\nu^2}{2} F_{\mu\nu}(x_0)^2 + O(a^6) \ . \tag{1.17}$$

Therefore, by taking the real part of the plaquette:

$$\mathrm{Tr}\left[F_{\mu\nu}(x_0)^2\right] = \frac{2}{g_s^2 a_\mu^2 a_\nu^2} \,\mathrm{Re}\,\mathrm{Tr}[1 - P_{\mu\nu}(n)] + O(a^2), \tag{1.18}$$

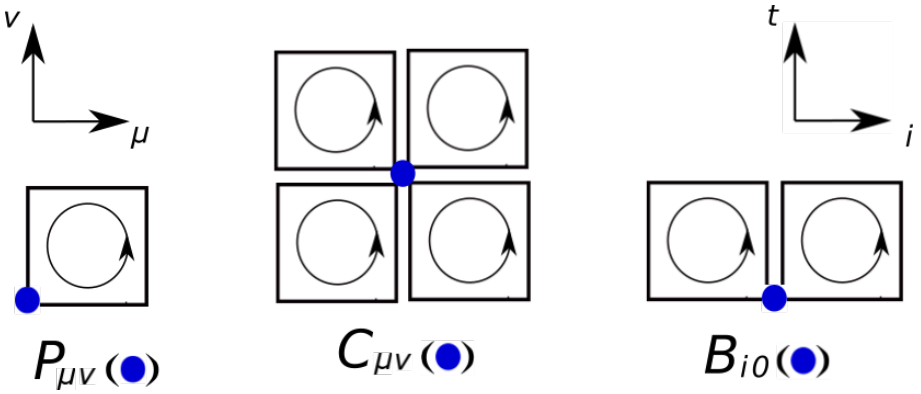

Figure 1.2: Plaquette, clover, and half-clover on the lattice.

we obtain the kinetic term of gauge fields in the naive continuum action Eq. (1.10) at the center of the plaquette x_0. Using Eq. (1.18), the Wilson gauge action [6] in Minkowski spacetime:

$$S_W = \sum_{t=1}^{N_t} K(t) + V(t) \tag{1.19}$$

$$K(t) = \sum_n \sum_i \frac{a}{g_s^2 a_0} \operatorname{Re}\operatorname{Tr}\left[1 - P_{0i}(n,t)\right] \tag{1.20}$$

$$V(t) = \sum_n \sum_{i<j} \frac{a_0}{g_s^2 a} \operatorname{Re}\operatorname{Tr}\left[P_{ij}(n,t)\right] \tag{1.21}$$

approximates kinetic term of gauge fields in the continuum Lagrangian Eq. (1.10) up to $O(a^2)$ discretization errors. Here a denotes spatial lattice spacing assuming that the lattice is spatially isotropic. Lattice spacing in the time direction is denoted as a_0. Note that the constant term, the identity matrix in the trace of Eq. (1.18) was dropped for the potential term V in the Wilson gauge action.

The fermionic part of the Lagrangian Eq. (1.10) can also be naively written as

$$S_F = a^3 a_0 \sum_n \bar{\psi}(n) \left(\sum_{\mu=1}^{4} i\gamma_\mu \frac{U_\mu(n)\psi(n+\hat{\mu}) - U_{-\mu}(n)\psi(n-\hat{\mu})}{2a} + m\psi(n) \right) \tag{1.22}$$

Therefore the Dirac matrix $D(n|m)$ on the lattice is naively

$$D(n|m)_{\alpha i,\beta j} = \sum_{\mu=1}^{4} i\left(\gamma_\mu\right)_{\alpha\beta} \frac{U_\mu(n)_{ij}\delta_{n+\hat{\mu},m} - U_{-\mu}(n)_{ij}\delta_{n-\hat{\mu},m}}{2a} + m\delta_{\alpha\beta}\delta_{ij}\delta_{nm} \tag{1.23}$$

where lattice sites m, n, Dirac indices α, β, and color indices a, b are explicitly written. This naive Dirac matrix has the so-called fermion doubling problem [23] which means that the Dirac matrix has unphysical poles. There are several well-established methods to get rid of such unphysical modes such as Wilson fermions [6], Kogut-Susskind staggered fermions [24], and domain wall fermions [25].

After the treatment of the fermion doubling problem, it is convenient for us to integrate out fermions in the path integral using the Gaussian integral of Grassmann numbers to obtain a path integral only in terms of gauge fields, for example for the partition function as

$$Z = \int \mathcal{D}\left[U\right] \det\left[D\right] e^{-S_W[U]} \,. \tag{1.24}$$

Here the matrix D is the Dirac matrix with a chosen method to treat the fermion doubling problem. The size of the Dirac matrix scales linearly with the size of the lattice, making the lattice QCD calculation much more expensive than that of pure Yang-Mills theory.

Having written down the path integral only in terms of gauge fields, we now proceed and evaluate the path integral numerically. Since the integral is very high dimensional, it is practical to utilize Monte Carlo methods with importance sampling. For a purely thermal calculation (no real-time evolution), the weight e^{-S} is always real and positive, and thus can be regarded as the probability distribution function of the configuration of the gauge fields. One samples N_s

configurations of gauge links across the lattice from the distribution function e^{-S} via Markov chain Monte Carlo (MCMC) methods. Using the set of N_s gauge configurations, we evaluate the expectation value of the observable $\mathcal{O}$ by computing the observable with each configuration A_n and summing,

$$\langle \mathcal{O} \rangle = \frac{1}{N_s} \sum_{n=1}^{N_s} \mathcal{O}(A_n) \ . \tag{1.25}$$

So far the lattice calculation is done on a lattice with a finite volume and a lattice spacing a for which we do not know the physical number. In the end, the infinite volume and continuum limits should be taken. In particular, the taking of the continuum limit $a \to 0$ plays the role of an ultraviolet renormalization. An appropriate tuning of lattice parameters, such as the mass m and the coupling constant g, should be performed to maintain the low-energy physics of lattice QCD while taking the continuum limit.

Euclidean lattice QCD has successfully calculated many aspects of QCD such as the equation of state at vanishing baryon chemical potential [26]. However, when we include the real-time evolution, we encounter the factor e^{iS}, which will introduce the so-called real-time sign problem. When the baryon chemical potential is finite, the Dirac determinant $\det D$ causes the finite-density sign problem [27]. These sign problems have prevented lattice QCD from computing the equation of state at large baryon chemical potential and non-equilibrium properties of QCD. Chapter 3 is devoted to the discussion of potential solutions to the real-time sign problem.

1.3.2 Yang-Mills energy momentum tensor on the lattice

In this section, we introduce the energy-momentum tensor (EMT) of Yang-Mills theory on the lattice [28]. As will be discussed in Sec. 1.4, the energy momentum tensor plays the central

role in the construction of hydrodynamics and so as the first-principles calculation of transport coefficients in hydrodynamics. Therefore it is essential that one understands the discretization of the EMT of QCD on the lattice. In the action formulation, the EMT is the Noether's currents for translational symmetry in space and time. For the Yang-Mills theory in the naive continuum, the EMT takes the form

$$T_{\mu\nu} = \frac{1}{4} g_{\mu\nu} \operatorname{Tr}\left[F_{\alpha\beta}F^{\alpha\beta}\right] - \operatorname{Tr}\left[F_{\mu\alpha}F^{\alpha}_{\nu}\right]. \tag{1.26}$$

up to the trace anomaly. The EMT is manifestly gauge-invariant and Hermitian.

On the lattice, each term in Eq. (1.26) should be discretized via a combination of plaquettes to preserve the local gauge invariance. At the same time, lattice observables should be constructed such that they approximate the EMT in the continuum on a site up to a desired discretization error $O(a^n)$. Let us begin with the first term, which is identical to the terms in the Wilson gauge action Eq (1.19). In the last section at Eq. (1.18), we saw that the plaquette, when taken the trace as $\operatorname{Re}\operatorname{Tr}\left[1 - P_{\mu\nu}(n)\right]$, approximates the field strength at the center of the plaquette, $\operatorname{Tr}\left[F_{\mu\nu}(x_0)^2\right]$, up to $O(a^2)$ error. Therefore the local observable $\operatorname{Tr}\left[F_{\mu\nu}(n)^2\right]$ on a lattice site n is approximated up to $O(a)$ discretization errors by

$$\operatorname{Tr}\left[F_{\mu\nu}(n)^2\right] = \frac{2}{g_s^2 a_\mu^2 a_\nu^2} \operatorname{Re}\operatorname{Tr}[1 - P_{\mu\nu}(n)] + O(a) \tag{1.27}$$

To improve the approximation up to $O(a^2)$, we simply take the average of four plaquettes around the site n:

$$\operatorname{Tr}\left[F_{\mu\nu}(n)^2\right] = \sum_{x=0,1}\sum_{y=0,1} \frac{1}{2g_s^2 a_\mu^2 a_\nu^2} \operatorname{Re}\operatorname{Tr}[1 - P_{\mu\nu}(n - x\hat{\mu} - y\hat{\nu})] + O(a^2). \tag{1.28}$$

In the context of quantum simulation, we have two lattice spacings: the spatial lattice spacing a and the Trotterization step a_0. As we traditionally take the Hamiltonian limit $a_0 \to 0$ first in quantum simulations, it is safe to leave the discretization error in time direction at the linear order and improve the discretization only in the spacial lattice spacing a up to $O(a^2)$. Thus for the terms involving gauge links in the time direction, we take the average of two plaquettes in the following way:

$$\mathrm{Tr}\left[F_{oi}(n)^2\right] = \sum_{x=0,1} \frac{1}{g_s^2 a_\mu^2 a_\nu^2} \mathrm{Re}\,\mathrm{Tr}[1 - P_{\mu\nu}(n - x\hat{i})] + O(a^2, a_0). \tag{1.29}$$

This discretization scheme saves us from constructing time-non-local observables of the form

$$\mathrm{Tr}\left[F_{\mu\nu}(n)^2\right] = \sum_{x=0,1} \sum_{y=0,1} \frac{1}{2g_s^2 a_0^2 a_i^2} \mathrm{Re}\,\mathrm{Tr}[1 - P_{0i}(n - x\hat{t} - y\hat{i})] + O(a^2). \tag{1.30}$$

whose corresponding operators are spatially non-local in the Hamiltonian formulation.

The disctretization of the second term in the energy-momentum tensor Eq. (1.26) requires the disctretization of $F_{\mu\nu}$ itself, which can be done again by combining certain plaquettes. The most naive discretization of $F_{\mu\nu}$ is

$$F_{\mu\nu}^N(n) = -\frac{i}{2g_s a_\mu a_\nu} \left(P_{\mu\nu}(n) - P_{\mu\nu}^\dagger(n)\right) + O(a) \tag{1.31}$$

which is correct up to an $O(a)$ error. An improvement of discretization to $O(a^2)$ order can be done again by taking the average of four plaquettes and construct the so-called "clover"

$$C_{\mu\nu}(n) = \frac{1}{4}\left[P_{\mu,\nu} + P_{\nu,-\mu} + P_{-\mu,-\nu} + P_{-\nu,\mu}\right](n). \tag{1.32}$$

as show in Figure 1.2. By combining clovers in the same way as Eq. (1.31) we obtain the lattice expression for the second term in Eq. (1.26) as

$$F^C_{\mu\nu}(n) = -\frac{i}{2g_s a_\mu a_\nu}\left(C_{\mu\nu}(n) - C^\dagger_{\mu\nu}(n)\right) \ . \tag{1.33}$$

that approximates $F_{\mu\nu}(n)$ up to $O(a^2)$ discretization errors. Again in the context of quantum simulation, it is convenient to ignore the discretization error from finite a_0 in the Hamiltonian limit. This motivates us to define "half-clovers" B (shown in Figure 1.2), which is the average of two plaquettes in the remaining spatial direction:

$$B_{i0}(n) = \frac{1}{2}\left(P_{i0}(n) + P_{0(-i)}(n)\right) \ . \tag{1.34}$$

By combining these half-clovers, we obtain the discretization of F_{0i} which is correct up to $O(a_0, a^2)$ error as

$$F^B_{i0}(n) = \frac{-i}{2g_s a_0 a}\left(B_{i0}(n) - B^\dagger_{i0}(n)\right). \tag{1.35}$$

We can further improve the discretization scheme so that the lattice EMT observables approximate theEMT in the continuum up to a higher-order $O(a^n)$ discretization error, by combining larger plaquettes as were constructed in [22].

1.4 Relativistic hydrodynamics

1.4.1 Hydrodynamics of ideal fluid

Since the first attempt to simulate the hot quark-gluon-plasma seen in heavy-ion collisions with relativistic hydrodynamics [29, 30, 31, 32], its transport coefficients, the shear viscosity and bulk viscosity, have been a key to understanding the non-equilibrium nature of dense quark-gluon plasma. From the hydrodynamic simulation of heavy-ion collisions fit to the experimental result, especially the elliptic flow [33], the ratio of the shear viscosity η to the entropy density s is estimated to be [34]

$$\frac{1}{4\pi} \lesssim \frac{\eta}{s} \lesssim \frac{2.5}{4\pi} \qquad \text{for} \qquad T_c \leq T \leq 2T_c \,. \tag{1.36}$$

The estimate is very close to the KSS bound $\eta/s = 1/4\pi$, a conjectured lower bound on the value of η/s for a wide class of theories [35]. While their are still discussions on the applicability of the KSS bound (see [36] and references therein), the strongly coupled quark-gluon plasma is called one of the"most nearly perfect liquid" due to the smallness of η/s. These transport coefficients are the low energy constants of hydrodynamics, meaning that they are in principle derivable from first-principles, i.e., QCD and be input to the hydrodynamic description of QCD.

The regime of QCD in which relativistic hydrodynamics serves as an effective theory is the strongly coupled regime of QCD. Thus non-perturbative methods, such as lattice QCD, are required to evaluate hydrodynamic transport coefficients. Unfortunately, at the moment, there is no viable non-perturbative methods to address these LECs. The main theme of this thesis in later chapters is the construction of lattice QCD methods for computing such non-equilibrium properties of QCD. To prepare for those chapters, in this section, we briefly review the basics of relativistic hydrodynamics as an effective theory, derive equations of motion for

the effective fields: relativistic Euler equations and Navier-Stokes equations, and come to the relations between LECs and correlators of the energy momentum tensor. Such relations will be used in lattice QCD methods to evaluate transport coefficients as will be discussed in Section 2.5. Almost entire discussion in this section is based on Chapter. 2 of the book "*Relativistic Fluid Dynamics In and Out of Equilibrium*" by P. Romatschke and U. Romatschke [37]. Following the convention chosen in the book, in this section, the metric tensor in Minkowski spacetime is chosen to be mostly-plus:

$$g_{\mu\nu} = \text{diag}(-1,\ 1,\ 1,\ 1)\ , \tag{1.37}$$

and we consider specifically $3+1$-dimensions.

In a relativistic theory, Lorentz symmetry requires the following conservation laws:

$$\nabla_\mu T^{\mu\nu} = 0\ . \tag{1.38}$$

Thus central steps in building relativistic hydrodynamics is to construct the energy momentum tensor $T_{\mu\nu}$ in terms of the hydrodynamic fields, yet to be chosen, while respecting Lorentz symmetry. As we are interested in the long-wave-length behavior of the system, we construct the EMT order by order in a derivative expansion (with respect to space and time) of the hydrodynamic fields. In fact, in momentum space, these derivatives pull down factors of the momentum scale k^n for nth order derivatives and the EMT will be written as the small k expansion. Let us denote the nth order term in the EMT as $T^{\mu\nu}_{(n)}$ such that the EMT will be constructed as

$$T^{\mu\nu} = T^{\mu\nu}_{(0)} + T^{\mu\nu}_{(1)} + \cdots\ . \tag{1.39}$$

When constructing the EMT, we should do so such that the symmetry in the original theory, i.e., Lorentz symmetry, is preserved at each order n. Thus, the task is, at each order, write down all possible combinations of the hydrodynamic fields with the right number of derivatives. When combining such terms to build $T^{\mu\nu}_{(n)}$, coefficients (LECs) need to be introduced. These are the transport coefficients defined by the construction of relativistic hydrodynamics, and their physical meaning will be given by solving the resulting equation of motion Eq. (1.38). In the following, we work out the expressions for $T^{\mu\nu}_{(0)}$ and $T^{\mu\nu}_{(1)}$.

To start the costruction of the zeroth order EMT, let us introduce a Lorentz scalar ϵ, Lorentz vector u^μ, and the metric tensor $g_{\mu\nu}$ in Eq. (1.37). We choose the Lorentz vector to be the time-like eigenvector of the EMT, $\langle T^{\mu\nu}\rangle$, and Lorentz scalar be the corresponding eigenvalue:

$$\langle T^{\mu\nu}\rangle u_\nu = -\epsilon u^\mu \tag{1.40}$$

Here the expectation value of the EMT is that of the underlying quantum system in equilibrium in Minkowski spacetime. The eigenvector is normalized to be $u^\mu u_\mu = -1$.

By writing down all possible terms with no derivatives while respecting Lorentz symmetry, one finds that $T_{\mu\nu}$ takes the following general form:

$$T^{(0)}_{\mu\nu} = f_1(\epsilon) u_\mu u_\nu + f_2(\epsilon) g_{\mu\nu} \tag{1.41}$$

where $f_1(\epsilon)$ and $f_2(\epsilon)$ are scalar function of the Lorentz scalar ϵ. So far none of coefficients $f_1(\epsilon), f_2(\epsilon)$ have been identified. Now let us perform a Lorentz boost and bring the EMT to the local rest frame. The Lorentz vector is $u^\mu = (1, 0, 0, 0)$ in the local rest frame and thus the EMT

takes the form

$$T^{\mu\nu}_{(0),\mathrm{LRF}} = \mathrm{diag}\left(f_1(\epsilon) - f_2(\epsilon),\ f_2(\epsilon),\ f_2(\epsilon),\ f_2(\epsilon)\right). \tag{1.42}$$

In the local rest frame, the expectation value of the EMT is

$$\langle T_{\mu\nu}\rangle_{\mathrm{LRF}} = \mathrm{diag}\left(\epsilon, P, P, P\right) \tag{1.43}$$

where ϵ and $P(\epsilon)$ are the equilibrium energy density and pressure to be computed from the underlying quantum theory. The coefficients $f_1(\epsilon)$ and $f_2(\epsilon)$ are identified by matching Eq. (1.42) and Eq. (1.43). The result is $f_1(\epsilon) = \epsilon + P(\epsilon)$, $f_2(\epsilon) = P(\epsilon)$. Thus the energy momentum tensor of zeroth order relativistic hydrodynamics is

$$T^{(0)}_{\mu\nu} = (\epsilon + P)\, u^\mu u^\nu + P\, g^{\mu\nu} \tag{1.44}$$

where the Lorentz scalar ϵ is identified as the local energy density. The Lorentz vector u_μ can be identified as the local fluid velocity. In addition to these hydrodynamic fields, we introduced another Lorentz scalar P which is identified as the equilibrium pressure. This equation of state $P(\epsilon)$ is not fixed in the framework of hydrodynamics. The equation of state is in fact the "zeroth order transport coefficient", which needs to be computed from the underlying quantum theory or extracted from experiment and be input to the hydrodynamic description above.

The equation of motion for ideal fluid dynamics,

$$\nabla_\mu T^{\mu\nu}_{(0)} = 0\,, \tag{1.45}$$

is the relativistic Euler equation. To derive it, it is convenient to introduce the following tensor

$$\Delta^{\mu\nu} = g^{\mu\nu} + u^\mu u^\nu \tag{1.46}$$

which is orthogonal to the vector u_μ. The vector u^μ and tensor $\Delta^{\mu\nu}$ project the equation of motion Eq. (1.45) separately into time-like and space-like components. In fact, in the local rest frame, $u^\mu_{\text{LRF}} = (1, 0, 0, 0)$ and $\Delta^{\mu\nu}_{\text{LRF}} = \text{diag}(0, 1, 1, 1)$. The time-like component of the Euler equation is

$$u_\nu \nabla_\mu T^{(0)}_{\mu\nu} = -\left(\epsilon + P\right) \nabla_\mu u^\mu - u^\mu \nabla_\mu \epsilon = 0 \, . \tag{1.47}$$

where $u_\mu \nabla_\nu u^\mu = 0$ was used. The space-like projection reads

$$\Delta_{\mu\alpha} \nabla_\mu T^{(0)}_{\mu\nu} = \left(\epsilon + P\right) u^\mu \nabla_\mu u_\alpha + \Delta_{\mu\alpha} \nabla_\mu P = 0 \, . \tag{1.48}$$

Let us introduce short-hand notations of the projection of the derivatives

$$D_h \equiv u^\mu \nabla_\mu, \qquad \nabla^\alpha_\perp \equiv \Delta^{\mu\alpha} \nabla_\mu \, . \tag{1.49}$$

The second term in Eq. (1.48) can be written with the energy density using $c_s(\epsilon) \equiv \sqrt{\frac{\partial P}{\partial \epsilon}}$ and thus Eq. (1.47) and Eq. (1.48) become

$$(\epsilon + P) \nabla_\mu u^\mu + D_h \epsilon = 0, \qquad \left(\epsilon + P\right) D_h u^\alpha + c_s^2 \nabla^\alpha_\perp \epsilon = 0 \, . \tag{1.50}$$

In the non-relativistic limit: $|\vec{v}| \ll 1$ and $P \ll \epsilon$, equations become the continuity equation for the

time-like projection and non-relativistic Euler equation for the space-like projection respectively:

$$\partial_t \epsilon + \vec{v} \cdot \partial \epsilon + \epsilon \partial \cdot \vec{v} = 0, \qquad \epsilon \partial_t \vec{v} + \epsilon \vec{v} \cdot \partial \vec{v} + \partial P = 0 \ . \tag{1.51}$$

These equations govern the time evolution of the underlying quantum system in the ideal hydrodynamic description.

1.4.2 Hydrodynamics of nearly ideal fluid

The goal of this section on relativistic hydrodynamics is to derive expressions for correlation functions of the EMT evaluated on a thermal state such as

$$\langle T^{01}(t,k) T^{01}(0,k) \rangle \propto e^{-\frac{\eta k^2}{\epsilon} t} \ , \tag{1.52}$$

which tell us how one computes the first order hydrodynamic coefficients, the shear viscosity η and the bulk viscosity ζ, from the underlying quantum theory. This equation tells us about how the fluid responds to a small perturbation by T^{01}. To study such a linear response, we need to consider the system slightly out of equilibrium. The energy momentum tensor should encode the slight change in ϵ, u^μ over space and time by including the next order EMT $T^{\mu\nu}_{(1)}$. Within the first-order hydrodynamic effective theory, the hydrodynamic fields are again introduced as the time-like eigenvector and its eigenvalue of the $T_{\mu\nu}$

$$u_\mu \langle T^{\mu\nu} \rangle = -\epsilon u^\nu \tag{1.53}$$

where the expectation value of $T^{\mu\nu}$ is now that of the underlying quantum theory slightly out of equilibrium. Since $T^{\mu\nu}_{(1)}$ is a symmetric tensor, we only need to list symmetric two-rank tensor as candidate terms. These are

$$\Delta_{\mu\nu}\nabla^{\perp}_{\lambda}u^{\lambda} \quad \text{and} \quad \nabla^{\perp}_{(\mu}u_{\nu)} = \frac{1}{2}\left(\nabla^{\perp}_{\mu}u_{\nu} + \nabla^{\perp}_{\nu}u_{\mu}\right). \tag{1.54}$$

For later convenience, we introduce two linear combinations of these two terms:

$$\Delta^{\mu\nu}\nabla^{\perp}_{\lambda}u^{\lambda} \quad \text{and} \quad \sigma^{\mu\nu} = 2\nabla^{<\mu}_{\perp}u^{\nu>} - \frac{2}{3}\Delta^{\mu\nu}\nabla^{\perp}_{\lambda}u^{\lambda} \tag{1.55}$$

The second term $\sigma_{\mu\nu}$ is traceless, *i.e.*, $g_{\mu\nu}\sigma^{\mu\nu} = 0$. We now write down the first-order EMT with these two terms while introducing new coefficients η and ζ:

$$T^{\mu\nu}_{(1)} = -\eta\sigma^{\mu\nu} - \zeta\Delta^{\mu\nu}\nabla^{\perp}_{\lambda}u^{\lambda}\,. \tag{1.56}$$

This equation is the definition of the shear viscosity η and the bulk viscosity ζ. The expression for EMT in the local rest frame again tells us what $P(\epsilon)$ is. The trace of the EMT should be compared to the trace of the expectation value $\langle T^{\mu\nu}\rangle$ of the quantum system slightly off the equilibrium. The trace of the EMT is

$$\left(T^{\mu\nu}_{(0)} + T^{\mu\nu}_{(1)}\right)g_{\mu\nu} = -\epsilon + 3\left(P(\epsilon) - \zeta\nabla^{\perp}_{\lambda}u^{\lambda}\right) \tag{1.57}$$

which should match $\epsilon - 3P$ of slightly out of equilibrium. So by convention, one can choose to consider $P(\epsilon)$ still as the equation of state for the quantum system in equilibrium, and put all

non-equilibrium corrections to the contribution from $T^{\mu\nu}_{(1)}$, which is $-\zeta\nabla^{\perp}_{\lambda}u^{\lambda}$. When the system of our interest is slightly-out-of-equilibrium, the correction from $T^{\mu\nu}_{(1)}$ is small.

The conservation of the EMT of first-order relativistic hydrodynamics,

$$\nabla_{\mu}\left(T^{\mu\nu}_{(0)}+T^{\mu\nu}_{(1)}\right)=0\,, \tag{1.58}$$

gives the relativistic Navier-Stokes equations. Again using projections, along u^{μ}, one obtains

$$D_h\epsilon+(\epsilon+P)\left(\nabla^{\perp}_{\lambda}u^{\lambda}\right)-\eta\sigma^{\mu\nu}\nabla_{\mu}u_{\nu}-\zeta\left(\nabla^{\perp}_{\mu}u^{\mu}\right)^2=0 \tag{1.59}$$

where $u^{\mu}\sigma_{\mu\nu}=0$ was used. For the projection $\Delta^{\mu\alpha}$, we obtain

$$(\epsilon+P)\,D_h u^{\alpha}+c_s^2\nabla^{\alpha}_{\perp}\epsilon-\Delta^{\alpha}_{\nu}\nabla_{\mu}\left(\eta\sigma^{\mu\nu}+\zeta\Delta^{\mu\nu}\left(\nabla^{\perp}_{\lambda}u^{\lambda}\right)\right)=0. \tag{1.60}$$

In the non-relativistic limit $|\vec{v}|\ll 1$ with the assumption that η,ζ are constant, the equations become the continuity equation and non-relativistic Navier-Stokes equation:

$$\partial_t\epsilon+\vec{v}\cdot\partial\epsilon+\epsilon\partial\cdot\vec{v} \;=\; 0 \tag{1.61}$$

$$\epsilon\partial_t\vec{v}+\epsilon\vec{v}\cdot\partial\vec{v}+\partial P \;=\; \eta\partial^2\vec{v}+\left(\zeta+\frac{1}{3}\eta\right)\partial\left(\partial\cdot\vec{v}\right)\,. \tag{1.62}$$

First order hydrodynamics governed by the continuity equation and Navier-Stokes equation is expected to give a good description of strongly coupled systems such as QCD at a finite temperature. The inputs to this effective theory, the equation of state $P(\epsilon)$ and viscosities $\eta(\epsilon),\zeta(\epsilon)$, can in principle be computed from QCD. As these transport coefficients are defined within the framework

of hydrodynamics, it is relativistic hydrodynamics which teaches us about useful correlation functions from which one extracts those coefficients in first-principles calculations. The next section detailes the derivation of such correlation functions.

1.4.3 Hydrodynamic collective modes

Now that we have obtained the equations of motion for the hydrodynamic fields in Sec. 1.4.2, let us solve them and find the expressions for correlation functions of the energy momentum tensor. I start with non-relativistic hydrodynamics as a warm-up [38]. Let us consider an incompressible and homogeneous fluid governed by the Eq. (1.62). The pressure term ∂P vanishes because of homogeneity $\partial\epsilon = 0$, and the last term is also not relevant because $\partial \cdot \vec{v} = 0$ for an incompressible fluid. As an initial condition, I consider a plane wave in x direction:

$$\vec{v}(\vec{r}, 0) = (u_0 \cos(kz), 0, 0)\,. \tag{1.63}$$

The y and z-component of the velocity field will remain zero, and only the x-component needs to be considered:

$$\frac{\partial v_x(z,t)}{\partial t} = \frac{\eta}{\epsilon}\frac{\partial^2 v_x(z,t)}{\partial z^2}. \tag{1.64}$$

The solution for $v_x(\vec{r}, t)$ is

$$v_x(\vec{r}, t) = u_0\, e^{-\frac{\eta k^2}{\epsilon}t}\, \cos(kz) \tag{1.65}$$

Thus, by applying a small perturbation to the velocity field and measuring the exponentially decaying amplitude of the velocity field, the viscosity η with a specific momentum k is extracted. Ultimately we can take the infinite-volume limit $k \to 0$, where the viscosity η is defined.

We would like to find correlators of the same kind in relativistic hydrodynamics as well. In the following, we solve the relativistic Navier-stokes equations via the variational approach [39] instead of adding fluctuation to the conserved quantities such as ϵ and u^μ [40]. The variational approach has an advantage of allowing us to access correlation functions of all components of the EMT. In the canonical approach utilized above, components such as T^{12} cannot be addressed due to the lack of the corresponding conserved quantity. In the variational approach, we add perturbation to the metric tensor $g^{\mu\nu}$, which is the source for the EMT. This means that the retarded two-point correlator of the EMT in flat space can be derived as

$$G^{\mu\nu,\mu\nu} = -2\,\frac{\delta T^{\mu\nu}}{\delta g^{\mu\nu}}\bigg|_{g=g_{\mu\nu}} . \tag{1.66}$$

Thus we consider adding a small fluctuation $\delta^{\mu\nu}$ to the Minkowski metric $g_{\mu\nu}$ and compute the change in $T^{\mu\nu}$ up to the linear order in the perturbation. In practice, it is convenient to add the fluctuation in one special direction and work in momentum space:

$$h^{\mu\nu} = g^{\mu\nu} + \delta^{\mu\nu} e^{-i\omega t + k_z z} . \tag{1.67}$$

The expression for $T^{\mu\nu}$ with the background metric $h^{\mu\nu}$, $T^{\mu\nu}(h^{\mu\nu})$, should be derived up to the first order in $\delta^{\mu\nu}$ to give an expression for $\delta T^{\mu\nu}$ in Eq. (1.66). Note that not only the metric but also the hydrodynamic fields ϵ and u^μ will have corrections due to $\delta^{\mu\nu}$, and they need to be included while deriving the expression for $\delta T^{\mu\nu}$. Now we follow Eq. (1.66) and come to the

following correlation functions in momentum space [39]:

$$G^{00,00}(\omega,k) = -2\epsilon_0 + \frac{k^2\left(\epsilon_0+P_0\right)}{i\gamma_s\omega k^2+\omega^2-c_s^2k^2} \tag{1.68}$$

$$G^{01,01}(\omega,k) = \epsilon_0 + \frac{\eta k^2}{i\omega-\gamma_\eta k^2} \tag{1.69}$$

$$G^{12,12}(\omega,k) = P - i\eta\omega \tag{1.70}$$

where γ coefficients are

$$\gamma_\eta = \frac{\eta}{\epsilon_0+P_0}, \quad \gamma_s = \frac{4\eta}{3\left(\epsilon_0+P_0\right)} + \frac{\zeta}{\epsilon_0+P_0} \tag{1.71}$$

Here ϵ_0 and P_0 are the equilibrium energy density and pressure respectively. The physical meaning of γ coefficients become clearer after Fourier transformation in time. For example, by applying the Fourier transformation $\omega \to t$ to $G^{01,01}$, one obtains

$$G^{01,01}(t,k) \propto e^{-\gamma_\eta k^2 t}\,, \tag{1.72}$$

meaning that γ_η represents the damping length of shear modes. In the same manner γ_s is identified as the damping length of sound modes. The Green-Kubo formula can be derived from Eq. (1.70):

$$\lim_{\omega\to 0}\frac{\partial G^{12,12}(\omega,k=0)}{\partial\omega} = -i\eta. \tag{1.73}$$

These equations give prescriptions for evaluating the viscosity from first-principles, provided that we can compute these correlation functions. Those correlators of $T^{\mu\nu}$ should be computed in position space or momentum space, depending on the underlying theory of our interest and

available methods. In the context of lattice field theories, numerical calculations of such correlators are often done in position space. Therefore Eq. (1.68,1.69) are easier to evaluate — the Green-Kubo relation in the position space becomes the delta function in time and it may not be practical to compute such a singular function numerically on the lattice.

As is mentioned at the beginning of the section, the KSS conjecture provides a conjectured lower bound on the ratio $\eta/s \geq \frac{1}{4\pi}$. The bound is provided by the value of η/s in the $\mathcal{N} = 4$ $SU(N)$ Supersymmetric Yang-Mills theory in the limit of $N \to \infty$ and the coupling constant $g \to \infty$. In this theory, the calculation of correlators Eq. (1.68,1.69,1.70) can be done via the AdS/CFT correspondence [41] — one computes correlators in the bulk which is the classical gravity in Anti de Sitter space, and uses the dictionary [42, 43] to obtain the corresponding correlators for the $\mathcal{N} = 4$ Supersymmetric Yang-Mills on the boundary. The results are [44, 45]

$$G^{01,01}(\omega, k) = \frac{N^2 \pi T^3 k^2}{8\left(i\omega - \frac{k^2}{4\pi T}\right)} \tag{1.74}$$

$$G^{12,12}(\omega, k) = -\frac{N^2 T^2}{16}(2i\pi T\omega + k^2) \tag{1.75}$$

from which we find that $\eta/s = \frac{1}{4\pi}$. Conformal invariance guarantees that the trace of the EMT vanishes, and thus so as the bulk viscosity, i.e. $\zeta = 0$.

We conclude the section by remarking that there are potential corrections to relations in Eq. (1.68,1.69,1.70). Firstly, when we consider higher-order hydrodynamics $T^{\mu\nu}_{(2)} \cdots$, there will be polynomial corrections to the numerator and denominator of Eq. (1.68,1.69,1.70), and so as to the exponent of Eq. (1.72). Secondly thermal fluctuations are believed to introduce polynomial corrections $\sim t^n$ to the correlator in time in Eq. (1.72). When such corrections are present, what we extract from a correlator of the EMT computed from the underlying quantum theory

represent the viscosity with finite volume effects or the effective viscosity in the presence of thermal fluctuations.

Chapter 2: Quantum simulation

2.1 Overview

Collider experiments have given us wealth of opportunities to observe rich phenomena in high energy physics. It is of great theoretical interest to compute observables measured in experiments and confirm whether the fundamental theories successfully explain experimental results. For such tasks, a quantum computer has the promise of playing a unique role [46]. After all, a quantum computer, once built with sufficiently limited noises, can be thought of as a very finely tuned laboratory to study the time-evolution of a quantum system. Thus in principle, given an enormous quantum computer, one can simulate a whole scattering experiment on a quantum computer [47] and compare the outcome — the measurement on the quantum computer — to experimental results. To start an overview of such quantum simulations, it is helpful to decompose a quantum simulation of a collision experiment or any other real-time dynamics of a quantum system into the following five building blocks, as is also roughly sketched in Figure 2.1:

1. Representation of quantum system on qubits

   The Hilbert space of a quantum system to be simulated needs to be mapped onto the Hilbert space of qubits on a quantum computer. To start with the simplest example, the mapping

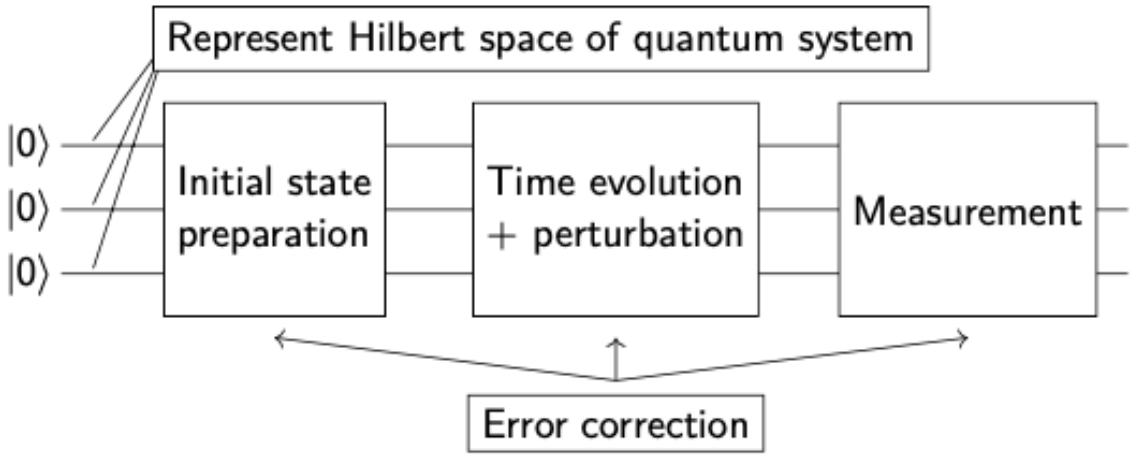

Figure 2.1: A schematic view of the quantum simulation of a quantum system.

of the quantum Ising model is "one to one" — the Hilbert space of a spin is mapped on to that of a qubit. Fermionic fields also have natural mappings to the qubits [48, 49, 50, 51]. For quantum fields with higher-dimensional local Hilbert space, one needs more number of qubits per point in space to represent them. The dimension of the Hilbert space of N qubits is 2^N. Therefore a minimum number of qubits required to fully represent a d-dimensional Hilbert space is $\log_2 d$. Bosonic fields have an infinite-dimensional Hilbert space on each point in space. Such Hilbert space needs to be approximated to be mapped onto a finite number of qubits. Ideas for such truncation includes: crystal-like subgroups [52, 53, 54, 55, 56], momentum space truncation [57, 58, 59], and the prepotential formalism [60, 61, 62, 63, 64, 65].

2. Time evolution via local unitary gates

   As our interest is in simulating the time-evolution of quantum systems, one needs to implement the time-evolution operator e^{-iHt} via primitive quantum gates on the quantum computer, most of which act on only 1 or 2 qubits. The time-evolution operator, when

applied to the qubits representing a quantum system, should (approximately) update the wave function on those qubits following the Hamiltonian of the quantum system. Utilizing the fact that quantum systems of our interest often possess only local interactions, the time-evolution operator can be approximated by a sequence of local unitary operations via the Suzuki-Trotter formula. Trotterized time-evolution circuits have been discussed for Abelian theories in, *e.g.* [66, 67, 68, 69, 70, 71, 72, 73, 74] and non-Abelian gauge theory in [75, 76, 77, 78].

3. Initial state preparation

   Before we apply the time-evolution operator to qubits, one needs to prepare an initial state of our interest. In the context of lattice QCD simulation, the initial state can be, for example, the ground state, a proton at rest, or a thermal state of QCD at a finite temperature. A quantum circuit for preparing such a particular initial state needs to be designed and applied to qubits prior to the time evolution. The state preparation circuit is likely to make use of the time-evolution operator, and thus can be as costly as the time evolution itself. Ideas for the ground state preparation include: variational algorithms [79, 80], Quantum-Phase-Estimate [81, 82], Adiabatic algorithms [83], and spectral combing [84]. Thermal state preparation methods include classical-quantum hybrid algorithms [85, 86] and the quantum refrigerator [15].

4. Measurement

   After the time-evolution, expectation values of operators of our interest should be measured. The construction of this building block involves several different tasks, depending on the goal of one's quantum simulation. Examples for tasks are finding useful operators to

measure and building efficient methods to extract final results from the measurement. In later sections, measurement algorithms for parton distribution functions [14] and hydrodynamic coefficients [15] are detailed.

5. Error correction algorithms

   In this thesis, those four building blocks above are built with the assumption that the quantum computer is noiseless, which is not the case in reality. In actual quantum simulations, error correction algorithms are necessary to obtain physically interesting results with a high precision. Error correction algorithms can be general, or can target specific kinds of error that are expected to be significant in lattice QCD, such as gauge-violating errors [87, 88, 89].

These are the five basic building of quantum simulations of quantum systems. Given one's goal of a quantum simulation, the map above lists a set of quantum algorithms needed to be built. For example, if one's interest is in the quantum simulation of an entire heavy-ion collision, then qubits should represent the Hilbert space of lattice QCD or its effective theories. The time evolution operator should be implemented via the Hamiltonian of lattice QCD or its effective description. As the QCD Hamiltonian only consists of local interactions, the Suzuki-Trotter formula enables us to implement the time-evolution as a sequence of local operations. The initial state should be two well-separated large nuclei heading towards each other with a high momentum, and species of freely streaming hadrons should be measured in the end. This observation makes it clear that we will need an enormous volume of lattice QCD and thus an enormous number of qubits and gates to simulate a heavy-ion collision on a quantum computer.

The state of art is that we do not have such a large-scale quantum computer. Still one can

access important information about heavy-ion collisions without a full simulation of a heavy-ion collision using less quantum resources. To do so, it is useful to describe a heavy-ion collision stage by stage via effective theories. A heavy-ion collision can be thought of as a sequence of stages, each of which has an effective description. Quantum simulations of each stage in a heavy-ion collision with an appropriate effective theory is expected to require less quantum resources — first of all, the quantum simulation does not need to collide a pair of well-separated nuclei, but instead describes the nuclear matter of the size $\sim 10\text{fm}^3$. Important information extracted from such stage-by-stage quantum simulations will be combined to provide us to a better understanding of heavy-ion collisions. Regarding heavy-ion collisions, two relevant effective descriptions are parton distribution functions (PDFs) and relativistic hydrodynamics. PDFs help us describe the initial high-energy collision of two large nuclei. Relativistic hydrodynamics provides a good description of the middle stage of the collision, a dense quark gluon plasma, before the fireball becomes a dilute gas of hadrons. The final stage of a collision, dilute gas of hadrons, is well described by the kinetic theory for which we need no quantum simulations. In the quantum simulation of the PDFs and the hydrodynamic coefficients, the same representation of lattice QCD on qubits and time evolution operator via the QCD Hamiltonian can be utilized. On the other hand, initial state preparation and measurement algorithms differ between the PDFs and the transport cofficients. In the rest of the section, I first summarize the representation of lattice gauge theories on qubits in Sec. 2.2 and time evolution in Sec. 2.3. Then I discuss state preparation algorithms and measurement methods for PDFs in Sec. 2.4 and relativistic hydrodynamics in Sec. 2.5.

2.2 Representation of lattice gauge theory

To start a quantum simulation of a quantum system, qubits on a quantum computer should represent the Hilbert space of the quantum system. When one's interest is the first-principle simulation of the time-evolution of nuclear matter, the quantum system to be simulated is ultimately lattice QCD. In this section, I construct the Hamiltonian formulation of the bosonic part of lattice QCD, which is lattice gauge theory [24, 90]. This section is based on [13], in which general methods for simulating gauge theories together with scalar matter fields and fermionic fields are detailed.

I consider a general lattice gauge theory with gauge group G. The Hilbert space of a link is the complex vector space $\mathcal{H}_G$ spanned by vectors $|g\rangle$ representing each element of the group $g \in G$. The entire Hilbert space of multiple gauge links is constructed by the tensor product of $\mathcal{H}_G$. The Hilbert space of L gauge links is simply $\mathcal{H} = \mathcal{H}_G^{\otimes L}$. Thus when mapping the Hilbert space of a lattice gauge theory, it is natural to map each link $\mathcal{H}_G$ to a set of qubits (G-register) by assigning each element $g \in G$ to the basis states in the G-register.

For discrete groups, it is rather straightforward to implement their G-registers — a finite number of elements in G are each mapped to basis in a set of N_q qubits which possesses 2^{N_q} dimensional Hilbert space. For example, to represent a $\mathbb{Z}_2$ lattice gauge theory, one qubit is enough per each link. For higher-dimensional gauge groups, the dimension of the Hilbert space of G-register needs to be larger than the dimension of the group G. While satisfying this constraint, an efficient way of mapping the local Hilbert space $\mathcal{H}_G$ to qubits can be studied so that the implementation of the time-evolution operator can be done as simply as possible.

How do we map the Hilbert space $\mathcal{H}_G$ of gauge groups with infinite number of elements

such as $SU(N)$ groups? There is no way to perfectly map such a Hilbert space onto qubits since there are only finite number of them. Thus the Hilbert space of each gauge link needs to be truncated to be mapped on to a finite number of qubits. As was mentioned in the last section, there are several methods proposed to truncate the Hilbert space of gauge theories [52, 53, 54, 55, 56, 57, 58, 59, 60, 61, 62, 63, 64, 65].

With a G-register implemented for each gauge link, qubits represent the entire Hilbert space including both physical and unphysical subspaces. As our interest is only in physical states, we shall discuss a gauge-symmetrization operator, which projects any states in the entire Hilbert space onto the physical subspace $\mathcal{H}_P$. On a lattice with N sites, there is an element $V_i \in G$ assigned on each site. The transformation rule for a gauge link U_{ij} from site i to j is $U_{ij} \to V_j U_{ij} V_i^\dagger$. Given a set $V \in G^N$ of elements on N sites, let us denote the gauge transformation as $\phi(V)|U_{ij}\cdots\rangle = |V_j U_{ij} V_i^\dagger \cdots\rangle$. All states connected by $\phi(V)$ for all $V \in G^N$ are physically equivalent, and they together form the gauge orbit. The physical space is then $\mathcal{H}_P = \mathcal{H}_G^{\otimes L}/\phi(G^{\otimes N})$. The projection of a state to the physical subspace is done by a gauge symmetrization operator:

$$P|U_{12}\cdots\rangle = \frac{1}{|G|^N}\int_G dV_1 \cdots \int_G dV_N \;\; |V_2 U_{12} V_1^\dagger \cdots\rangle = \frac{1}{|G|^N}\int_{G^N} dV \;\; \phi(V)|U_{12}\cdots\rangle \quad (2.1)$$

An implementation of the operator P for $U(1)$ gauge theory is given in [91].

Since the entire Hilbert space is much larger than the physical subspace, it might seem to be a waste of qubits to map the entire Hilbert space onto qubits. However, the efficiency of representation methods of lattice gauge theories should not be discussed based only on the qubit cost at first glance. The efficiency of representation methods should be investigated while

considering other costs present in the entire quantum simulation. For example, the number of qubits one needs to achieve a certain small lattice spacing and the complexity of the time evolution circuit both depend on methods for representing lattice gauge theories. The search for an efficient formalism for the quantum simulation of gauge theories is a very active area of research. Regarding the gauge invariance of quantum simulations in the presence of the unphysical subspace, states of our interest to measure observables for as well as observables themselves are gauge-invariant. As the Hamiltonian for lattice gauge theories (which will be constructed in Eq. (2.19) in the next section) and thus time-evolution operator are strictly gauge-invariant, as long as one starts with an gauge-invariant initial state, the final state on a quantum computer is guaranteed to be gauge invariant. Therefore one obtains physically meaningful results by measuring gauge-invariant observables on the final state, even though the state in the middle of unitary gate operations is not expected to be gauge invariant. With the presence of noises in the middle of the quantum simulation, the final state is likely to contain gauge-violating states. Such errors can be reduced by applying quantum error correction algorithms for taming gauge-violating errors [87, 88, 89].

2.3 Time evolution

2.3.1 Hamiltonian of lattice gauge theories

Quantum simulations consists of the Hilbert space (qubits) and operators to act on it (unitary gates). Now that the Hilbert space of a lattice gauge theory is mapped onto that of qubits, we should construct the most important operation to these qubits — the time evolution operator — via quantum gates. For that, we first need the expression for the Hamiltonian of lattice

gauge theory. In the following, we focus on lattice $SU(3)$ gauge theory, and generalize the expression for its Hamiltonian to a general lattice gauge theory in the end. One way to obtain lattice $SU(3)$ Hamiltonian is to derive one from the action of lattice gauge theory, e.g. Wilson action in Eq. (1.19):

$$\begin{aligned} S_W &= \sum_{t=1}^{N_t} K(t) + V(t) && (2.2)\\ K(t) &= \sum_n \sum_i \frac{a}{g_s^2 a_0} \operatorname{Re}\operatorname{Tr}\left[1 - P_{0i}(n,t)\right] && (2.3)\\ V(t) &= \sum_n \sum_{i<j} \frac{a_0}{g_s^2 a} \operatorname{Re}\operatorname{Tr}\left[P_{ij}(n,t)\right] && (2.4) \end{aligned}$$

through the transfer matrix $\hat{T} = e^{-i\hat{H}}$ [90] which is defined to act on the entire Hilbert space [13]. The Hamiltonian formulation and action formulation of a quantum theory are connected by the Trotterization:

$$\langle U_t | e^{-i\hat{H}t} | U_0 \rangle = \int \mathcal{D}U \langle U_t | \hat{P}\hat{T} | U_{t-1} \rangle \cdots \langle U_1 | \hat{P}\hat{T} | U_0 \rangle = \int \mathcal{D}U \; e^{iS}. \tag{2.5}$$

Here $\mathcal{D}U$ means the all "paths" for spacial gauge links are taken while respecting the boundary condition U_0 and U_t for the initial and final states respectively. For this equality to hold with the lattice action for $SU(3)$ gauge theory, the following must be true:

$$\langle U' | \hat{T} | U \rangle = e^{i(K(t)+V(t))} = e^{i\sum_n \left(\frac{a}{g_s^2 a_0} \sum_i \operatorname{Re}\operatorname{Tr}\left[1 - U_{n,i} U'^{\dagger}_{n,i}\right] + \frac{a_0}{g_s^2 a} \sum_{i,j} \operatorname{Re}\operatorname{Tr}\left[U_{n,i} U_{n+\hat{i},j} U^{\dagger}_{n+\hat{j},i} U^{\dagger}_{n,j}\right] \right)}. \tag{2.6}$$

When one inserts this relation to Eq. (2.5) without the projection operator P at each time slice in Eq. (2.1), one recovers the path integral with the Wilson action Eq. (2.2) where the temporal

gauge links are set to the identity. To reproduce the Wilson gauge action with arbitrary temporal gauge links, we insert the projection P at each time slice. To demontstrate, for the kinetic term on a link U_{ab} from site a to site b, the transfer matrix's matrix elements are

$$\langle U'_{ab}|T|U_{ab}\rangle = e^{i\frac{a}{g_s^2 a_0}\,\mathrm{Re\,Tr}\left[1-U_{ab}U'^{\dagger}_{ab}\right]}\,, \tag{2.7}$$

which will yield a kinetic term with the identity on temporal gauge links in the action formulation. By inserting the projection operator, the matrix elements become

$$\langle U'_{ab}|TP|U_{ab}\rangle = \int_G dg_a \int_G dg_b\; e^{i\frac{a}{g_s^2 a_0}\,\mathrm{Re\,Tr}\left[1-g_a^{\dagger}U_{ab}g_b U'^{\dagger}_{ab}\right]}\,, \tag{2.8}$$

which now encodes the integral over the temporal gauge links as is usually seen in the path integral in Eq. (1.24). Thus by inserting projection operators at each time slice, the resulting path integal formalism obtains temporal gauge degrees of freedom.

The equation above, Eq. (2.6), in principle defines the Hamiltonian for the lattice $SU(3)$ gauge theory. To transfer the Hamiltonian to a useful form as an operator, I would like to find an expression for $\hat{H}$ which acts on the Hilbert space (so either $\langle U'|$ or $|U\rangle$) and realizes the equality Eq. (2.6). For this purpose, let us introduce two kinds of basic operators. One is the gauge link operator $U_{n,i}$ which is diagonal in the "position" basis:

$$\hat{U}_{n,i}|U_{n,i}\rangle = U_{n,i}|U_{n,i}\rangle \tag{2.9}$$

Note that gauge link operators are defined only for gauge links in spatial direction ($i = x, y, z$), as gauge links in the temporal direction $U_{n,t}$ do not exist in the Hamiltonian formulation. The

gauge link operators transform as

$$\hat{U}_{n,i} \to g^{-1}_{n+\hat{i}}\, \hat{U}_{n,i}\, g_n \tag{2.10}$$

The second kind of operator is the conjugate operator of $U_{n,i}$ which we denote as $\pi_{n,i}$. They are not diagonal in the position basis:

$$\hat{R}_{n,i}(g)|U_{m,j}\rangle = \begin{cases} |g\, U_{m,j}\rangle & \text{when } m = n \text{ and } i = j \\ |U_{m,j}\rangle & \text{otherwise} \end{cases} \tag{2.11}$$

with

$$\hat{R}_{n,i}(g) = e^{ix^a \hat{\pi}^a_{n,i}}\ . \tag{2.12}$$

Here, x^a are eight real numbers parameterizing the group element $g \in SU(3)$, and π^a are eight Hermitian operators associated with x^a. Using these primitive operators, one finds an expression for the transfer matrix operator $\hat{T}$ which satisfies the relation Eq. (2.6):

$$\hat{T} = \int_{g\in G} \prod_{n,i} \Big[dg_{n,i}\ \hat{R}_{n,i}(g_{n,i}) \Big]\ e^{i\frac{a}{g_s^2 a_0} \sum_{n,i} \mathrm{Re}\,\mathrm{Tr}\left[1 - g^\dagger_{n,i}\right] + i\hat{V}}. \tag{2.13}$$

Here, $\hat{V}$ is simply the operator version of the potential term in Eq. (2.4) obtained by converting all links in $V(t)$, which are spatial, to the corresponding link operators $\hat{U}$. Note that temporal gauge links $A_{n,0}$ are set to zero, and this is the convention I take in the rest of the thesis. Now that the transfer matrix is written with operators, in principle, one can obtain the Hamiltonian by taking $\hat{H} = -\log(\hat{T})$. However, to obtain an even more useful expression for the Hamiltonian,

one can further simplify the expression for $\hat{T}$ by taking the Hamiltonian limit $a_0 \to 0$ before we take the logarithm. For that purpose, let us rewrite g with real parameters x^a

$$\hat{T} = \int_{-\pi}^{\pi} \prod_{n,i,a} \left[dx^a_{n,i} \; e^{i x^a_{n,i} \hat{\pi}^a_{n,i}} \right] \; e^{i \frac{a}{g_s^2 a_0} \sum_{n,i} \mathrm{Re\,Tr} \left[1 - e^{i x^a_{n,i} \lambda^a} \right] + i\hat{V}}. \tag{2.14}$$

In the $a_0 \to 0$ limit, the integral can be evaluated by the saddle point approximation. The saddle point is $x = 0$ and its gauge-equivalent points that form the gauge orbit. Since the whole expression of $\hat{T}$ is gauge invariant, we simply take the saddle point to be $x = 0$ and obtain

$$\hat{T} \sim \int dx \; e^{i x_\rho \hat{\pi}_\rho + \frac{ia}{2 g_s^2 a_0} x_\rho x_\rho + i\hat{V}} = N e^{-i a_0 \frac{g_s^2}{2a} \hat{\pi}_\rho \hat{\pi}_\rho + i\hat{V}}. \tag{2.15}$$

Here a compact notation for indices is introduced as $\rho \equiv (n, i, a)$. Now it is straightforward to take the logarithm of $\hat{T}$ to obtain the Hamiltonian. The resulting Kogut-Susskind Hamiltonian [24] is

$$\hat{H}_{KS} = \frac{g_s^2}{2a} \sum_{n,i,a} \hat{\pi}^a_{n,i} \hat{\pi}^a_{n,i} - \frac{1}{g_s^2 a} \sum_{\substack{n \\ i<j}} \mathrm{Re\,Tr} \left[\hat{P}_{ij}(n) \right]. \tag{2.16}$$

By introducing the operator

$$\hat{\pi}_{n,i} = \hat{\pi}^a_{n,i} T^a \tag{2.17}$$

which transform as

$$\hat{\pi}_{n,i} \to g_n^{-1} \; \hat{\pi}_{n,i} \; g_n, \tag{2.18}$$

under the gauge transformation, the Hamiltonian can be written as

$$\hat{H}_{KS} = \frac{g_s^2}{2a} \sum_{n,i,a} \mathrm{Tr}[\hat{\pi}_{n,i}^2] - \frac{1}{g_s^2 a} \sum_{\substack{n \\ i<j}} \mathrm{Re}\,\mathrm{Tr}\left[\hat{P}_{ij}(n)\right]. \tag{2.19}$$

This is the Hamiltonian of lattice $SU(3)$ gauge theory. Note that each term is gauge-invariant under the transformation by Eq. (2.10) and Eq. (2.18), which will guarantee the gauge-invariance of the time-evolution operator after Trotterization, as will be discussed in the next section. Hamiltonians of general lattice gauge theories with gauge group G take the same form Eq. (2.19). The gauge link operators are as defined in Eq. (2.9) so that they are diagonal in the position basis of the group G. Operator $\pi_{n,i}$ is the momentum operator conjugate to $U_{n,i}$ and $\pi_{n,i}^2$ is the Laplace-Beltrami operator on the surface G.

2.3.2 Suzuki-Trotterization

In this section, I decompose the time evolution operator into local time evolution operators via Trotterization and implement them using four primitive circuits [13]:

1. **Inversion gate**. This gate acts on a single G-register and changes the register to its inverse:

$$\mathfrak{U}_{-1} |g\rangle = \left|g^{-1}\right\rangle. \tag{2.20}$$

2. **Multiplication gate**. This gate acts on two G-registers and multiplies the second register by the first register:

$$\mathfrak{U}_{\times} |g\rangle |h\rangle = |g\rangle |gh\rangle. \tag{2.21}$$

3. **Trace gate**. This gate acts on a single G-register and obtains the trace of the register

$$\mathfrak{U}_{\mathrm{Tr}}(\theta)\,|g\rangle = e^{i\theta\,\mathrm{Re}\,\mathrm{Tr}\,g}\,|g\rangle\,. \tag{2.22}$$

4. **Fourier transformation gate**. This gate acts on a single G-register and transforms it into the Fourier space:

$$\mathfrak{U}_F \sum_{g\in G} f(g)\,|g\rangle = \sum_{\rho\in\hat{G}} \hat{f}(\rho)_{ij}\,|\rho,i,j\rangle \tag{2.23}$$

These primitive gates allow us to construct the time evolution of the lattice gauge theory with its Hamiltonian in Eq. (2.19).

The time-evolution operator $\mathcal{U}(t) = e^{-i\hat{H}t}$ is an operator that acts on the entire Hilbert space, which cannot be implemented efficiently via primitive gates on a quantum computer — usually they perform only 1, 2 or 3-qubit operations. To construct an approximate operator for the time-evolution via primitive gates available on a quantum computer, we employ the Trotter-Suzuki formula:

$$\mathcal{U}_{TS}(t) = \prod_{t/\Delta t} e^{-iH_K\Delta t}e^{-iH_V\Delta t}. \tag{2.24}$$

Note that the Trotterization does not break gauge invariance at any orders in Δt since each term in the Hamiltonian is gauge invariant. The Trotterization approximates the exact time evolution operator up to $O(\Delta t^2)$ or $O(\Delta t^3)$, depending on the order of kinetic and potential terms in the Trotterization. As the kinetic term H_K and the potential term H_V each consists of mutually commuting operators, time-evolution via those terms can be written as a product of local time-

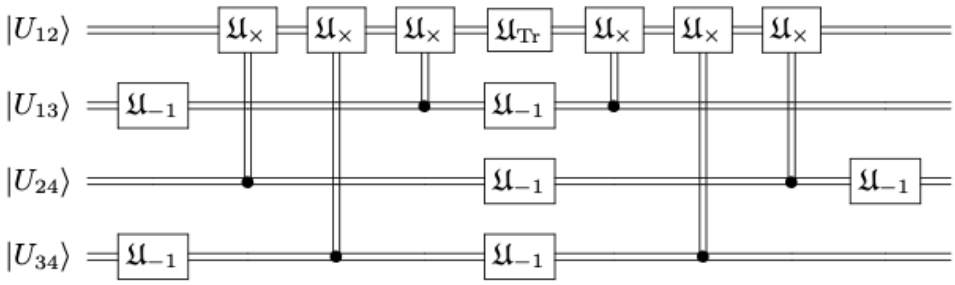

Figure 2.2: A quantum circuit for the potential part of the time evolution operator $\mathcal{U}_V^{(1)}(i,j)$.

evolution:

$$e^{-iH_K\Delta t} = \prod_{\langle ij\rangle} \mathcal{U}_K^{(1)}(i,j), \qquad \mathcal{U}_K^{(1)}(i,j) = e^{-i\frac{g^2}{2a}\pi_{ij}^2\Delta t} \tag{2.25}$$

and

$$e^{-iH_V\Delta t} = \prod_{p} \mathcal{U}_V^{(1)}(p), \qquad \mathcal{U}_V^{(1)}(p) = e^{i\frac{1}{g^2 a}\,\mathrm{Re\,Tr}[P_{\mu\nu}(n)]\Delta t}. \tag{2.26}$$

Operators $\mathcal{U}_K^{(1)}(i,j)$ can be applied in any order within $e^{-iH_K\Delta t}$ as they commute with each other; likewise for operators $\mathcal{U}_K^{(1)}(i,j)$ in $e^{-iH_V\Delta t}$.

The potential part of the time evolution $\mathcal{U}_V^{(1)}$ is constructed with the multiplication gate and trace gate and the help of an ancillary register: we prepare the product of four links of the plaquette and then apply the trace gate $\mathfrak{U}_{\mathrm{Tr}}(\frac{1}{g^2 a})$. The circuit is shown in Figure 2.3.2. Note that the circuit in Figure 2.3.2 prepares the product of four links on one of those link instead on an ancillary register.

The kinetic part $\mathcal{U}_K^{(1)}$ is constructed via the Fourier transformation gate for to diagonalize the operator and then a diagonal unitary:

$$\mathcal{U}_K^{(1)}(i,j) = \mathfrak{U}_F \mathfrak{U}_{\mathrm{phase}} \mathfrak{U}_F^{\dagger}. \tag{2.27}$$

The construction of the phase gate depends on the group G, its truncation if necessary, and how one implements of the G-register. Once the G-register is designed, the phase gate should be constructed so that it gives an appropriate phase to all eigenstates in the momentum basis.

The number of circuits needed to perform the time evolution of a lattice gauge theory with N_L links and N_P plaquettes are:

$$\mathfrak{U}_{-1} \ : \ 6N_P\frac{T}{\Delta t}, \quad \mathfrak{U}_{\times} : 6N_P\frac{T}{\Delta t}, \quad \mathfrak{U}_{\rm Tr} : N_P\frac{T}{\Delta t} \tag{2.28}$$

$$\mathfrak{U}_{F} \ : \ 2N_L\frac{T}{\Delta t}, \quad \mathfrak{U}_{\rm phase} : N_L\frac{T}{\Delta t} \ . \tag{2.29}$$

The remaining task is to implement these primitive circuits with the quantum gates available on a quantum computer. In the next section, we construct these primitive circuits for the dihedral D_4 gauge theory and demonstrate the time evolution of the system. For simulating lattice $SU(3)$ gauge theory, it is necessary to truncate the group. One truncation method is to approximate the $SU(3)$ group with its largest crystal-like subgroup called $\mathcal{S}(1080)$, which has 1080 elements [52, 53, 54, 55, 56]. The design of the $\mathcal{S}(1080)$ register and the construction of primitive circuits are currently studied.

In the rest of the section, we describe methods for computing certain correlators given the time-evolution circuit for a gauge theory: correlators of spatial plaquettes and a temporary extended Wilson loop [13]. Algorithms described here will be applied to the measurements of PDFs and transport coefficients in later sections. In both cases, measurements of a unitary operator will be necessary. The expectation value of a unitary operator is computed by introducing an ancillary qubit in the following way [92]. Firstly, given the state $|P\rangle$ for which we would like to measure a unitary operator $\mathcal{U}$, we introduce an ancillary qubit and prepare the state

$|P_1\rangle = \frac{1}{\sqrt{2}}\left(|0\rangle_a|P\rangle + |1\rangle_a|P\rangle\right)$. Here the index a denotes the state on the ancillary qubit. Then we apply the unitary operator $\mathcal{U}$ controlled on the ancillary qubit

$$\mathcal{U}_c = |0\rangle_{aa}\langle 0|\ I + |1\rangle_{aa}\langle 1|\ \mathcal{U}. \tag{2.30}$$

Here I denotes the identity operator that acts on the original Hilbert space. The resulting state is $|P_2\rangle = \mathcal{U}_c|P_1\rangle = \frac{1}{\sqrt{2}}\left(|0\rangle_a|P\rangle + \mathcal{U}|1\rangle_a|P\rangle\right)$. The measurements of σ_x and σ_y on the ancillary qubit give the real part and imaginary part of $\langle P|\mathcal{U}|P\rangle$ respectively:

$$\langle P|\mathcal{U}|P\rangle = \langle P_2|\sigma_x \otimes I|P_2\rangle + i\langle P_2|\sigma_y \otimes I|P_2\rangle \tag{2.31}$$

With this algorithms in mind, let us transform correlators of our interest into a set of unitary operators and apply the method above to measure such correlators.

The correlator of spatial Wilson plaquettes's real part $W_{\mu\nu} = \mathrm{Re}\,\mathrm{Tr}\,[P_{\mu\nu}]$ can be thought of as the glueball propagator in QCD. The correlator of our interest here is of the form:

$$\langle\Psi|\ \mathcal{U}(-t)\ W_{\mu'\nu'}(x')\,\mathcal{U}(t)\ W_{\mu\nu}(x)\ \ |\Psi\rangle\,. \tag{2.32}$$

Utilizing the fact that the operators $W_{\mu\nu}$ are Hermitian, one prepares a family of time-dependent Hamiltonian parameterized by two small real numbers ϵ_1 and ϵ_2:

$$H_{\epsilon_1,\epsilon_2}(\tau) = H_0 + \epsilon_2\delta(\tau - t)W_{\mu'\nu'}(x') + \epsilon_1\delta(\tau)W_{\mu\nu}(x) \tag{2.33}$$

The measurement of the family of unitary operators $C(\epsilon_1, \epsilon_2) \equiv \langle\Psi|\mathcal{U}(-t)\mathcal{U}_{\epsilon_1,\epsilon_2}(t)\,|\Psi\rangle$, with

the time-evolution $U_{\epsilon_1,\epsilon_2}$ via the Hamiltonian $H_{\epsilon_1,\epsilon_2}$, can be performed via the method described above. To obtain the plaquette correlator, one differentiates $C(\epsilon_1, \epsilon_2)$ with respect to the perturbation:

$$- \left. \frac{\partial^2 C(\epsilon_1, \epsilon_2)}{\partial \epsilon_1 \partial \epsilon_2} \right|_{\epsilon_1=\epsilon_2=0} = \langle\, U(-t)\, W_{\mu'\nu'}(x')\, \mathcal{U}(t)\, W_{\mu\nu}(x)\, \rangle \tag{2.34}$$

In practice, the derivative can be taken numerically after measuring the correlator $C(\epsilon_1, \epsilon_2)$ for several small ϵ_1 and ϵ_2. This method can be straightforwardly extended to the n-point correlators of plaquettes with the requirement that the numerical differentiation will be taken n times.

The measurement of temporally-extended Wilson loops $\left\langle \mathrm{Re\,Tr}\, U_{ij}^\dagger(t) U_{ij}(0) \right\rangle$ can be done in the same way by the decomposition of the operator into unitary pieces. Note that the temporal gauge $A_{n,0}$ is set to be zero as usual. As a gauge link U_{ij} takes complex matrix values in general, one decomposes the correlator into matrix elements as $\left\langle \mathrm{Re}([U_{ij}^\dagger(t)]^{ba}[U_{ij}(0)]^{ab}) \right\rangle$ and define a family of perturbed Hamiltonian:

$$H_\epsilon^{ab}(\tau) = H_0 + \epsilon_2 \delta(\tau - t)\, \mathrm{Re}[U_{ij}^\dagger]^{ba} + \epsilon_1 \delta(\tau)\, \mathrm{Re}[U_{ij}]^{ab} + \tilde{\epsilon}_2 \delta(\tau - t)\, \mathrm{Im}[U_{ij}^\dagger]^{ba} + \tilde{\epsilon}_1 \delta(\tau)\, \mathrm{Im}[U_{ij}]^{ab}. \tag{2.35}$$

With the perturbed Hamiltonian, correlators $C^{ab}(\epsilon_1, \tilde{\epsilon}_1, \epsilon_2, \tilde{\epsilon}_2) \equiv \langle \Psi |\, \mathcal{U}(-t) \mathcal{U}_\epsilon^{ab}(t)\, | \Psi \rangle$ should be measured by utilizing the method above for the measurement of unitary operators. By take a numerical differentiation, one obtain

$$- \left[\frac{\partial^2}{\partial \epsilon_1 \partial \epsilon_2} - \frac{\partial^2}{\partial \tilde{\epsilon}_1 \partial \tilde{\epsilon}_2} \right]_{\epsilon=0} C^{ab}(\epsilon_1, \epsilon_2, \tilde{\epsilon}_1, \tilde{\epsilon}_2) = \mathrm{Re} \left\langle \mathcal{U}(-t) [U_{ij}^\dagger]^{ba} \mathcal{U}(t) [U_{ij}]^{ab} \right\rangle. \tag{2.36}$$

The imaginary part of the correlator can be measured in a similar way. Now we sum over the

indices a, b to obtain the trace of the correlator.

For many gauge groups, different matrix elements $\left\langle \mathrm{Re}([U_{ij}^{\dagger}(t)]^{ba}[U_{ij}(0)]^{ab}) \right\rangle$ are related by gauge symmetry as it is the case for dihedral D_4 (simulated below) and $SU(N)$ in the fundamental representation. In such cases, the correlator needs to be evaluated for a particular choice of a, b. Also note that perturbation by the link U_{ij} is not gauge-invariant unlike the spatial Wilson plaquette $W_{\mu\nu}$. As a consequence, the state during the time-evolution is not gauge invariant but rather lie in the entire Hilbert space. Nevertheless, by summing over a, b and taking the trace at the end, one obtains the desired invariant Wilson loop.

2.3.3 Demonstration

In this section I demonstrate the time-evolution of dihedral D_4 gauge theory [13] on a two-plaquette lattice shown in Figure 2.3.3. The lattice is smallest non-trivial setting in the sense that the lattice cannot be reduced to 1 spatial dimension. There are four link degrees of freedom, and thus One needs four D_4 registers. Each link has the Hilbert space of dimension 8, which can be represented by 3 qubits. In addition to that, two ancillary qubits are introduced for the time-evolution and measurements and one ends up with a 14-qubit simulation. The action for the

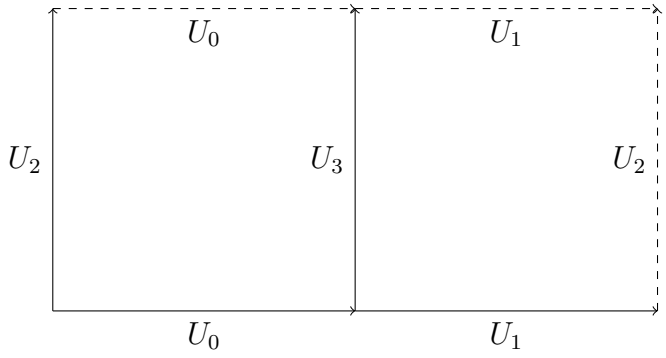

Figure 2.3: $D4$ gauge theory on a 2-plaquette lattice

model is

$$\begin{aligned} S = & - \frac{1}{g^2} \sum_t \left(\mathrm{Re\,Tr} \left[U_2^\dagger(t) U_0^\dagger(t) U_3(t) U_0(t) \right] + \mathrm{Re\,Tr} \left[U_3^\dagger(t) U_1^\dagger(t) U_2(t) U_1(t) \right] \right) \\ & - \frac{1}{g^2} \sum_{P_T} \mathrm{Re\,Tr}\, P_T. \end{aligned} \tag{2.37}$$

The last term is a sum over all temporal plaquettes on the lattice. The corresponding Hamiltonian is

$$\begin{aligned} H = & \mathrm{Re\,Tr} \left[U_2^\dagger(t) U_0^\dagger(t) U_3(t) U_0(t) \right] + \mathrm{Re\,Tr} \left[U_3^\dagger(t) U_1^\dagger(t) U_2(t) U_1(t) \right] \\ & - \sum_{i=0,1,2,3} \log T_K^{(1)}(i) \end{aligned} \tag{2.38}$$

where $\log T_K^{(1)}(i)$ the kinetic term on link i. Having the toy-model set up, the next step is to design the D_4 register and implement the primitive circuits: $\mathfrak{U}_\times$, $\mathfrak{U}_-$, $\mathfrak{U}_{\mathrm{Tr}}$, $\mathfrak{U}_F$, and $\mathfrak{U}_{\mathrm{phase}}$. The details of the design of these circuits are discussed in the Appendix A.

As is discussed in Sec. 2.2, the initial state must be gauge-invariant. In the demonstration, the initial state was chosen to be the gauge projection of the identity matrix on each link. The system is time-evolved for $t = 10$ with two different Trotter time steps, $\Delta t = 0.2$ and $\Delta t = 0.5$. Figure 2.3.3 shows the expectation value of one of the plaquettes over time. The exact result is shown in black, while those with Trotter step sizes of $\Delta t = 0.2$ and $\Delta = 0.5$ are shown in red and blue respectively. The source of errors in the simulation are the Trotterization and the sampling when computing expectation values. For the larger trotter step of $\Delta = 0.5$, the Trotter error builds up and becomes noticeable at larger time.

With the same model, I demonstrate the measurement of temporal Wilson loop as shown in

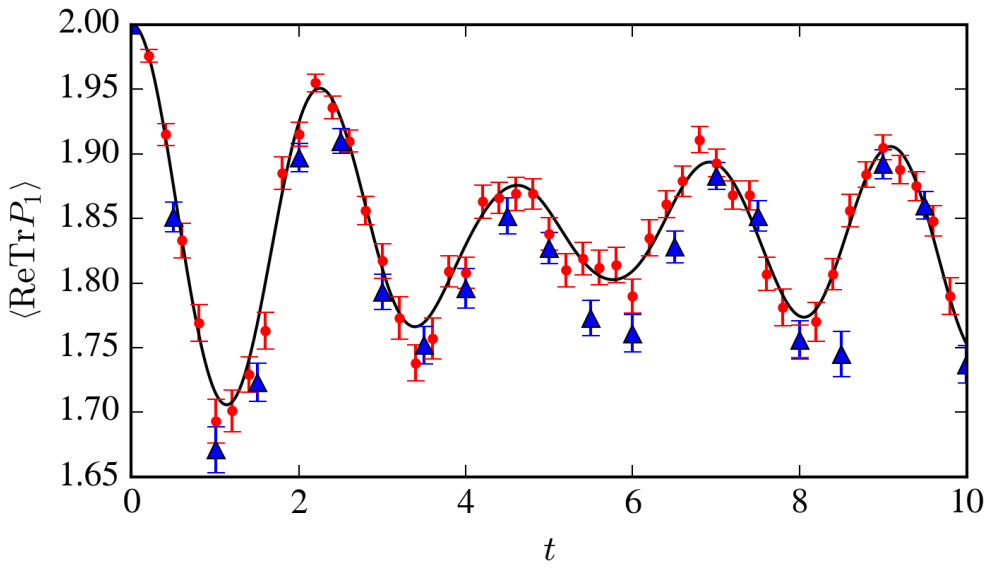

Figure 2.4: The expectation value of one of the plaquettes over time. The black solid line represents the exact result. Classical simulation of quantum calculation are done with Trotter steps of $\Delta = 0.2$ in red and $\Delta = 0.5$ in blue. The difference between the exact result and quantum calculation comes from the sampling in quantum calculation (estimated and shown in error bars) and the Trotterization.

Figure 2.3.3. In the simulation, the time-evolution is performed with the Trotter step $\Delta t = 0.2$. Choices of the ϵs are $(\epsilon_1, \epsilon_2) = (0.1, 0.0), (0.0, 0.1), (0.1, 0.1)$ and the same for the parameters $\tilde{\epsilon}_1, \tilde{\epsilon}_2$, and the numerical differentiation was taken.

2.4 Parton distribution functions

2.4.1 Overview

In this section, I discuss the state preparation and measurement algorithms for computing parton distribution functions (PDFs) and the hadronic tensor [14]. They are non-perturbative objects that capture the structure of hadrons in terms of fundamental degrees of freedom: quarks and gluons. They provide non-perturbative inputs to high-energy scattering experiments such as

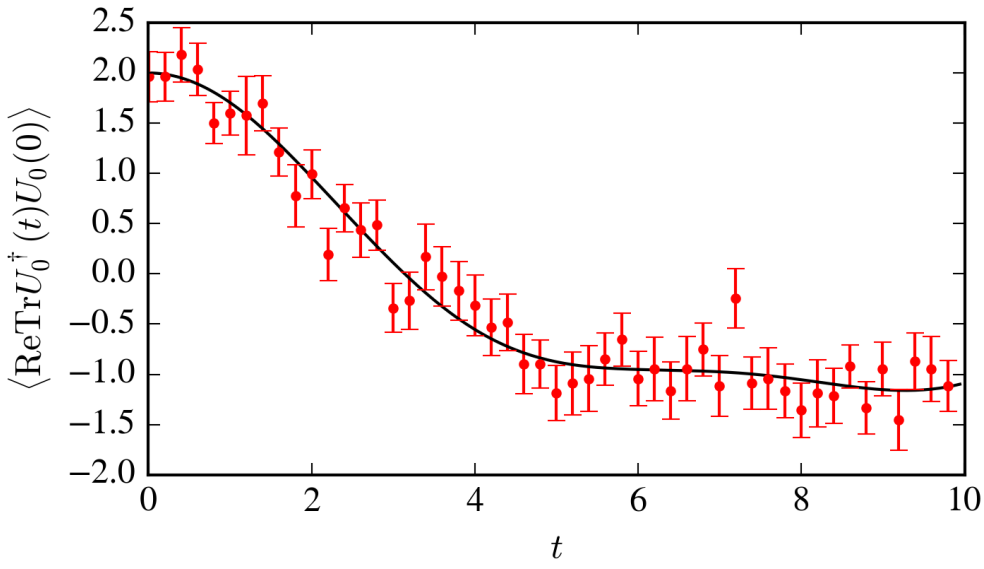

Figure 2.5: The expectation value of a temporal Wilson loop as a function of the time extent of the loop. Total of 2×10^5 measurements were collected for each data point. In addition to errors from the sampling, Trotterization and finite differencing introduce systematic errors.

a deep inelastic scattering's cross section and the initial conditions of heavy-ion collisions. Thus it is of both experimental and theoretical interest to determine PDFs and the hadronic teosor [93]. As PDFs and the hadronic tensors describe such properties of hadrons, non-perturbative calculation via lattice QCD is necessary to theoretically evaluate them. Both PDFs and hadronic tensors are defined in the context of high-energy scattering and thus involve correlators with a real-time evolution. Although Minkowski lattice calculation of such correlators naively suffer from the real-time sigh problem, there have been methods studied to circumvent the issue for PDFs such as analytical continuation [94, 95], Compton amplitudes [96], quasi-PDFs [97] and similarly pseudo-PDFs [98]. Computation of the hadronic tensor has also been studied [99]. The purpose of this section is to propose yet another method to compute PDFs and the hadronic tensor via quantum simulation. First-principles calculations of PDFs and the hadronic tensor on a quantum computer can be done without sign problems, and are expected to be generalized to Generalized

Parton Distributions straightforwardly. We start with PDFs and discuss state preparation algorithms in Sec. 2.4.2. I discuss a measurement procedure in Sec. 2.4.3 and give a concrete example of a quantum computation of PDFs of the Thirring model in $1+1$-dimension. When the algorithm is generalized to QCD, we encounter a technical difficulty arising from the Wilson line on the light-cone. To circumvent the problem, an alternative object, the hadronic tensor, is considered in Sec. 2.4.4.

To start, let us introduce the theoretical definition of PDFs and find the goal of each building blocks in the map of the quantum simulation Figure 2.1. Parton distribution functions are interpreted as the probability distribution function for finding a parton species p_i (either quarks or gluons) with momentum fraction x of the total momentum of proton P. Using such probability distribution functions $f_i(x)$, the total cross section of a high-energy electron scattering off a proton P in Figure 2.4.1 is expresse as

$$\sigma_{e^-P\to e^-X} = \sum_i \int_0^1 dx\ f_i(x)\sigma\left(e^- p_i \to e^- X\right) \tag{2.39}$$

where $\sigma\left(e^- p_i \to e^- X\right)$ are scatting cross section of the electron and quarks or gluons. Here X reprensents the final state of the scattering except the electron. Aymptotic freedom implies that partons look free when the momentum transfer q is high in Figure 2.4.1 except for QED interaction. Thus the electron can only scatter from charged particles in the proton, which are quarks. The cross section of an electron and a quark can be computed easily. Thus, once PDFs $f_i(x)$ for quarks are obtained from lattice calculations, the total cross section can be computed by Eq. (2.39).

In this section we particularly focus on PDFs on quarks $f_i(x)$ of flavor i which can be

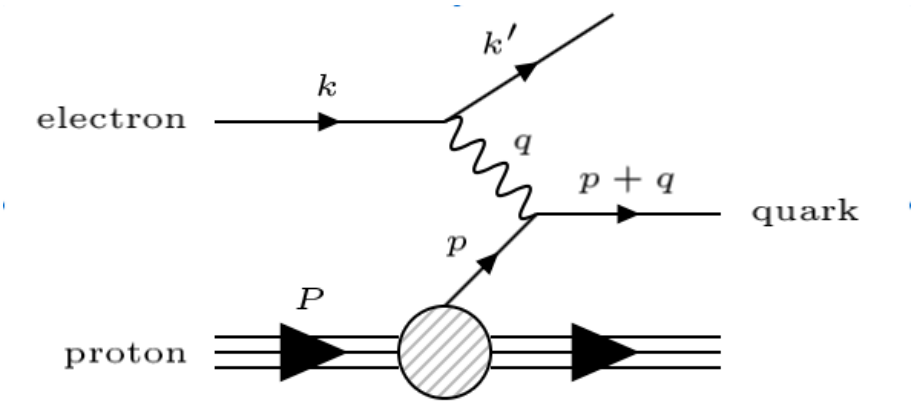

Figure 2.6: Deep inelastic scattering of an electron off a proton

computed from QCD as

$$f_i(x) = \int_{-\infty}^{\infty} \frac{dt}{2\pi} e^{-itx(n\cdot P)} \langle P|\bar{\psi}_i(tn^\mu)\gamma^+ W(tn^\mu;0)\psi_i(0)|P\rangle \tag{2.40}$$

where $\gamma^+ \equiv (\gamma^0+\gamma^1)/\sqrt{2}$. The state $|P\rangle$ is the proton state to evaluate PDFs for. The observable to measure consists of the quark operators $\psi_i(tn^\mu)$ ($n^\mu = (1,\vec{n})$ is a light-like vector), and $\bar{\psi}_i(0)$ on the light-cone. Those two quark operators need to be connected by a Wilson line on the light cone to make the entire observable gauge-invariant.

The evaluation of quark distribution functions on a quantum computer thus involves computing the expectation values of the following real-time correlator:

$$C(t) = \langle P|\bar{\psi}_q(tn^\mu)\gamma^+ W(tn^\mu;0)\psi_q(0)|P\rangle \ . \tag{2.41}$$

Therefore, we shall prepare a proton at rest as a initial state in the next section Sec. 2.4.2. Then I discuss how to evaluate the correlator $C(t)$ in Eq. (2.41) once a proton state is prepared on the quantum computer in Sec. 2.4.3. This quantum algorithm will be demonstrated with the $1+1$-

dimensional massive Thirring model.

2.4.2 State preparation

In this section, we discuss an quantum algorithm for preparing the state which we measure PDFs for — a proton at rest on a 3-dimensional spatial lattice. The central method we employ here is the adiabatic state preparation, which works as following.

1. We define a family of Hamiltonians $H(g)$ which are smoothly connected by the change of a parameter g of the Hamiltonian. In this family, the Hamiltonian of ones interest, $H_f(g_f)$, and a Hamiltonian whose ground state is known and thus can be prepared, $H_i(g_i)$, need to be included.

2. We prepare the ground state of H_i.

3. We perform the time-evolution of the system while slowly changing the parameter g from g_i to g_f until the Hamiltonian becomes H_f.

4. The adiabatic theorem guarantees that the system remains to be in the ground state as long as the Hamiltonian is changed slowly

$$\dot{H}/\Delta^2 \ll 1 \tag{2.42}$$

where Δ is gap between the ground state and the first excited state. In particular, it is important that the gap Δ does not vanish anytime on the path of g taken in the adiabatic time evolution.

The algorithm is naively sketched in Figure 2.4.2.

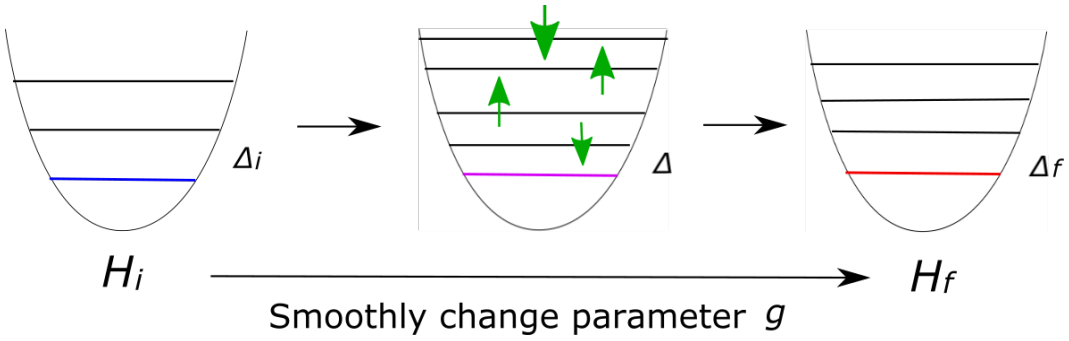

Figure 2.7: A naive sketch of the adiabatic state preparation with a family of Hamiltonian parameterized by a single parameter g.

A proton at rest is not the ground state of the entire QCD Hilbert space. However, one can still apply the adiabatic state preparation method by restricting the simulation to a sector of the Hilbert space which satisfies three conditions: gauge-invariant (in the context of Hamiltonian formulation as was discussed in the last section), translationally invariant (and thus has zero-momentum), and the baryon number 1. In this sector, the ground state is a proton at rest. Once we put a state in this sector on qubits, the state on quantum computer remains in the sector under the time-evolution via the family of QCD Hamiltonian. Thus the Adiabatic state preparation can be done in the following way:

1. One prepares a family of Lattice QCD Hamiltonian parameterized by the lattice coupling g.

2. The system starts with the free theory by setting $g = 0$, with which the ground state is three zero-momentum quarks. At zero coupling, the ground state of gauge fields is that each link being identity and quarks are free Gaussian wave functions. [1]

3. One slowly turns up the coupling g to a desired value while performing the time-evolution.

[1] A precise implementation of circuits to prepare such state should be worked out in future work.

The time-evolution keeps the system in the designated sector because the time evolution is gauge-invariant, conserves the momentum and the baryon number. As long as the change of g is done slowly enough, the system remains to be in its ground state. Thus we end up with the proton at rest at the end of the time evolution.

We shall estimate the cost of the state preparation algorithm described above. Along the adiabatic time evolution while varying g, the time evolution per time step costs always number of gates of order $\propto V$ where V is volume on the lattice (with a fixed lattice spacing). The remaining factor that contributes to the cost is the gap Δ. Firstly, at the beginning of the time-evolution with vanishing g, the massless gluon excitations need to be restricted by an appropriate boundary condition or the use of $S(1080)$ approximation to the $SU(3)$ gauge theory. Then the gap is a pair of fermions with back-to-back momentum, which is $\sim 1/L$ where $L^3 = V$. Thus the number of time steps required at the beginning scales as $\sim L^2$. The situation is better at the end of the time-evolution where the gap is the pion at rest ~ 135 MeV, so that the number of time steps needed in this part of the time-evolution does not scale with V. Thus the state preparation algorithm naively requires $L^2 \times V$ gate operations for a single state preparation.

2.4.3 Measurement of parton distribution functions

In this section, I discuss measurement algorithms of PDFs given that a proton state is prepared. The computation of PDFs of a proton with QCD involve measuring the quark-anti quark correlator on the light cone in Eq. (2.41). There are a couple of complications here. Firstly, the operator is neither Hermitian nor unitary. Secondly, the Wilson line $W(y;0)$ connecting quark operators lies on the light-cone, making its measurement very costly as will be discussed

later. To address the first complication without having the second complication involved, we take the massive Thirring model in $1+1$-dimension to illustrate the algorithm. Then we address the complication that arises from the Wilson line, which will lead us to considering a simpler object — the hadronic tensor.

Let us first introduce the Hamiltonian of the Thirring model in $1+1$D in the continuum:

$$H_{\text{cont}} = \bar{\psi}\left(-i\gamma^1\partial_1 + m\right)\psi + g^2\left(\bar{\psi}\gamma^\mu\psi\right)\left(\bar{\psi}\gamma_\mu\psi\right) \tag{2.43}$$

Here ψ and $\bar{\psi}$ are two-component spinor. We work in the Dirac basis so that $\gamma^0 = \sigma_x$ and $\gamma^1 = i\sigma_y$. As parameters of the Hamiltonian, we have mass m and the coupling constant g. As the discretization scheme of fermions, we choose staggered fermions. The resulting Hamiltonian on the lattice is

$$\begin{aligned} H_{\text{dis}} &= \sum_{x=1}^{N_s} m\,(-1)^x\,\chi^\dagger(x)\chi(x) + \frac{(-1)^x}{2}\left[\chi^\dagger(x)\chi(x+1) + \chi^\dagger(x+1)\chi(x)\right] \\ &- g^2\chi(x)\chi(x)^\dagger\chi^\dagger(x+1)\chi(x+1) \end{aligned} \tag{2.44}$$

where N_s is the number of sites and $\chi, \chi^\dagger$ are one-component spinors. Here I took the lattice spacing to be $a = 1$.

To write the Hamiltonian in terms of quantum gates available on the quantum computer, we apply the Jordan-Wigner transformation [48]:

$$\begin{aligned} \chi^\dagger(x) &= \sigma_z^1 \otimes \cdots \otimes \sigma_z^{x-1} \otimes \sigma_+^x \otimes I_2^{x+1} \otimes \cdots \otimes I_2^{N_s} \\ \chi(x) &= \sigma_z^1 \otimes \cdots \otimes \sigma_z^{x-1} \otimes \sigma_-^x \otimes I_2^{x+1} \otimes \cdots \otimes I_2^{N_s} \end{aligned} \tag{2.45}$$

Here, I_n are $n \times n$ identities, σ_i are Pauli matrices, and $\sigma_\pm = (\sigma_x \pm \sigma_y)/2$. The superscripts on the operators denote lattice sites. The resulting Thirring model Hamiltonian is $H = H_x + H_y + H_z + H_{zz}$ with

$$\begin{aligned} H_x &= \sum_{n=1}^{N_{s-1}} a_{xx}(n)\sigma_x(n)\sigma_x(n+1) \\ H_z &= \frac{g^2}{4}\sigma_z(1) - \frac{g^2}{4}\sigma_z(N_s) + \sum_{n=1}^{N_s} a_z(n)\sigma_z(n) \\ H_{zz} &= \sum_{n=1}^{N_{s-1}} a_{zz}(n)\sigma_z(n)\sigma_z(n+1) \end{aligned} \tag{2.46}$$

Coefficients are determined from the Jordan-Wigner transformation: $a_z(n) = m(-1)^n/2$, $a_{xx} = a_{yy}(n) = (-1)^{n+1}/4$, and $a_{zz}(n) = g^2/4$.

The PDFs of the Thirring model in $1+1$D in the continuum is given as

$$f_{\mathrm{T}}(x) = \int_{-\infty}^{\infty} \frac{dt}{2\pi} e^{-itx(n\cdot P)} \langle P|\bar{\psi}_q(tn^\mu)\gamma^+\psi_q(0)|P\rangle \tag{2.47}$$

Note that the Wilson line does not appear in the definition. For the purpose of a demonstration, the state $|P\rangle$ can be any bound states such as that of two fermions. The corresponding "staggered PDF" on the lattice is

$$f_{\mathrm{T,stag}}(x) = \langle P| \sum_{y,z} e^{ixP(y-z)} \left[\epsilon_{y,z} + i(-1)^z \epsilon_{y,z+1}\right] \times e^{iH(y-z)}\chi^\dagger(y)e^{-iH(y-z)}\chi(z)\,|P\rangle\,. \tag{2.48}$$

Here $\epsilon_{i,j} = 1$ when $i \mod 2 = j \mod 2$ and $\epsilon_{i,j} = 0$ otherwise. Thus the goal of quantum

computing is to evaluate the real-time correlator of the form

$$C(y,z) = \langle P| e^{iH(y-z)}\chi^\dagger(y)e^{-iH(y-z)}\chi(z)\,|P\rangle \tag{2.49}$$

As it is also the case with QCD, the operator to be measured is neither Hermitian nor unitary. The measurement of such correlator can be done by decomposing the observable into unitary pieces:

$$\begin{aligned} e^{iH(y-z)}\chi(y)e^{-iH(y-z)}\chi^\dagger(z) &= \sum_{i,j=x,y} C_{ij}U_{ij} && (2.50)\\ U_{ij} &= e^{iH(y-z)}\chi_i(y)e^{-iH(y-z)}\chi_j(z) && (2.51) \end{aligned}$$

Here χ and $\chi^\dagger$ are decomposed into unitary operations $\chi_x = \chi + \chi^\dagger$ and $\chi_y = i\left(\chi - \chi^\dagger\right)$. Coefficients are $C_{xx} = C_{yy} = 1/4, C_{xy} = -i/4, C_{yx} = i/4$. The expectation value of each unitary operator U_{ij} can be measured by inserting an ancillary qubit as is discussed in Sec. 2.3.2.

This leaves us to implement a sequence of gates that give controlled U_{ij} operations in Eq. (2.50). Firstly, $\chi_x(n)$ and $\chi_y(n)$ in U_{ij} operators simply become controlled σ_x and σ_y gates:

$$\begin{aligned} C_x(i,j) &= |0\rangle\langle 0| \otimes I_2 + |1\rangle\langle 1| \otimes \sigma_x && (2.52)\\ C_y(i,j) &= |0\rangle\langle 0| \otimes I_2 + |1\rangle\langle 1| \otimes \sigma_y && (2.53) \end{aligned}$$

The time evolution e^{-iHt} needs to be Trotterized and written in terms of local operations first:

$$e^{-iHt} \sim \prod_{i=1}^{N_t} e^{-iH_x dt}e^{-iH_y dt}e^{-iH_z dt}e^{-iH_{zz} dt} \tag{2.54}$$

with N_t the number of Trotter steps and $dt = t/N_t$ is taken to be small. Now one can approximate

each term by local time-evolution:

$$
\begin{aligned}
e^{-iH_x dt} &= \prod_{n=1}^{N_s-1} e^{-ia_{xx}(i)dt\times\sigma_x(n)\otimes\sigma_x(n+1)}, & e^{-iH_y dt} &= \prod_{n=1}^{N_s-1} e^{-ia_{yy}(i)dt\times\sigma_y(n)\otimes\sigma_y(n+1)} \\
e^{-iH_z dt} &= \prod_{n=1}^{N_s} e^{-i\tilde{a}_z(i)dt\times\sigma_z(n)}, & e^{-iH_{zz} dt} &= \prod_{n=1}^{N_s-1} e^{-ia_{zz}(i)dt\times\sigma_z(n)\otimes\sigma_z(n+1)}
\end{aligned}
\tag{2.55}
$$

Here $\tilde{a}$ are the modified coefficients a due to the boundary condition: $\tilde{a}(1) = -m + g^2/4$ and $\tilde{a}(N_s) = (-1)^{N_s} m - g^2/4$.

The following controlled gates are required to perform the Trotterized time evolution Eq. (2.55):

$$
\begin{aligned}
C_z(i,j) &= |0\rangle\langle 0| \otimes I_2 + |1\rangle\langle 1| \otimes \sigma_z && (2.56)\\
C_{rz}(\theta,i,j) &= |0\rangle\langle 0| \otimes I_2 + |1\rangle\langle 1| \otimes \exp(i\theta\sigma_z) && (2.57)\\
C_{rxx}(\theta,i,j,k) &= |0\rangle\langle 0| \otimes I_4 + |1\rangle\langle 1| \otimes \exp(i\theta\sigma_x \otimes \sigma_x) && (2.58)\\
C_{ryy}(\theta,i,j,k) &= |0\rangle\langle 0| \otimes I_4 + |1\rangle\langle 1| \otimes \exp(i\theta\sigma_y \otimes \sigma_y) && (2.59)\\
C_{rzz}(\theta,i,j,k) &= |0\rangle\langle 0| \otimes I_4 + |1\rangle\langle 1| \otimes \exp(i\theta\sigma_z \otimes \sigma_z)\ . && (2.60)
\end{aligned}
$$

All these controlled gates are implemented with primitive gates in a simple manner. In Qiskit's notation [100, 101], two-qubit gates $C_x(i,j), C_y(i,j), C_z(i,j)$ and $C_{rz}(i,j)$ are directly available — they are called $cx(i,j), cy(i,j), cz(i,j)$ and $crz(i,j)$ in Qiskit respectively. Three-qubit controlled gate $C_{rzz}(i,j,k)$ can be implemented by a sequence of Toffoli gate, $C_{rz}(i,k)$, and Toffoli gate. This is because the operator $e^{i\theta\sigma_x(j)\otimes\sigma_z(k)}$ is implemented by a sequence of $cx(j,k)$ (j: control qubit, k: target qubit), $rz(\theta,k)$, and $cx(j,k)$. So to implement $C_(rzz)$, we simply let these three gates controlled to ith qubit. The other three-qubit gates, $C_{rxx}(i,j,k)$ and $C_{ryy}(i,j,k)$, are implemented by sandwiching $C_{rzz}(i,j,k)$ with basis-change operators $z \to x$ (Hadamart) or

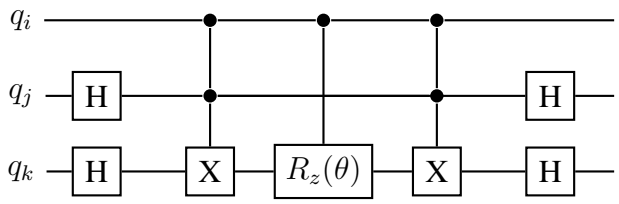

Figure 2.8: Quantum circuits for the three-qubit controlled gate $C_{rxx}(\theta, i, j, k)$ defined in Eq. (2.58).

$y \to x$ respectively on jth and kth qubits. The circuit for C_{rxx} is shown in Figure 2.8.

Now that all necessary circuits for the computation of PDFs in $1+1$-dimensional Thirring model have been constructed via primitive gates on a quantum computer, let us move onto compute a PDF for the Thirring model. For each $U_{i,j}$ in Eq. (2.50), I measure its expectation value on the state $|P\rangle$ by applying the controlled $U_{i,j}$ (constructed from the controlled gates above) to the controlled state $|P'\rangle$, and then measure σ_x, σ_y on the ancillary qubit to obtain the expectation value of $U_{i,j}$ on $|P\rangle$. Then I sum up those expectation values following Eq. (2.50) and obtain the whole correlator $C(y,z)$ in Eq. (2.49). These correlators must be Fourier-transformed according to Eq. (2.48) to be a parton distribution function. A naive Fourier transformation may yield highly oscillatory artifacts, which can be suppressed by a Gaussian window with a width σ:

$$f_{\mathrm{T,stag}}(x) = \lim_{\sigma\to 0}\lim_{L\to\infty} \langle P| \times \sum_{y,z} e^{ixP(y-z)-(y-z)^2/\sigma^2} \left[\epsilon_{y,z} + i(-1)^z \epsilon_{y,z+1}\right]$$
$$\times e^{iH(y-z)} \chi^\dagger(y) e^{-iH(y-z)} \chi(z) |P\rangle \tag{2.61}$$

As a demonstration shown in Figure 2.4.3, we computed the staggered PDF for $1+1$D Thirring model on 10 sites with two sets of parameters: $m = 1.5, g = 0.0$ and $m = 1.4, g = 0.4$. The Fourier transformation was taken with $\epsilon = 3$ for the Gaussian window in Eq. (2.61).

Ultimately, we would like to compute PDFs of hadrons from lattice QCD. With QCD, the

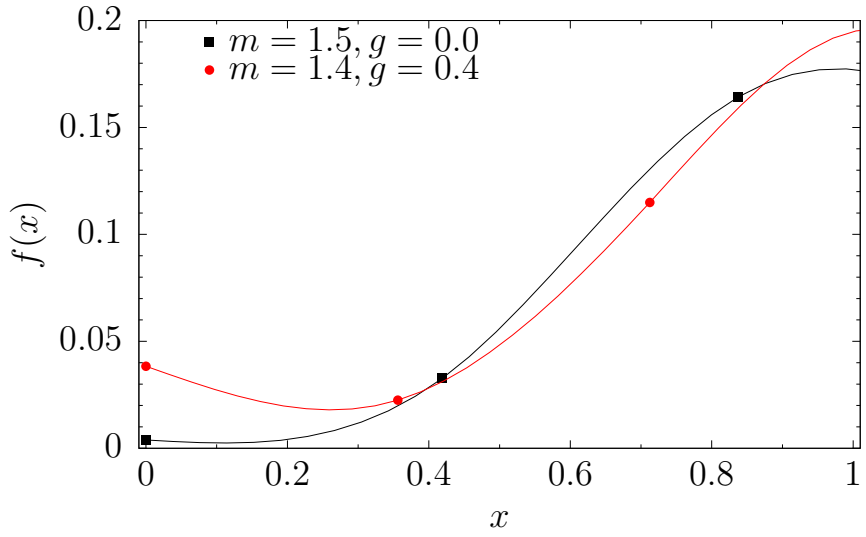

Figure 2.9: The fermion distribution of the lowest-lying fermion in the Thirring model with two sets of parameters: $m = 1.5, g = 0.0$ and $m = 1.4, g = 0.4$.

observable to be measured is the correlator of quark creation and annihilation operators connected via a Wilson line on the light cone as in Eq. (2.41):

$$C(y) = \langle P | \, \bar{\psi}_q(t\, n^\mu)\gamma^+ W(t\, n^\mu; 0)\psi_q(0) \, | P \rangle \tag{2.62}$$

The Wilson line can be approximated on the lattice by a sequence of gauge links at each Trotter step as

$$W(y;0) \approx U_{y,y-a}(t = y - a) \cdots U_{2a,a}(t = a)U_{a,0}(t = 0) \; . \tag{2.63}$$

Note that $A_0 = 0$ gauge is chosen for the temporal gauge links as usual. Following the method for measuring temporally-extended Wilson loop in Sec. 2.3.2, one can n principle measure the Wilson line on the light cone by perturbing the Hamiltonian via gauge links U at every time slices in $0 < t < y$. The number of numerical differentiation taken is exactly the number of time slices affected by the Wilson line. Such a high-order finite differencing is not practical as the Wilson

expends further in time and Hamiltonian limit a_0 is taken. This technical difficulty encourages us to find an alternative operator which does not involve Wilson lines but still provides information about the structure of hadrons. One of such objects is the Hadronic tensor, whose measurement method will be discussed in the next section.

2.4.4 Measurement of the hadronic tensor

Hadronic tensor is closely related to the deep inelastic scattering cross section. Together with the leptonic tensor

$$L_{\mu\nu} = 2\left(k_\mu k'_\nu + k_\nu k'_\mu - g_{\mu\nu} k \cdot k'\right), \tag{2.64}$$

the hadronic tensor is directly related the lepton-proton scattering cross section up to the leading order in QED coupling α

$$\frac{d^2\sigma}{dxdy} = \frac{\alpha^2 y}{Q^4} L_{\mu\nu} W^{\mu\nu}. \tag{2.65}$$

Here $Q^2 = -q^2$, q is the transfer momentum, $x = Q^2/(2P \cdot q)$, $y = (P \cdot q)/(P \cdot k)$, and $k'k - q$. As such, the quantum simulation of hadronic tensor is also simpler. The hadronic tensor can be computed as

$$W^{\mu\nu}(q) = \mathrm{Re} \int \mathrm{d}^d x \; e^{iqx} \left\langle P \right| T\left\{J^\mu(x) J^\nu(0)\right\} \left| P \right\rangle \tag{2.66}$$

where $J^\mu = \bar{\psi}\gamma^\mu\psi$ is the current, which is already gauge-invariant. Thus we need no Wilson lines between the two currents. As J^μ is Hermitian, instead of decomposing J^μ into unitary matrices, we follow the procedure for studying linear response [102] and simply measure the expectation value of the operator

$$U(\epsilon_x, \epsilon_0) = e^{iHt} e^{iJ^\mu(\vec{x})\epsilon_x} e^{-iHt} e^{-iJ^\nu(\vec{0})\epsilon_0}. \tag{2.67}$$

The second derivative of the expectation value gives the desired correlator:

$$\frac{\mathrm{d}}{\mathrm{d}\epsilon_x}\frac{\mathrm{d}}{\mathrm{d}\epsilon_0}\langle P|\, U(\epsilon_x,\epsilon_0)\,|P\rangle = \langle P|\, J^\mu(x)J^\nu(0)\,|P\rangle \tag{2.68}$$

Once such correlator is computed for multiple position x, the correrator should be Fourier transformed with a regulator to obtain the hadronic tensor in Eq. (2.66). Alternatively, the entire Fourier transformed operator can be measured on a quantum computer at once:

$$W^{\mu\nu}(q) = \langle P|\, T\left\{J^\mu(0)\int \mathrm{d}^d x\; e^{iqx-x^2/\epsilon}J^\nu(x)\right\}|P\rangle\,. \tag{2.69}$$

with the Gaussian window ϵ. In either case, the measurement of the hadronic tensor can be done in a much simpler way compared to the PDFs due to the gauge-invariace and the Hermiticity of the current J^μ. PDFs are in principle obtained from hadronic tensor as is discussed in [14].

2.5 Transport coefficients

2.5.1 Overview

Hydrodynamic transport coefficients, the shear viscosity and bulk viscosity, are shown to be the central constants for our understanding of the non-equilibrium properties of a strongly coupled quark gluon plasma. As is discussed in Sec. 1.4.3, to obtain hydrodynamic coefficients, the following kinds of correlators should be evaluated:

$$C(t,\vec{x}) = \langle\Psi(\beta)|\,[T_{\mu\nu}(t,\vec{x}),T_{\mu\nu}(0,0)]\,|\Psi(\beta)\rangle \tag{2.70}$$

with varying $(t, \vec{x})$. Here $T_{\mu\nu}$ is the $\mu\nu$ component of the energy-momentum tensor of QCD, and $\Psi(\beta)$ is the thermal state of QCD at an inverse temperature β. Lattice QCD calculations of such real-time correlators on a classical computer naively suffer from sign problems. Despite such numerical difficulties, efforts are made to obtain transport coefficients [103, 104, 105, 106, 107].

In this section, as an alternative method to theoretically obtain the transport coefficients from first-principles, we discuss quantum algorithms for computing the those transport coefficients in hydrodynamics in gauge theories [15]. The mapping of lattice gauge theories onto qubits in Sec. 2.2 and time evolution circuits in Sec. 2.3 can be used to accomplish the two building blocks of the quantum simulation in Figure 2.1. This section is devoted to a detailed discussion of state preparation algorithms and measurement procedures. As an initial state, a thermal state of the gauge theory at finite temperature should be prepared. For the measurement, we shall find operators $T_{\mu\nu}$ for lattice gauge theories and build an algorithm to measure their correlators. Once we obtain correlators, relations Eqs. (1.68,1.69,1.70) will let us extract transport coefficients from such correlation functions with a finite volume effect.

2.5.2 State preparation

The goal of the state preparation algorithm for transport coefficients in hydrodynamics is very different from that for PDFs. An ideal initial state would be a thermal state at a finite temperature in the regime of phase transition or crossover where the system is strongly coupled. Nevertheless, the kinds of tools we can use for such state preparation is still an adiabatic state preparation or other forms of time evolution circuits. In this section, we naively sketch ideas for the state preparation of QCD thermal states. However, before we proceed, the meaning

of a "thermal state" should be clarified, given that lattice QCD has only finite volume. In the infinite volume limit of the lattice, the microcanonical approach (with the focus on energy density) and the canonical approach (with focus on temperature) should agree. Thus if quantum simulations are performed close to the thermodynamic limit, one can either prepare a pure state with approximately correct energy density $\epsilon(T)$ corresponding to the desired temperature T, or can prepare a density matrix state with the temperature T. One expects that expectation values computed on those state will approximate the thermal expectation values well. On a finite-volume lattice, the finite-volume effects are expected to appear differently in those two approaches. In general, density matrix are expected to have a smaller finite volume effect for thermal expectation values. When our interest is on non-local observables or real-time correlators, the size of finite-volume effects may be so large that taking of the limit close to the thermodynamic limit on the lattice might be necessary. An efficient way, *i.e.* with a smaller finite volume effect, of taking the thermodynamic limit should be studied in the context of quantum simulation. In the following, we propose a couple of naive ideas for preparing thermal states, without specifying "which type" of thermal states to prepare in these algorithms. Such details of thermal states preparation and their finite volume effects should be studied in future work.

To design algorithms for preparing a thermal state at a finite temperature, it is useful to think about how a QCD finite temperature system is created in heavy-ion collisions. In experiment, we originally have a vacuum, in which we cause a high-energy collision of heavy nuclei. This collision creates a hot dense plasma of quarks and gluons. The fireball then expands, cools, and goes under the crossover or the phase transition, and becomes a low-temperature dilute gas of hadrons. We would like to stop the process of heavy-ion collision in the middle stage where the fireball is still strongly interacting. This can be done by simply putting the fireball in a finite-size

box, so that the system does not expand too much. On quantum computer, one has a finite-size system naturally by having a finite-size lattice. The remaining task is to start the collision. For quantum algorithms, there are two possible starting points: the vacuum and high-energy plasma. In the following, we first discuss the algorithm starting with a high-temperature state, and then the algorithm starting with a vacuum.

A high-energy state can be easily prepared on a quantum computer due to the lattice artifacts. One simply prepares a random gauge-invariant state and it will on average have an energy density of $\propto 1/a^4$, which is large when the lattice spacing a is taken to be small. Now, to prepare a state with lower energy density (or a lower temperature), one needs to extract energy from the system. Just as the system cools down by expanding into the vacuum in heavy-ion collisions, the cooling of the system can be done by attaching the vacuum of an appropriate size to the system on a quantum computer. One can prepare an even large system with a desired energy density, *i.e.* a heat bath, and attach the bath to the system. These ideas naively cost a lot of qubits while they still require a long time-evolution circuit $\propto V$. One can at least reduce qubit cost by performing an active cooling of the system via the "quantum refrigerator" (for a review of quantum refrigerators, see [108, 109]) The idea of quantum refrigerators is that one attaches a small vacuum to the system for an appropriate number of times. The quantum refrigerator may be a quantum system of the similar size as the system. The only requirement on the quantum refrigerator is that one needs to be able to set the refrigerator to the ground state. The quantum refrigerator can actively cool down the system by applying the following cycle (as sketched in Figure 2.5.2) many times:

1. One sets the refrigerator to the ground state.

2. One couples the refrigerator to the system in such a way that symmetry of the system, in particular gauge symmetry, is preserved. Then one performs the time evolution. As the refrigerator is in the ground state, the energy should on average flow from the system to the refrigerator.

3. The system is decoupled from the refrigerator.

The energy density is expected to decrease in each cycle, and the cycle should be repeated until the system's energy density decreases down to the desired energy density:

$$E_i > E_1 \geq E_2 \geq \cdots \geq E_{N-s-1} \geq E_{N_s} = E_f \tag{2.71}$$

If we are able to extract the same fraction of energy, (so keep E_n/E_{n-1} fixed for all cycles), the number of cycles required to cool the system down to the target energy density scales logarithmically with the ratio of the initial energy density E_i to the final density E_f:

$$N_s \propto \log\left(\frac{E_i}{E_f}\right) . \tag{2.72}$$

The proof or disproof of such scenarios should start by a more detailed construction of the algorithm.

An alternative approach to prepare a finite-temperature state is to start from the vacuum and add an appropriate amount of energy into the system (analogous to causing a heavy-ion collision in experiment). For the preparation of the ground state with desired lattice coupling g, we can again utilize the adiabatic state preparation described in Sec. 2.4.2. As an initial ground state of the adiabatic state preparation, one can start either in the strong coupling limit $g \to \infty$ or the

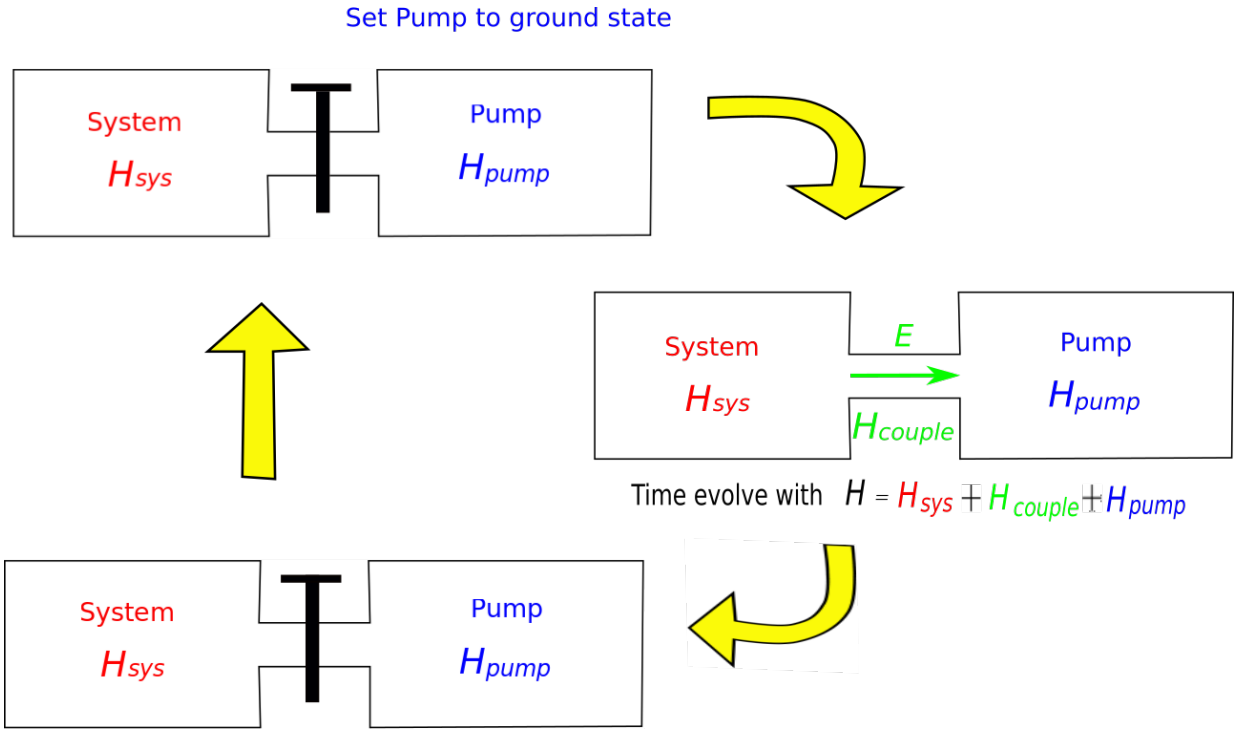

Figure 2.10: A schematic view of the quantum refrigerator.

weak coupling limit $g = 0$. The strong coupling is expected to work better for the following reasons. Firstly, the ground state at $\to \infty$ is the equal super position of all elements in the gauge group G for each link [110]:

$$|\Omega_{\text{strong}}\rangle = \otimes_U \left(\sum_{g \in G} |g\rangle \right) \tag{2.73}$$

which is already gauge invariant. On the other hand, the ground state in the zero-coupling limit, the ground state is the identity for all links, which is not gauge-invariant

$$|\Omega_{\text{weak}}\rangle = \otimes_U |I\rangle \tag{2.74}$$

so the gauge-projection operator needs to be applied. In addition to that, when it comes to truncating the gauge theory, the strong coupling ground state can be naturally implemented in

the same way for the $S(1080)$ gauge theory truncation, whereas the weak-coupling ground state for the $S(1080)$ gauge theory is not trivial.

Once one prepares a ground state in either way, the adiabatic state preparation should be performed — one applies the time-evolution while changing the lattice coupling constant g slowly toward the desired value. The gap Δ is an important factor to determine the cost of the algorithm. The gap Δ behaves differently at strong and week coupling limits. At a strong coupling, the gap is basically the mass of lowest glueball mass and thus a realistic physical coupling can be reached without encountering a small gap Δ. On the other hand, when one starts from the weak-coupling, the physical lattice spacing is small compared to the confinement scale, and the gap is likely to be very small. Thus additional treatments, such as explicit symmetry breaking, may be needed to create a sufficiently large gap and perform the adiabatic state preparation from the weak coupling limit.

Once we obtain the ground state with the physical coupling constant, one adds energy to the system. Since the system is in the ground of state, any operation to the qubits will in principle inject energy to the system. A more concrete approach is to employ the "quantum oven" (as opposed to the quantum refrigerator) and attach a small system with random state (which likely has a high energy density) to the system so that energy flows into the system. With any methods for adding energy to the system, one needs to be careful not to add too much energy into the system.

Finally, whether one starts from the high-energy state or the ground state to reach an appropriate energy density (or the corresponding temperature), the system needs to equilibrate by time evolving for an appropriate length of time. How long does it for a system to equilibrate? The thermalization of $\mathbb{Z}_2$ gauge theory is demonstrated in [111]. For QCD, once again, heavy-

ion collisions give us a hope. A hot plasma of quarks and gluons seems to equilibrate within the heavy-ion collision [11], suggesting that the thermalization of strongly coupled nuclear matter occurs in ~ 10 fm, which is of the same scale as the size of the lattice.

2.5.3 Measurement

A measurement of retarded correlators of a Hermitian operator $\mathcal{O}$ on a state $|\phi\rangle$ can be done very simply without any ancillary qubits or the decomposition of operators. One first defines a perturbed Hamiltonian by adding a small amount ϵ of $\mathcal{O}$ locally at time $t = 0$ to the Hamiltonian: $H' = H + \epsilon\delta(t)\mathcal{O}$. Then one time-evolves the initial state $|\psi\rangle$ with the perturbed Hamiltonian until time $t = t_1$ to obtain $|\phi(t_1)\rangle = e^{-iHt}e^{-i\epsilon\mathcal{O}}|\phi\rangle$. A measurement of $\mathcal{O}$ on $|\phi(t_1)\rangle$ yields

$$\langle\phi(t_1)|\mathcal{O}|\phi(t_1)\rangle = \langle\phi|\ e^{i\epsilon\mathcal{O}}\ e^{iHt}\ \mathcal{O}\ e^{-iHt}\ e^{-i\epsilon\mathcal{O}}\ |\phi\rangle\ . \tag{2.75}$$

By taking the derivative of the expectation value above with respect to ϵ and taking the limit $\epsilon \to 0$, one obtains the desired correlator:

$$\lim_{\epsilon\to 0}\frac{\partial}{\partial\epsilon}\langle\phi(t_1)|\mathcal{O}|\phi(t_1)\rangle = -i\langle\phi|\left[\mathcal{O}(t), \mathcal{O}(0)\right]|\phi\rangle\ . \tag{2.76}$$

In practice, we define the perturbed Hamiltonian with several different ϵ, measure the expectation values, and take the finite differencing.

This leaves us with deriving the expression for the energy-momentum tensor operators of gauge theories and implementing them. In the action formulation, the expression for the energy-

momentum tensor of gauge theories

$$T_{\mu\nu} = \frac{1}{4} g_{\mu\nu} \operatorname{Tr}\left[F_{\alpha\beta} F^{\alpha\beta}\right] - \operatorname{Tr}\left[F_{\mu\alpha} F^{\alpha}_{\nu}\right]. \tag{2.77}$$

on the lattice is well studied as is reviewed in Sec. 1.3.2. In this section, the metric tensor in Minkowski spacetime is chosen to be mostly-minus:

$$g_{\mu\nu} = \text{diag}(1, -1, -1, -1). \tag{2.78}$$

In the context of quantum simulations, we need the corresponding energy momentum tensor operators in the Hamiltonian formulation. To derive these operators, we simply follow the prescription in [90] for deriving the lattice gauge Hamiltonian from the action as reviewed in Sec. 2.3.1. A small modification is made to the derivation by perturbing the action with the lattice function of the EMT to obtain the EMT operators. In the action formulation, one way to obtain the expectation of an observable is to first define a generating functional:

$$Z_\epsilon = \int \mathcal{D}U \; e^{i(S_0 + \epsilon \mathcal{O}(t_0))}. \tag{2.79}$$

By differentiating this perturbed partition function with respect to ϵ,

$$i\langle \mathcal{O}(t_0) \rangle = Z_0^{-1} \left(\frac{\partial Z_\epsilon}{\partial \epsilon} \right)_{\epsilon \to 0}, \tag{2.80}$$

one obtains the desired expectation value. One can define a corresponding Hamiltonian formulation

by

$$\langle U'|e^{-ia_0 H_\epsilon}|U\rangle = e^{i(S+\epsilon\mathcal{O})}. \tag{2.81}$$

For the corresponding perturbed Hamiltonian, yet to be determined, to give the expectation value $\langle\mathcal{O}(t_0)\rangle$ in the same way, the perturbed Hamiltonian should satisfy

$$\hat{H}_\epsilon = \hat{H}_0 - \epsilon\hat{O}/a_0. \tag{2.82}$$

where H_0 is the original Hamiltonian of one's quantum system. So what I do in the following is to define the perturbed partition function Z_ϵ with a component of the EMT, and find the corresponding perturbed Hamiltonian H_ϵ which satisfies Eq. (2.81). Then I read off the operator expression for the EMT using Eq. (2.82). The components of EMT are categorized into three: diagonal components $T_{\mu\mu}$ in Sec. 2.5.3.1, spatial off-diagonal components T_{ij} in Sec. 2.5.3.2, and time-like off-diagonal components T_{0i} in Sec. 2.5.3.3. In each section, the operators that are correct up to $O(a^2)$ discretization errors are derived. All results of EMT operators are summarized in Table 2.5.3. Using lattice EMTs in the action formulation that are correct up to higher-order errors [22], corresponding operators with better approximations can be derived. When one uses such operators, improved lattice gauge Hamiltonian [112, 113, 114] must be used to implement the time-evolution to obtain the final result to be correct up to the desired higher-order discretization error.

Table 2.1: All gauge-invariant lattice operators needed to construct the energy momentum tensor operators in $3+1$ dimensions. Operators are all gauge invariant and Hermitian, and are derived to be correct up to $O(a)$ and $O(a^2, a_0)$ discretization errors. Operators $\hat{P}, \hat{C}, \hat{F}^N_{ij}, F^C_{ij}$ are the operator version of Eq. (1.14), Eq. (1.32), Eq. (1.31), and Eq. (1.33) respectively, given by converting all links (spatial) to the link operators defined in Eq. (2.9).

Operator	$O(a)$	$O(a^2)$
$\mathrm{Tr}\, F_{0i}F_{0i}(n)$	$\frac{g_s^2}{a^4}\,\mathrm{Tr}\left[\pi^2_{n,i}\right]$	$\sum_{x=0,1}\frac{g_s^2}{2a^4}\,\mathrm{Tr}\left[\pi^2_{n-x\hat{i},i}\right]$
$\mathrm{Tr}\, F_{0i}F_{0j}(n)$	$\frac{g_s^2}{a^4}\,\mathrm{Tr}\left[\pi_{n,i}\pi_{n,j}\right]$	$\frac{g_s^2}{4a^4}\Big(\mathrm{Tr}\left[\hat{\pi}_{n,i}\hat{\pi}_{n,j}\right] + \mathrm{Tr}\left[\hat{\pi}_{n,i}\hat{U}^\dagger_{n-\hat{j},j}\hat{\pi}_{n-\hat{j},j}\hat{U}_{n-\hat{j},j}\right]$ + $\mathrm{Tr}\left[\hat{U}^\dagger_{n-\hat{i},i}\hat{\pi}_{n-\hat{i}}\hat{U}_{n-\hat{i},i}\hat{\pi}_{n,j}\right]$ $+\mathrm{Tr}\left[\hat{U}^\dagger_{n-\hat{i},i}\hat{\pi}_{n-\hat{i},i}\hat{U}_{n-\hat{i},i}\hat{U}^\dagger_{n-\hat{j},j}\hat{\pi}_{n-\hat{j},j}\hat{U}_{n-\hat{j},j}\right]\Big)$
$\mathrm{Tr}\, F_{0j}F_{ij}(n)$	$-\frac{1}{a^4}\,\mathrm{Tr}\left[\hat{\pi}_{n,j}\,\mathrm{Im}\,\hat{P}_{ij}(n)\right]$	$-\frac{1}{2a^4}\Big(\mathrm{Tr}\left[\hat{\pi}_{n,j}\,\mathrm{Im}\,\hat{C}_{ij}(n)\right]$ $+\mathrm{Tr}\left[\hat{U}^\dagger_{n-\hat{j},j}\hat{\pi}_{n-\hat{j},j}\hat{U}_{n-\hat{j},j}\,\mathrm{Im}\,\hat{C}_{ij}(n)\right]\Big)$
$\mathrm{Tr}\, F_{ij}F_{ij}(n)$	$\frac{2}{g_s^2a^4}\,\mathrm{Re}\,\mathrm{Tr}\left[1-\hat{P}_{ij}(n)\right]$	$\sum_{x=0,1}\sum_{y=0,1}\frac{1}{2g_s^2a^4}\,\mathrm{Re}\,\mathrm{Tr}\left[1-\hat{P}_{ij}(n-x\hat{i}-y\hat{j})\right]$
$\mathrm{Tr}\, F_{ij}F_{kj}(n)$	$\mathrm{Tr}[\hat{F}^N_{ij}(n)\hat{F}^N_{kj}(n)]$	$\mathrm{Tr}[\hat{F}^C_{ij}(n)\hat{F}^C_{kj}(n)]$

2.5.3.1 $T_{\mu\mu}$ in the Hamiltonian formulation

The diagonal components of the EMT has two kinds of terms, both of which are familiar from the Wilson gauge action. There is F^2_{0i} which contains temporal plaquettes and F^2_{ij} which is purely spatial. Without the loss of generality, let us consider adding the following two terms to the action:

$$S_\epsilon = S_W + \epsilon a_0 a^3\,\mathrm{Tr}\left[F_{01}(n_0)^2 + F_{12}(n_0)^2\right]. \tag{2.83}$$

The perturbed Hamiltonian H_ϵ and the perturbed action S_ϵ should be connected via transfer matrix $T_\epsilon = e^{-ia_0 H_\epsilon}$ as

$$\langle U'|T_\epsilon|U\rangle = e^{iS_\epsilon} = e^{i(K_\epsilon + V_\epsilon)} \tag{2.84}$$

with

$$K_\epsilon(U', U) = K + \epsilon \frac{2a}{g_s^2 a_0} \operatorname{Re}\operatorname{Tr}\left[1 - U_{n_0,1} U'^{\dagger}_{n_0,1}\right] \tag{2.85}$$

$$V_\epsilon(U', U) = V + \epsilon \frac{2a_0}{g_s^2 a} \operatorname{Re}\operatorname{Tr}\left[1 - P_{12}(n_0)\right] \tag{2.86}$$

This relation defines the perturbed Hamiltonian. Using the primitive operators $\hat{U}_{n,i}$ in Eq. (2.9) and $\hat{R}_{n,i}$ in Eq. (2.11), the following operator serves as the transfer matrix satisfying Eq. (2.84):

$$\hat{T}_\epsilon = \int \mathcal{D}g \; e^{iK(g) + i\epsilon \frac{2a}{g_s^2 a_0} \mathrm{ReTr}[1 - g^\dagger_{n_0,1}] + i\hat{V}_\epsilon}. \tag{2.87}$$

Here we introduced some short-hand notation:

$$\int \mathcal{D}g \equiv \int_{g\in G} \prod_{n,i} dg_{n,i} \hat{R}_{n,i}(g_{n,i}) \tag{2.88}$$

$$K(g) \equiv \frac{a}{g_s^2 a_0} \sum_{n,i} \operatorname{Re}\left[1 - g^\dagger_{n,i}\right]. \tag{2.89}$$

The operator $\hat{V}_\epsilon$ consists of the plaquette operators $\hat{P}$ which acts on the Hilbert space of a spatial plaquette and return the value of the plaquette. The Hamiltonian $\hat{H}_\epsilon$ can in principle be obtained by taking the logarithm of T_ϵ. However, as was done for the Yang-Mills Hamiltonian, one can

simplify the expression by considering the limit $a_0 \to 0$ and taking saddle-point approximation:

$$\begin{aligned} \hat{T}_\epsilon \quad &\sim \quad \int dx\; e^{ix_\rho \hat{\pi}_\rho - x_\rho M_{\rho\sigma} x_\sigma + i\hat{V}_\epsilon} \\ &\text{with} \quad M_{\rho\sigma} = \frac{-ia}{2g_s^2 a_0}\delta_{\rho\sigma} - \epsilon \frac{ia}{g_s^2 a_0}\delta_{nn_0}\delta_{mn_0}\delta_{i1}\delta_{j1}\delta_{ab}. \end{aligned} \tag{2.90}$$

Here a short-hand notation was introduced for indices: $\rho = (n, i, a)$ and $\sigma = (m, j, b)$. Performing the Gaussian integral, one obtains, up to the linear order,

$$\hat{H}_\epsilon = \hat{H}_{KS} - \epsilon \left(\frac{g_s^2}{a} \operatorname{Tr}\left[\hat{\pi}^2_{n_0,1}\right] + \frac{2}{g_s^2 a} \operatorname{Re}\operatorname{Tr}\left[1 - \hat{P}_{12}(n_0)\right] \right). \tag{2.91}$$

Now the operators for $\operatorname{Tr}\left[\hat{F}_{01}(n_0)^2\right]$ and $\operatorname{Tr}\left[\hat{F}_{12}(n_0)^2\right]$ can be read off from the perturbed Hamiltonian. Note here that spatial plaquettes in $V_\epsilon(U', U)$ were directly converted to their operator forms, while temporal plaquettes in $K_\epsilon(U', U)$ needed to be converted to terms with momentum operators $\hat{\pi}$. We will see the same pattern for the rest of the section. By generalizing the result to other operators of the same kinds, one finds

$$\operatorname{Tr}\left[\hat{F}_{0i}(n_0)^2\right] = \frac{g_s^2}{a^4} \operatorname{Tr}\left[\hat{\pi}^2_{n_0,i}\right] \tag{2.92}$$

$$\operatorname{Tr}\left[\hat{F}_{ij}(n_0)^2\right] = \frac{2}{g_s^2 a^4} \operatorname{Re}\operatorname{Tr}\left[1 - \hat{P}_{ij}(n_0)\right]. \tag{2.93}$$

Now by combining those operators above, we construct the $\hat{T}_{\mu\mu}$ operators that are correct up to $O(a)$ as

$$\hat{T}_{00}(n_0) = \frac{g_s^2}{2a^4}\sum_i \mathrm{Tr}[\hat{\pi}^2_{n_0,i}] + \frac{1}{g_s^2 a^4}\sum_{i<j}\mathrm{Re}\,\mathrm{Tr}[1-\hat{P}_{ij}(n_0)] \tag{2.94}$$

$$\begin{aligned}\hat{T}_{ii}(n_0) &= \frac{g_s^2}{2a^4}\,\mathrm{Tr}\left[-\hat{\pi}^2_{n_0,i}+\hat{\pi}^2_{n_0,j}+\hat{\pi}^2_{n_0,k}\right] \\ &+ \frac{1}{g_s^2 a^4}\,\mathrm{Re}\,\mathrm{Tr}\left[1-\hat{P}_{ij}(n_0)-\hat{P}_{ik}(n_0)+\hat{P}_{jk}(n_0)\right]\,.\end{aligned} \tag{2.95}$$

A few remarks follow. Firstly, T_{00} is the Hamiltonian density of the Kogut-Susskind Hamiltonian in Eq. (2.19) up to a constant term. The trace of the EMT operator vanishes as was the case with in the action formulation Eq. (1.26). Finally, all these $T_{\mu\mu}$ operators are manifestly gauge-invariant and Hermitian.

The improvement of $\mathrm{Tr}\left[\hat{F}_{01}(n_0)^2\right]$ and $\mathrm{Tr}\left[\hat{F}_{12}(n_0)^2\right]$ operators up to $O(a^2)$ discretization errors can be achieved by simply taking the average of naive operators around the site in the plane that $F_{\mu\nu}$s lie:

$$\mathrm{Tr}\left[\hat{F}_{0i}(n_0)^2\right] = \sum_{x=0,1}\frac{g_s^2}{2a^4}\,\mathrm{Tr}\left[\hat{\pi}^2_{n_0-x\hat{i},i}\right] \tag{2.96}$$

$$\mathrm{Tr}\left[\hat{F}_{ij}(n_0)^2\right] = \sum_{x=0,1}\sum_{y=0,1}\frac{1}{2g_s^2 a^4}\,\mathrm{Re}\,\mathrm{Tr}\left[1-\hat{P}_{ij}(n_0-x\hat{i}-y\hat{j})\right]. \tag{2.97}$$

Note that for $\mathrm{Tr}\left[\hat{F}_{0i}(n_0)^2\right]$ the average of two plaquettes lying in the remaining i direction was taken as we do not need to improve the discretization error from a_0 up to $O(a_0^2)$. For the space-like $\mathrm{Tr}\left[\hat{F}_{ij}(n_0)^2\right]$ one needs to take the average of four plaquettes in both i and j direction. These improved operators let us construct $T_{\mu\mu}$ operators that are correct up to $O(a^2, a_0)$ discretization

errors.

2.5.3.2 T_{ij} in the Hamiltonian formulation

The spacial off-diagonal components of the energy momentum tensor reads

$$T_{ij} = \mathrm{Tr}\left[-F_{i0}F_{j0} + F_{ik}F_{jk}\right]. \tag{2.98}$$

As was seen in the previous section, the first term consisting of temporal plaquettes needs to be written with momentum operators π in the Hamiltonian formulation. On the other hand, the second term will be converted simply to the spatial plaquette operators. For lattice operators, we will first work with the naive discretization Eq. (1.31), and then use clovers Eq. (1.33) and half-clovers Eq. (1.35) to improve operators up to $O(a^2)$ errors. To start, let us perturb the Wilson action as

$$K_\epsilon = K + \epsilon a_0 a^3 \,\mathrm{Tr}\left[F^N_{10}F^N_{20}\right] \tag{2.99}$$

$$V_\epsilon = V + \epsilon a_0 a^3 \,\mathrm{Tr}\left[F^N_{13}F^N_{23}\right]. \tag{2.100}$$

The transfer matrix $\hat{T}_\epsilon$ is now defined via Eq. (2.84) with these appropriate perturbation K_ϵ and V_ϵ above. The operator $\hat{T}_\epsilon$ can be written with the primitive operators Eq. (2.9) and Eq. (2.11) as

$$\hat{T}_\epsilon = \int \mathcal{D}g \; e^{iK(g) - i\epsilon \frac{a}{4g_s^2 a_0}\mathrm{Tr}\left[(g^\dagger_{n_0,1} - g_{n_0,1})(g^\dagger_{n_0,2} - g_{n_0,2})\right] + i\hat{V}_\epsilon}. \tag{2.101}$$

In the Hamiltonian limit, saddle approximation at $x = 0$ gives

$$\begin{aligned} \hat{T}_\epsilon \;\sim\; & \int dx\; e^{ix_\rho \hat{\pi}_\rho - x_\rho M_{\rho\sigma} x_\sigma + i\hat{V}_\epsilon} = A e^{-\frac{1}{4}\hat{\pi}_\rho M^{-1}_{\rho\sigma}\hat{\pi}_\sigma + i\hat{V}_\epsilon} \\ & M_{\rho\sigma} = \frac{-ia}{2g_s^2 a_0}\delta_{\rho\sigma} + \epsilon\frac{ia}{g_s^4 a_0}\delta_{nn_0}\delta_{mn_0}\delta_{i1}\delta_{j2}\delta_{ab}\;. \end{aligned} \tag{2.102}$$

Up to the linear order in ϵ, one obtains the perturbed Hamiltonian $\hat{H}_\epsilon$ to be

$$\hat{H}_\epsilon = \hat{H}_{KS} - \epsilon\frac{g_s^2}{a}\,\mathrm{Tr}[\hat{\pi}_{n_0,1}\hat{\pi}_{n_0,2}] - \epsilon a^3\,\mathrm{Tr}\left[\hat{F}^N_{ik}(n_0)\hat{F}^N_{jk}(n_0)\right]\;. \tag{2.103}$$

The temporal part $\mathrm{Tr}\left[F^N_{10}F^N_{20}\right]$ can be read off from the second term in $\hat{H}_\epsilon$ as

$$\mathrm{Tr}\left[\hat{F}^N_{i0}\hat{F}^N_{j0}(n_0)\right] = \frac{g_s^2}{a^4}\,\mathrm{Tr}[\hat{\pi}_{n_0,i}\hat{\pi}_{n_0,j}]\;. \tag{2.104}$$

Thus the operator $\hat{T}_{ij}(n_0)$ with the naive discretization is

$$\hat{T}^N_{ij}(n_0) = -\frac{g_s^2}{a^4}\,\mathrm{Tr}\left[\hat{\pi}_{n_0,i}\hat{\pi}_{n_0,j}\right] + \mathrm{Tr}\left[\hat{F}^N_{ik}(n_0)\hat{F}^N_{jk}(n_0)\right]\;. \tag{2.105}$$

Clovers defined in Eq. (1.32) and half-clovers defined in Eq. (1.34) allow us to improve the operator $\hat{T}_{ij}$ up to $O(a^2, a_0)$ discretization errors. The spatial part $F_{ik}F_{jk}$ is simply improved by using the clover operator as

$$\hat{F}_{ik}\hat{F}_{jk}(n) = \hat{F}^C_{ik}(n)\hat{F}^C_{jk}(n) + O(a^2). \tag{2.106}$$

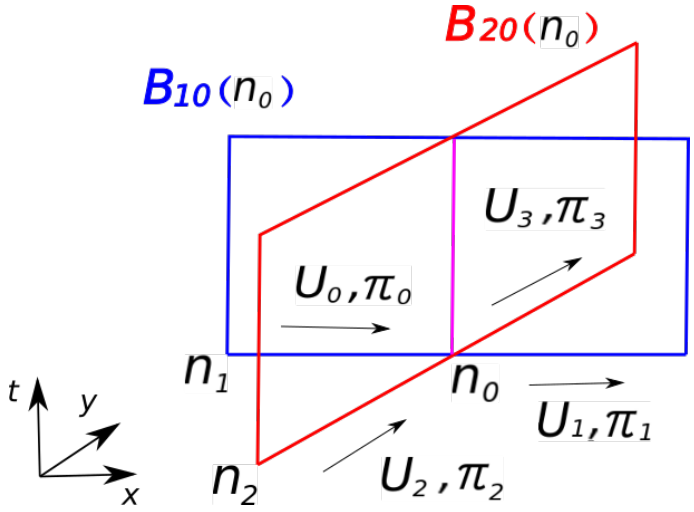

Figure 2.11: Half-clovers $B_{10}(n_0)$ and $B_{20}(n_0)$ and short-hand notations for links involved.

For the rest of the section, I focus on the temporal part $F_{i0}F_{j0}$, starting by the following perturbation

$$K_\epsilon(U', U) \;=\; K + \epsilon a_0 a^3 \,\mathrm{Tr}\left[F^B_{10}(n_0) F^B_{20}(n_0)\right] . \tag{2.107}$$

Links around the site n_0 was denoted as shown in Figure 2.11 to simplify expressions. The following transfer matrix operator satisfies the relation in Eq. (2.84) with the perturbation above:

$$\hat{T}_\epsilon = \int \mathcal{D}g\, e^{iK(g) - i\frac{\epsilon a}{16 g_s^2 a_0}\mathrm{Tr}\left[(g_1^\dagger - g_1 + \hat{U}_0^\dagger(g_0^\dagger - g_0)\hat{U}_0)(g_3^\dagger - g_3 + \hat{U}_2^\dagger(g_2^\dagger - g_2)\hat{U}_2)\right] + i\hat{V}} . \tag{2.108}$$

After the saddle-point approximation at $x = 0$, the expression for the transfer matrix simplifies:

$$\begin{aligned} \hat{T}_\epsilon \;&\sim\; \int dx\; e^{ix_\rho \hat{\pi}_\rho - x_\rho M_{\rho\sigma} x_\sigma + i\hat{V}} = A e^{-\frac{1}{4}\hat{\pi}_\rho M^{-1}_{\rho\sigma}\hat{\pi}_\sigma + i\hat{V}} \\ &\text{with } M_{\rho\sigma} = -\frac{ia}{2g_s^2 a_0}\delta_{\rho\sigma} - \frac{i\epsilon a}{4 g_s^2 a_0}(M_1)_{\rho\sigma} \end{aligned} \tag{2.109}$$

where matrix elements of $(M_1)_{\rho\sigma}$ are zero except

$$\begin{aligned}
(M_1)_{(n_0,1,a)(n_0,2,b)} &= \delta_{ab}, & (M_1)_{(n_0,1,a)(n_2,2,b)} &= \mathrm{Tr}\left[\lambda^a \hat{U}_2^\dagger \lambda^b \hat{U}_2\right] \\
(M_1)_{(n_1,1,a)(n_0,2,b)} &= \mathrm{Tr}\left[\hat{U}_0^\dagger \lambda^a \hat{U}_0 \lambda^b\right], & (M_1)_{(n_1,1,a)(n_2,2,b)} &= \mathrm{Tr}\left[\hat{U}_0^\dagger \lambda^a \hat{U}_0 \hat{U}_2^\dagger \lambda^b \hat{U}_2\right]
\end{aligned} \tag{2.110}$$

Sites n_1 and n_2 are as introduced in Figure 2.11. By expanding Eq. (2.109) up to the linear order in ϵ, I obtain

$$H_\epsilon = H_{K,S} - \epsilon \frac{g_s^2}{4a}\left(\mathrm{Tr}\left[\hat{\pi}_1 \hat{\pi}_3\right] + \mathrm{Tr}\left[\hat{\pi}_1 \hat{U}_2^\dagger \hat{\pi}_2 \hat{U}_2\right] + \mathrm{Tr}\left[\hat{U}_0^\dagger \hat{\pi}_0 U_0 \hat{\pi}_3\right] + \mathrm{Tr}\left[\hat{U}_0^\dagger \hat{\pi}_0 \hat{U}_0 \hat{U}_2^\dagger \hat{\pi}_2 \hat{U}_2\right] \right). \tag{2.111}$$

The result can be generalized to general $F_{i0}^B \hat{F}_{j0}^B$ straightforwardly:

$$\begin{aligned}
\mathrm{Tr}\left[\hat{F}_{i0}^B \hat{F}_{j0}^B(n_0)\right] = \frac{g_s^2}{4a^4}\Bigg(& \mathrm{Tr}\left[\hat{\pi}_{n_0,i} \hat{\pi}_{n_0,j}\right] + \mathrm{Tr}\left[\hat{\pi}_{n_0,i} \hat{U}^\dagger_{n_0-\hat{j},j} \hat{\pi}_{n_0-\hat{j},j} \hat{U}_{n_0-\hat{j},j}\right] \\
& + \mathrm{Tr}\left[\hat{U}^\dagger_{n_0-\hat{i},i} \hat{\pi}_{n_0-\hat{i}} \hat{U}_{n_0-\hat{i},i} \hat{\pi}_{n_0,j}\right] + \mathrm{Tr}\left[\hat{U}^\dagger_{n_0-\hat{i},i} \hat{\pi}_{n_0-\hat{i},i} \hat{U}_{n_0-\hat{i},i} \hat{U}^\dagger_{n_0-\hat{j},j} \hat{\pi}_{n_0-\hat{j},j} \hat{U}_{n_0-\hat{j},j}\right] \Bigg).
\end{aligned} \tag{2.112}$$

With these operators and spatial clover operators in Eq. (2.106), operators for the off-diagonal spatial components, $\hat{T}_{ij}$, are constructed to be correct up to $O(a^2, a_0)$ discretization errors.

2.5.3.3 T_{0i} in the Hamiltonian formulation

In this section, I derive operators for the off-diagonal time-like components of $T_{\mu\nu}$. All terms in T_{0i} contain temporal plaquettes, and thus need to be converted to combinations of gauge link operators $\hat{U}$ and momentum operators $\hat{\pi}$. We again work with the naive discretization (via

Eq. (1.31)) first and then improve operators using clovers Eq. (1.33) and half-clovers Eq. (1.35).

Let us take T_{01} as an example

$$T_{01} = \mathrm{Tr}\left[F_{02}F_{12} + F_{03}F_{13}\right] = \mathrm{Tr}\left[F^N_{02}F^N_{12} + F^N_{03}F^N_{13}\right] + O(a). \tag{2.113}$$

As both terms have the same form of $\mathrm{Tr}\left[F_{0j}F_{ij}\right]$, I focus on the first term for now and perturb the action as

$$K_\epsilon(U', U) = K + \epsilon a^3 a_0 \,\mathrm{Tr}\left[F^N_{02}F^N_{12}\right]. \tag{2.114}$$

The perturbed transfer matrix $\hat{T}_\epsilon$ is again defined via Eq. (2.84). The operator $\hat{T}_\epsilon$ can be written with the help of primitive operators Eq. (2.9) and Eq. (2.11) as

$$\hat{T}_\epsilon = \int \mathcal{D}g \; e^{iK(g) - \frac{i\epsilon}{4g_s^2}\mathrm{Tr}\left[(g_{n_0,2} - g^\dagger_{n_0,2})(\hat{P}_{12}(n_0) - \hat{P}^\dagger_{12}(n_0))\right] + i\hat{V}}. \tag{2.115}$$

In the Hamiltonian limit $a_0 \to 0$, saddle-point approximation around $x = 0$ simplifies the integral:

$$\begin{aligned} \hat{T}_\epsilon &\sim \int dx \; e^{\frac{ia}{2g_s^2 a_0} x_\rho \delta_{\rho\sigma} x_\sigma + i x_\rho \hat{\pi}'_\rho + i\hat{V}} \\ \text{where } \hat{\pi}'_\rho &= \hat{\pi}_\rho + \frac{\epsilon}{g_s^2}\delta_{nn_0}\delta_{i2}\,\mathrm{Tr}\left[\lambda^b \,\mathrm{Im}\,\hat{P}_{12}(n_0)\right]. \end{aligned} \tag{2.116}$$

Evaluating the Gaussian integral, one obtains, up to the linear order in ϵ,

$$\hat{H}_\epsilon = \hat{H}_{KS} + \epsilon \frac{1}{a}\,\mathrm{Tr}\left[\hat{\pi}_{n_0,2}\,\mathrm{Im}\,\hat{P}_{12}(n_0)\right]. \tag{2.117}$$

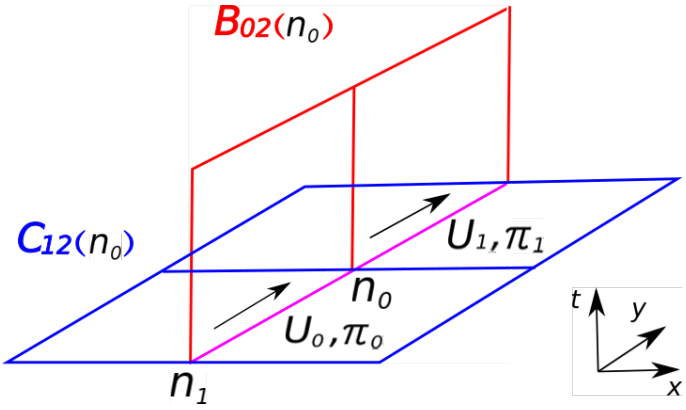

Figure 2.12: Clover $C_{12}(n_0)$, half-clover $B_{02}(n_0)$, and short-hand notations for links involved.

The operator for $\mathrm{Tr}\left[F^N_{02}F^N_{12}\right]$ can be read off from the second term as

$$\mathrm{Tr}\left[\hat{F}^N_{02}\hat{F}^N_{12}(n_0)\right] = -\frac{1}{a^4}\,\mathrm{Tr}\left[\hat{\pi}_{n_0,2}\,\mathrm{Im}\,\hat{P}_{12}(n_0)\right]. \tag{2.118}$$

By generalizing the result to operators of the form $\mathrm{Tr}\,[F_{0j}F_{ij}]$, one can construct $\hat{T}_{0i}$ operators with the naive discretization as

$$\hat{T}_{0i}(n_0) = -\sum_{j\neq i}\frac{1}{a^4}\,\mathrm{Tr}\left[\hat{\pi}_{n_0,j}\,\mathrm{Im}\,\hat{P}_{ij}(n_0)\right]. \tag{2.119}$$

To improve operators up to $O(a^2, a_0)$ discretization errors, one can use clovers in Eq. (1.32) and half-clovers in Eq. (1.34). I again add $F_{01}F_{12}$ to the Wilson action as

$$K_\epsilon(U', U) \;=\; K + \epsilon a^3 a_0\,\mathrm{Tr}\left[F^B_{02}(n_0)F^C_{12}(n_0)\right] \tag{2.120}$$

Here I introduce short-handed notations for relevant links around the site n_0 as denoted in Figure 2.12. The corresponding transfer matrix can be written as

$$\hat{T}_\epsilon = \int \mathcal{D}g \; e^{iK(g) - i\frac{\epsilon}{8g_s^2}\mathrm{Tr}\left[(g_1 - g_1^\dagger + \hat{U}_0^\dagger(g_0 - g_0^\dagger)\hat{U}_0)(\hat{C}_{12}(n_0) - \hat{C}_{12}^\dagger(n_0))\right] + i\hat{V}} \tag{2.121}$$

which can be simplified by the saddle-point approximation around $x = 0$ in the $a_0 \to 0$ limit as

$$\hat{T}_\epsilon \sim \int \quad dx \quad e^{\frac{ia}{2g^2 a_0} x_\rho \delta_{\rho\sigma} x_\sigma + i x_\rho \hat{\pi}'_\rho + i\hat{V}} \tag{2.122}$$

$$\hat{\pi}'_\rho = \hat{\pi}_\rho \quad + \quad \frac{\epsilon}{2g_s^2}\delta_{nn_0}\delta_{i2}\left(\mathrm{Tr}\left[\lambda^a \,\mathrm{Im}\,\hat{C}_{12}(n_0)\right] + \mathrm{Tr}\left[\hat{U}_0^\dagger \lambda^a \hat{U}_0 \,\mathrm{Im}\,\hat{C}_{12}(n_0)\right]\right) \tag{2.123}$$

Here $\hat{C}$ is the clover operator. Up to the linear order in ϵ, we obtain the perturbed Hamiltonian as

$$\hat{H}_\epsilon = \hat{H}_{KS} + \epsilon\frac{1}{2a}\left(\mathrm{Tr}\left[\hat{\pi}_1 \,\mathrm{Im}\,\hat{C}_{12}(n_0)\right] + \mathrm{Tr}\left[\hat{U}_0^\dagger \hat{\pi}_0 \hat{U}_0 \,\mathrm{Im}\,\hat{C}_{12}(n_0)\right]\right). \tag{2.124}$$

We read off the expression for the general $\hat{F}_{0j}^B \hat{F}_{ij}^C$ as

$$\begin{aligned}\mathrm{Tr}\left[\hat{F}_{0j}^B \hat{F}_{ij}^C(n_0)\right] \quad &= \quad -\frac{1}{2a^4}\left(\mathrm{Tr}\left[\hat{\pi}_{n_0,j} \,\mathrm{Im}\,\hat{C}_{ij}(n_0)\right]\right. \\ &+ \quad \left.\mathrm{Tr}\left[\hat{U}^\dagger_{n_0-\hat{j},j}\hat{\pi}_{n_0-\hat{j},j}\hat{U}_{n_0-\hat{j},j} \,\mathrm{Im}\,\hat{C}_{ij}(n_0)\right]\right).\end{aligned} \tag{2.125}$$

All off-diagonal time-like components of $\hat{T}_{\mu\nu}$, $\hat{T}_{0i}$, can be constructed from operators in Eq. (2.125) to be correct up to $O(a^2, a_0)$ discretization error.

Chapter 3: Sign Problems

3.1 The real-time sign problem

Lattice QCD calculations have successfully addressed many problems in QCD and have given us a tremendous amount of insight into the theory of strong interactions. However, there are still observables yet to be computed by lattice QCD, including ones of relevance to heavy-ion collisions, in both Euclidean and Minkowski lattice calculations due to the so-called sign problem. In this chapter, new ideas and insights into sign problems are discussed based on [17, 115]. Firstly, this section briefly reviews the origin of sign problems and some of the methods for alleviating sign problems in QCD. In Sec. 3.2, one of such methods, the *manifold deformation* method [16], is reviewed. The manifold deformation method is very closely related to yet another approach to the sign problem, the *complex normalizing flow* [17], which will be introduced in Sec. 3.3. For both manifold deformation methods and complex normalizing flows, their applicability to lattice field theories of one's interest is a central question to be addressed, as will be discussed in Sec. 3.4. Finally in Sec. 3.5, numerical methods based on machine learning to solve sign problems in the framework of the manifold deformation method and complex normalizing flows will be explored.

To illustrate sign problems, let us introduce a generic notation for the action as S and its

partition function as Z where

$$Z = \int \mathcal{D}[\phi] e^{-S(\phi)}. \tag{3.1}$$

Here, the path integral can be defined in Minkowski space, Euclidean space, or with Schwinger-Keldysh contours as introduced in Sec. 1.3.1, with an appropriate choice of the action S. The path integral in Minkowski spacetime is often denoted with the weight e^{iS_M} (instead of e^{-S}) where S_M is the Minkowski action. In our convention above, Minkowski actions take complex values: $S = -iS_M$. Throughout the rest of the chapter, I refer to the weight e^{-S} as the "Boltzmann factor" no matter which part of the Schwinger-Keldysh contour the weight is associated with. In the path integral above, ϕ represents all field degrees of freedom on the lattice, such as all gauge links in lattice QCD path integral in Eq. (1.24). As introduced in Sec. 1.3.1, the Boltzmann factor e^{-S} for lattice QCD is defined with the action $S = S_W - \log\det D$ where S_W is the Wilson gauge action and D is the Dirac matrix as was introduced in Eq. (1.23). At a finite baryon chemical potential, even in Euclidean lattice QCD calculations, the Boltzmann factor takes complex values due to the Dirac determinant $\det D$ [116]. This is the so-called finite density sign problem. For lattice QCD in Minkowski spacetime, the Boltzmann factor takes complex values due to the factor "i" in front of the Wilson gauge action. This is the so-called real-time sign problem. In both cases, the Boltzmann factor can no longer be regarded as the probability distribution function for the fields ϕ on the lattice, and Monte Carlo samplings cannot be performed with the naive Boltzmann factor. One way to define a probability distribution function within this path integral formalism is to introduce a quenched distribution function $e^{-\operatorname{Re} S(\phi)}$, which is real and positive for all configurations of ϕ. One can in principle perform Markov chain Monte Carlo (MCMC) sampling with the quenched distribution function and compute observables in lattice QCD. The

introduction of the quenched distribution requires that the ratio of two expectation values be taken:

$$\langle \mathcal{O} \rangle = \frac{\int \mathcal{D}[\phi]\ e^{-S}\ \mathcal{O}(\phi) / \int \mathcal{D}[\phi]\ e^{-\operatorname{Re} S}}{\int \mathcal{D}[\phi]\ e^{-S} / \int \mathcal{D}[\phi]\ e^{-\operatorname{Re} S}} = \frac{\langle \mathcal{O}\ e^{-i \operatorname{Im} S} \rangle_Q}{\langle e^{-i \operatorname{Im} S} \rangle_Q}. \tag{3.2}$$

Unfortunately, both the numerator and the denominator are numerically challenging to compute on the lattice. As an example, let us examine what we expect to obtain for the denominator, the so-called average sign $\langle \sigma \rangle = \langle e^{-i \operatorname{Im} S} \rangle_Q$. In the presence of a sign problem, the average sign is strictly smaller than 1, and it is expected to scale exponentially with the volume [110],

$$\langle \sigma \rangle \sim a^V, \quad |a| < 1 \tag{3.3}$$

when the action has only local interactions, which is often the case for lattice field theories of our interest. When the action S has only local interactions, one can naively view the numerator and the denominator of its average sign, the partition function Z and the quenched partition function Z_Q respectively, as a product of the "local Z" and "local Z_Q", *i.e.*,

$$Z(V) \sim Z(V/2)^2, \quad Z_Q(V) \sim Z_Q(V/2)^2\ . \tag{3.4}$$

Here $Z(V)$ and $Z_Q(V)$ are the partition function and the quenched partition function of a lattice with volume V respectively. Therefore, it follows that the resulting average sign with volume V, $\langle \sigma \rangle(V)$, can be also written as

$$\langle \sigma \rangle(V) \sim \langle \sigma \rangle(V/2)^2 \tag{3.5}$$

which leads one to the exponential scaling of the average sign in Eq. (3.3). On the other hand,

sampled values of the average sign are always a complex number with the magnitude of 1 (on the unit circle). Therefore, the number of samples required in MCMC sampling scales as $\sim e^{2V}$ to resolve the average sign from zero.

Sign problems exist not only in QCD but also in a wide range of fields in physics. Due to its significance, extensive work has been done to explore methods for solving or alleviating sign problems. As it is unlikely that a general solution to sign problems exists [117], solutions to sign problems are expected to be more or less problem-dependent. For example, regarding the finite-density sign problem (see, *e.g.* [118] for a review), explored ideas include reweighting methods [119], the complex Langevin method [120], the density of states methods [121], canonical methods [122, 123], the fermion bag approach [124], analytic continuation from imaginary chemical potential [125], and perturbative removal of a sign problem [126]. The rest of the section is devoted to discuss an extension of yet another method called the manifold deformation method (see [16] for a review).

3.2 Manifold deformation methods

One long-standing method to alleviate sign problems is the manifold deformation method. As will be described in detail in the following, the basic idea of the method is to deform the contour of integration in the path integral to the "complex plane", aiming for a milder sign problem. There has been a family of ideas for the manifold deformation method starting with the Lefschetz thimbles [127, 128, 129, 130]. The Lefschetz thimbles have been generalized to the generalized thimble method [131], which has been applied to bosonic and fermionic systems at finite density [132, 133, 134, 135, 136], real-time sign problems [137, 138], and

gauge theory [139]. Due to the numerical cost in finding such generalized thimbles, a method to machine-learn manifolds has been proposed [140]. More related to the topic of this chapter, to overcome numerical issues with the generalized thimble method, the sign-optimized manifold method was introduced in [141, 142]. The basic idea of the sign-optimized manifold is to prepare a family of manifolds of integration parameterized by several parameters, and numerically optimize the parameters (and thus the manifold of integration) within the family such that the average sign is maximized. The method has been applied to fermionic systems in [143, 144]. This approach, "the preparation a family of manifolds", remains as the key concept in a new method, *complex normalizing flow*, which will be introduced in Sec. 3.3. To start, in this section, I summarize the basic idea of the manifold deformation method.

The idea of the manifold deformation method is simple. To illustrate the problem, let us take an action $S(\phi)$ where the fields ϕ take real values. For example, for the lattice $SU(3)$ gauge theory, eight real values parameterizing elements $g \in SU(3)$ on each link can be regarded as such ϕ fields. Therefore, the domain of real values ϕ take depends on the lattice field theory of one's interest. For example, ϕ takes $\phi \in \mathbb{R}^N$ for real scalar field theories with N real degrees of freedom. Fields ϕ can also have a compact space, for example $\phi \in [-\pi, \pi)$ for each degree of freedom in $U(1)$ gauge theory and the Thirring model [144]. Given the original domain of integration of the path integral, the idea of the manifold deformation method is to deform the contour of integration in the path integral from the original domain in $\mathbb{R}$ to a manifold $\mathcal{M}$ in the corresponding complex plane $\mathbb{C}$. As a consequence of such a smooth deformation, the new manifold $\mathcal{M}$ is expected to be parameterizable by the same number of real variables as the original integration domain has. The goal of the deformation is to find a new manifold of integration which has a larger average sign and thus a milder sign problem.

The equivalence of physics on the original integration domain and the deformed manifold $\mathcal{M}$ is guaranteed by the multi-dimensional Cauchy's theorem as is discussed in detail in [110]. To be more precise, the expectation value of an observable (lattice function) $\mathcal{O}(\phi)$ is guaranteed to be the same on the original domain of integration and $\mathcal{M}$ by the Cauchy's integral theorem when the following three conditions are met:

1. The manifold $\mathcal{M}$ is a continuous manifold, obtainable by a continuous deformation of the original domain of integration.

2. The integrands, $e^{-S(\phi)}$ and $\mathcal{O}(\phi)e^{-S(\phi)}$, are holomorphic functions in the region between the original integration domain and $\mathcal{M}$, scanned by the deformation of the manifold from the real plane to $\mathcal{M}$.

3. The asymptotic behavior of the manifold remains the same. For example, for ϕ that takes value from a compact space like on a unit circle, the manifold should be closed as shown in Figure 3.1. For the contour with a gap as shown on the right panel of Figure 3.1 to be allowed, the contribution from the gap in the dashed line to the path integral has to vanish, which cannot be the case as the Boltzmann factor has to be a holomorphic function. For theories where ϕ takes value from $\mathbb{R}^N$, manifolds need to be in the "asymptotically safe region", which $\mathbb{R}^N$ also belongs to, at infinities $|\phi| \to \infty$. An asymptotically safe region is where the integrand $e^{-S(\phi)}$ vanishes at $|\phi| \to \infty$ such that the integration in this region does not contribute to the path integral. For example, the action $S(\phi) = -\phi^4$ has two disconnected asmptotically safe regions separated by borders $\arg\phi = (1+2n)\pi/8$ (for integer n) as are sketched in Figure 3.2. Only contours in the safe region which includes the real axis are allowed.

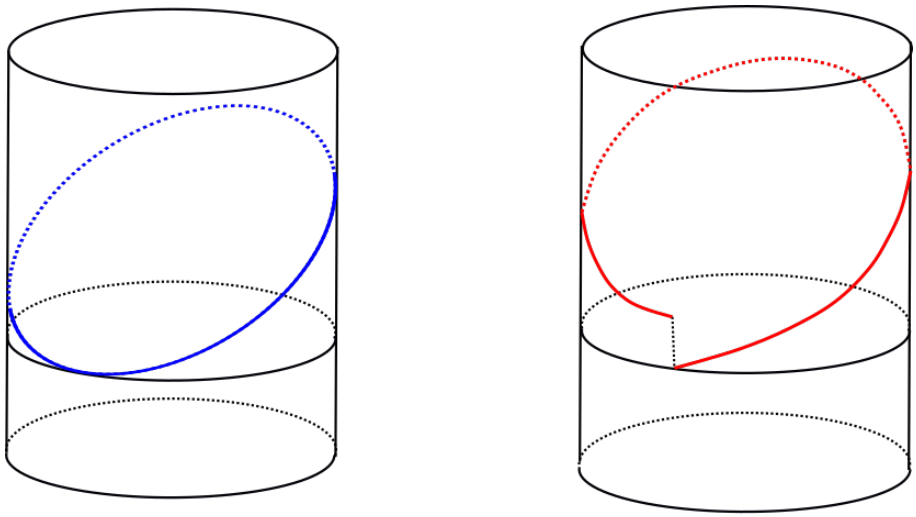

Figure 3.1: Contour deformation on a cylinder. The blue contour on the left gives the correct expectation values while the red contour with the gap does not.

When these conditions are met, Cauchy's theorem guarantees that the integrals of $e^{-S(\vec{\phi})}$ and $\mathcal{O}(\phi)e^{-S(\phi)}$ on the union of the original domain of integration and $\mathcal{M}$ both vanish so that

$$\int_{\mathcal{M}} \mathcal{D}[\phi]\ e^{-S(\phi)} = \int_{\mathbb{R}^N} \mathcal{D}[\phi]\ e^{-S(\phi)}\ , \tag{3.6}$$

and the same holds for the integral of $\mathcal{O}(\phi)e^{-S(\phi)}$.

As is introduced at the beginning of the section, manifold deformation methods have been applied to a variety of sign problems and alleviated them. However, it is fair to summarize that no sign problem in QCD has been *solved* so far by manifold deformation methods or any other methods. In other words, no manifold deformation methods have successfully found a manifold of integration with the average sign of 1 in a scalable way in the presence of sign problems in QCD. To solve a sign problem, the existence or non-existence of a *perfect manifold*, which has the average sign of 1, for a given lattice field theory is a crucial question to be addressed before a manifold deformation method is applied. The existence of perfect manifolds will be discussed in

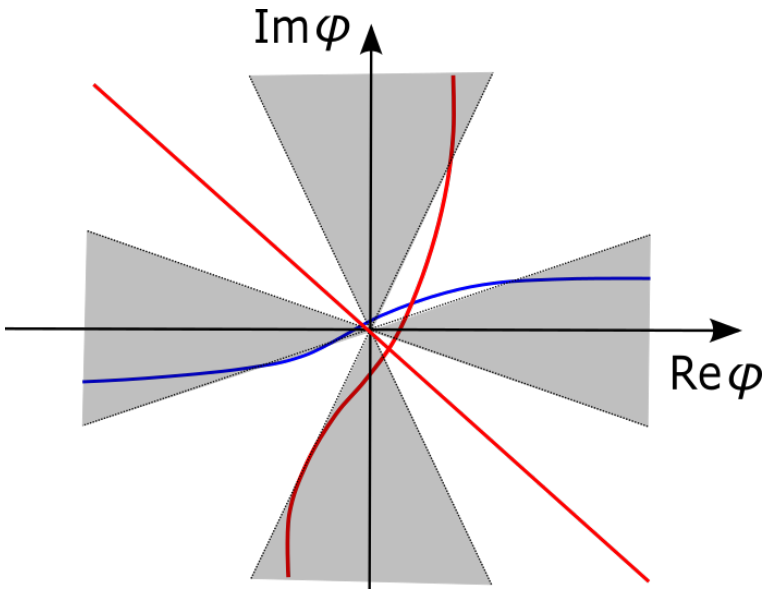

Figure 3.2: Contour deformation on the complex plane of ϕ. Gray shaded regions are the aymptotically safe regions when the Boltzmann factor is $e^{-\phi^4}$. The blue contour gives the correct expectation values while the red contours do not.

Sec.3.4.1.

3.3 Complex normalizing flows

In this section, I discuss another potential method for solving sign problems — the complex normalizing flow [17, 115]. While the complex normalizing flow is conceptually equivalent to the manifold deformation method introduced in the last section, it provides several important mathematical and algorithmic consequences. The idea of the manifold deformation was to deform the contour of integration so that the average sign increases. When one wants to completely solve a sign problem, the ultimate goal is to find a *perfect manifold* which has the average sign $\langle\sigma\rangle = 1$. The existence of such perfect manifolds is a very non-trivial but essential question to be addressed for each lattice theory before a manifold deformation method is applied. Complex normalizing flows give us a tool to address this question as will be discussed in Sec. 3.4.2.

Complex normalizing flows also provide a way for us to find such perfect manifolds with the aid of machine learning in a similar way as discussed in [140]. In addition to that, once a complex normalizing flow is found, it accelerates Monte Carlo samplings for evaluating the path integral, as will be discussed in this section and Sec. 3.5. In this section, I introduce the idea of complex normalizing flows for reducing sign problems, starting by introducing the definition of normalizing flows.

A normalizing flow for N dimensional probability distribution $f(\phi) : \mathbb{R}^N \to \mathbb{R}$ (normalized to be 1) is a map from $f(\phi)$ to a trivial distribution such as the Gaussian distribution:

$$\det\left(\frac{\partial\phi}{\partial x}\right) f(\phi) = g_N(\vec{x}) \ . \tag{3.7}$$

Here function $g_n(\vec{x})$ is the n-dimensional Gaussian distribution:

$$g_n(\vec{x}) = \prod_{i=1}^{n} \frac{1}{\sqrt{2\pi}} \exp(-x_i^2/2). \tag{3.8}$$

Such a normalizing flow exists for any normalizable distribution functions in any dimensions [145]. For 1-dimensional distributions $f(\phi) : \mathbb{R} \to \mathbb{R}$, their normalizing flows defined via

$$\frac{\mathrm{d}\phi}{\mathrm{d}x} f(\phi) = g_1(x) \tag{3.9}$$

can be uniquely constructed via the cumulative distribution functions of $f(\phi)$ and $g_1(x)$

$$F(\phi) = \int_{-\infty}^{\phi} d\phi' \ f(\phi'), \quad G(x) = \int_{-\infty}^{x} dx' \ g_1(x). \tag{3.10}$$

The cumulative distribution functions are the normalizing flows from f, g_1 to a uniform distribution on the interval $[0, 1]$. Thus the map from $g_1(x)$ to $f(\phi)$ can be constructed a sequence of two maps as

$$\phi(x) = F^{-1} \circ G. \tag{3.11}$$

Normalizing flows for multi-dimensional distributions ($N > 1$) are known to exist [145] but they ceases to be unique, making it more challenging to find such maps. Finding normalizing flows with desirable features is an active area of research [145].

The application of normalizing flows to lattice field theories without sign problems has been studied intensely in recent years [146, 147, 148, 149, 150]. The advantage of the use of normalizing flows is that Markov chain Monte Carlo (MCMC) methods can be accelerated by generating an approximate normalizing flow $\phi(x)$ for the Boltzmann factor and applying it to the path integral:

$$\langle \mathcal{O} \rangle = \frac{\int \mathcal{D}\phi \; e^{-S(\phi)} \; \mathcal{O}(\phi)}{\int \mathcal{D}\phi \; e^{-S(\phi)}} = \frac{\int d\vec{x} \; g_N(\vec{x}) \; \mathcal{O}(\phi(\vec{x}))}{\int d\vec{x} \; g_N(\vec{x})} \; . \tag{3.12}$$

Here, sampling of N real variables $\vec{x}$ from the Gaussian distribution can be done more efficiently than performing MCMC samplings of ϕ from the original distribution $e^{-S(\phi)}$. Such normalizing flows can also be used to create proposals for the lattice field configurations for a Markov chain.

In practice, searches for normalizing flows are often numerical and one obtains a map that only approximates an exact normalizing flow. Such an approximate map induces an effective action on ϕ

$$S_{\text{ind}}(\phi) = x(\phi)^2 + \log \det \frac{\partial \phi}{\partial x}. \tag{3.13}$$

Thus to compute correct expectation values with such an approximate normalizing flow, the

following ratio must be computed:

$$\langle \mathcal{O} \rangle = \frac{\langle e^{S_{\rm ind}-S} \mathcal{O} \rangle}{\langle e^{S_{\rm ind}-S} \rangle} \tag{3.14}$$

where the expectation values in the numerator and the denominator are evaluated with the induced distribution $e^{-S_{\rm ind}}$ using the approximate normalizing flow.

Normalizing flows cannot be applied to lattice field theories with a sign problem directly. For a Boltzmann factor e^{-S} which takes complex values to be mapped to the Gaussian distribution as in Eq. (3.7), we must allow the mapped ϕ to be complex-valued. Thus the normalizing flow is now a map $\phi(x) : \mathbb{R}^N \to \mathbb{C}^N$ from the real variables in the Gaussian distribution x in $\mathbb{R}^N$ to the complexified physical fields ϕ in $\mathbb{C}^N$. We call such maps the *complex normalizing flows*. If such a complex normalizing flow is found for a lattice field theory of one's interest, the map can be used in the same way as traditional normalizing flows. Instead of sampling from the Boltzmann factor (or the quenched Boltzmann factor as we assumed the presence of a sign problem), one can sample from the Gaussian distribution and apply the complex normalizing flow as in Eq. (3.12) to compute expectation values. There are some conditions to be met for complex normalizing flows as will be discussed shortly. The search for such maps is likely to be done numerically, and thus one obtains only an approximate complex normalizing flow. In such a situation, an appropriate reweighting should be performed as in Eq. (3.14).

The ideas of complex normalizing flows and manifold deformations are very tightly connected. A complex normalizing flow $\phi(x)$, starting from $\mathbb{R}^N$, maps each point $x \in \mathbb{R}^N$ to a point in the complex space $\mathbb{C}^N$ and thus generates a manifold $\mathcal{M}_n$ in $\mathbb{C}^N$. In other words, a complex normalizing flow provides a parametrization of the manifold $\mathcal{M}_n$ by $\mathbb{R}^N$. When one uses a

normalizing flow to compute expectation values, they are actually evaluated on such a generated manifold $\mathcal{M}_n$ in the complex plane of physical fields ϕ:

$$\langle \mathcal{O} \rangle = \frac{\int d\vec{x}\; g_N(\vec{x})\; \mathcal{O}(\phi(x))}{\int d\vec{x}\; g_N(\vec{x})} = \frac{\int_{\mathcal{M}_n} \mathcal{D}\phi\; e^{-S(\phi)}\; \mathcal{O}(\phi)}{\int_{\mathcal{M}_n} \mathcal{D}\; \phi e^{-S(\phi)}}\;. \tag{3.15}$$

To guarantee that such complex normalizing flows give the correct expectation values (the expectation values that are evaluated on the real plane $\mathbb{R}^N$), the complex normalizing flow $\phi(\vec{x})$ needs to be constructed such that the resulting manifold $\mathcal{M}_n$ satisfies the three conditions discussed in Sec. 3.2.

Given the connection between complex normalizing flows and deformed manifolds, it is clear that a manifold $\mathcal{M}_n$ generated by an exact complex normalizing flow has the average sign of 1 and thus has no sign problem. Therefore, for a complex normalizing flow to exist, a perfect manifold must exist. The converse holds as well — when a perfect manifold exists, that implies that a complex normalizing flow exists. This can be shown by the existence of normalizing flow for any real and positive-valued distributions. On a perfect manifold patameterized by N real parameters denoted as $\vec{y}$, the distribution $e^{-S(\phi(\vec{y}))}$ is real and positive in terms of $\vec{y}$. As there are always normalizing flows $\vec{y}(\vec{x})$ between the Boltzmann factor $e^{-S(\phi(y))}$ and the Gaussian distribution $g_N(\vec{x})$, the complex normalizing flow is constructed as

$$\phi(x) = \phi \circ y(x). \tag{3.16}$$

Thus the existence of perfect manifolds and complex normalizing flows are the equivalent statements. In the next section, we discuss the existence of perfect manifolds in Sec. 3.4.1 and complex

normalizing flows in Sec. 3.4.2. The possibility of the breakdown of such arguments for the existence of complex normalizing flows, and equivalently perfect manifolds, are also discussed based on our current understanding [17, 115]. In Sec. 3.4.3, the existence and non-existence of perfect manifolds are demonstrated with 1-dimensional toy models.

3.4 Existence

In this section, the existence of *locally perfect* manifolds is discussed. On a locally perfect manifold, the Boltzmann factor locally has a fixed phase but the manifold consists of segments which have different phases. Therefore, such a manifold is locally perfect but still has a *global sign problem*. In Sec. 3.4.1, I show how one can construct such a locally perfect manifold in the context of manifold deformation methods. In Sec. 3.4.2, I discuss the existence of locally perfect manifolds using normalizing flows.

3.4.1 Existence of perfect manifolds

In this section, we show how a locally perfect manifold can be constructed. The key tool used here is the holomorphic gradient flow [131]:

$$\frac{\mathrm{d}\phi}{\mathrm{d}t} = \overline{\frac{\partial S}{\partial \phi}}. \tag{3.17}$$

It is a first order differential equation to update each point ϕ in the manifold of integration and thus let the manifold of integration "flow". Here t is the flow time of the manifold, which has nothing to do with the time as in Minkowski spacetime. At each flow time t, we obtain a new manifold. At $t \to \infty$, the manifold flows into Lefschetz thimbles [127, 128, 129, 130]. The idea

of the generalized thimble method [131] is to flow the manifold only for a finite flow time. As one updates the manifold over flow time t, the real part of the action S keeps increasing

$$\frac{\mathrm{d}S}{\mathrm{d}t} = \left|\frac{\partial S}{\partial \phi}\right|^2 . \tag{3.18}$$

Therefore the quenched partition function decreases, and one may expect that the average sign will increase. In fact, at the infinite limit of the flow time, the imaginary part of the action stays constant on the manifold as it is the case for Lefschetz thimbles. Unfortunately, the average sign is still not guaranteed to increase. Thimbles are likely to have a sign problem due to the Jacobian at larger flow time and thus are not optimal manifold of integration. Nevertheless, the holomorphic gradient flow can still be used to construct a locally perfect manifold. The key feature of the holomorphic gradient flow is that when a manifold starts to flow from the real plane $\mathbb{R}^N$, for an infinitesimal flow time t, the holomorphic gradient flow always improves the sign problem, as is shown in the following.

To begin, let us note that the numerator of the average sign, the partition function Z, does not change due to the holomorphic gradient flow as long as the three conditions discussed in Sec. 3.2 are met on the resulting manifold of integration. On the other hand the denominator, the quenched partition function Z_Q should change as the integrand $e^{-\operatorname{Re} S}$ not a holomorphic function. Thus, when the sign problem improves, we expect to see that Z_Q decreases while Z remains the same. Let us demonstrate that Z_Q always decreases at early flow time. The change in the quenched partition function at the start, $\mathbb{R}^N$, is given by

$$\frac{\mathrm{d}}{\mathrm{d}t} Z_Q = \frac{\mathrm{d}}{\mathrm{d}t} \int_{\mathbb{R}^N} \mathcal{D}\phi \; e^{-\operatorname{Re} S[\tilde{\phi}(\phi)]} \left|\det \frac{\partial \tilde{\phi}}{\partial \phi}\right| , \tag{3.19}$$

where each point $\phi \in \mathbb{R}^N$ is flowed to a point $\tilde{\phi}(\phi) \in \mathbb{C}^N$. The parameterization, $\tilde{\phi}(\phi)$ with $\phi \in \mathbb{R}^N$, of the new manifold was used to write Eq. (3.19), so the manifold of integration remains to be $\mathbb{R}^N$. Thus we can focus sorely on the change in its integrand. The derivative of the integrand with respect to t is

$$\frac{\mathrm{d}}{\mathrm{d}t} e^{-\operatorname{Re} S} |\det J| = e^{-\operatorname{Re} S} |\det J| \left[\operatorname{Re} \operatorname{Tr} J^{-1} \frac{\mathrm{d}J}{\mathrm{d}t} - \frac{\mathrm{d} \operatorname{Re} S}{\mathrm{d}t} \right]. \tag{3.20}$$

As is seen in Eq. (3.18), the change in the real part of the action is guaranteed to be non-negative: $\frac{\mathrm{d} \operatorname{Re} S}{\mathrm{d}t} = \left| \frac{\mathrm{d}S}{\mathrm{d}\tilde{\phi}} \right|^2$. Thus when the term with the Jacobian is smaller than the second term, the quenched partition function Z_Q decreases and the sign problem is improved. This scenario is not guaranteed to happen at ant flow time t. Indeed, at larger flow time t, the Jacobian tends to be large and Z_Q increases, worsening the sign problem. However, starting from the real plane, at least at early flow time, it is guaranteed that the term is Jacobian is small enough for the quenched partition function to decrease. The Jacobian at the real plane is diagonal with $\frac{\mathrm{d}\tilde{\phi}_i}{\mathrm{d}\phi_i}$ for each diagonal element, and therefore we find that

$$\operatorname{Tr} J^{-1} \frac{\mathrm{d}J}{\mathrm{d}t} = \sum_i \overline{\frac{\partial^2 S}{\partial \tilde{\phi}_i^2}}. \tag{3.21}$$

As we evaluate Jacobian term on the real plane, its real part is simply $\sum_i \frac{\partial^2 \operatorname{Re} S}{\partial \phi_i^2}$. Thus Eq. (3.20) is simplified and becomes

$$\frac{\mathrm{d}}{\mathrm{d}t} e^{-\operatorname{Re} S} |\det J| = \sum_i e^{-\operatorname{Re} S} \left[\frac{\partial^2 \operatorname{Re} S}{\partial \phi_i^2} - \left| \frac{\partial S}{\partial \tilde{\phi}_i} \right|^2 \right]. \tag{3.22}$$

To further simplify Eq. (3.19), the following relation for the magnitude of the derivative of the

action on the real plane is useful:

$$\left|\frac{\partial S}{\partial \tilde{\phi}_i}\right|^2 = \left(\frac{\partial \operatorname{Re} S}{\partial \phi_i}\right)^2 + \left(\frac{\partial \operatorname{Im} S}{\partial \phi_i}\right)^2 . \tag{3.23}$$

The first term can be written with a total derivative

$$\frac{\partial}{\partial \phi_i}\left(\frac{\partial \operatorname{Re} S}{\partial \phi_i} e^{-\operatorname{Re} S}\right) = e^{-\operatorname{Re} S}\left[\frac{\partial^2 \operatorname{Re} S}{\partial \phi_i^2} - \left(\frac{\partial \operatorname{Re} S}{\partial \phi_i}\right)^2\right]. \tag{3.24}$$

Using these relations, Eq. (3.19) becomes

$$\begin{aligned}
\frac{\mathrm{d}Z_Q}{\mathrm{d}t} &= \int \mathcal{D}\phi \sum_i \left[\frac{\partial}{\partial \phi_i}\left(\frac{\partial \operatorname{Re} S}{\partial \phi_i} e^{-\operatorname{Re} S}\right) + e^{-\operatorname{Re} S}\left(\frac{\partial \operatorname{Re} S}{\partial \phi_i}\right)^2 \right. \\
&\qquad \left. - e^{-\operatorname{Re} S}\left(\frac{\partial \operatorname{Re} S}{\partial \phi_i}\right)^2 - e^{-\operatorname{Re} S}\left(\frac{\partial \operatorname{Im} S}{\partial \phi_i}\right)\right] \\
&= -\int \mathcal{D}\phi\, e^{-\operatorname{Re} S}\left(\frac{\partial \operatorname{Im} S}{\partial \phi_i}\right)^2 .
\end{aligned} \tag{3.25}$$

The final expression above is clearly non-positive, and strictly negative when the imaginary part of the action changes while $e^{-\operatorname{Re} S}$ is non-vanishing. Thus we conclude that the quenched partition function Z_Q always decreases after an infinitesimal flow from the real plane in the presence of a sign problem.

This is the key result of the holomorphic gradient flow from the real plane $\mathbb{R}^N$: when a sign problem exists on the real plane, an infinitesimal deformation of the manifold $\mathbb{R}^N$ by the holomorphic gradient flow Eq. (3.17) is guaranteed to improve the sign problem by making the quenched partition smaller. At a larger flow time, this not true any more — the quenched partition function can increase and worsen the sign problem due to the Jacobian. Another problem with

the use of the holomorphic gradient flow for a large flow time is that the resulting manifold may be a union of several thimbles which may have different phases and thus introduces a cancellation between different thimbles. Local phase fluctuations due to the Jacobian are sometime referred to as a *local sign problem* while cancellations between thimbles are called a *global sign problem*. In the following, we show how one can in principle get rid of the local sign problem by applying infinitesimal holomorphic gradient flows from the real plane. As will be discussed later, a resulting locally perfect manifold may still have a global sign problem due to the cancellation between segments of the manifold.

I start the construction of a locally perfect manifold by flowing the original manifold $\mathbb{R}^N$ by the holomorphic gradient flow Eq. (3.17) until an infinitesimal flow time $t = \epsilon$. All points $\phi \in \mathbb{R}^N$ will be mapped to $\phi_1 \in \mathbb{C}^N$ according to the gradient flow (up to the linear order in ϵ)

$$\phi_1(\phi) = \phi + \epsilon \left.\overline{\frac{\partial S}{\partial \phi}}\right|_{\phi}. \tag{3.26}$$

and form a new manifold $\mathcal{M}_1$. As an infinitesimal flow from the real plane makes the quenched partition function smaller, the sign problem is improved on $\mathcal{M}_1$ compared to $\mathbb{R}^N$.

To improve the manifold further, I would like to parameterize $\mathcal{M}_1$ by $\mathbb{R}^N$ and flow the manifold again with an effective action induced by the parameterization. One such parameterization of the new manifold $\mathcal{M}_1$ is the map $\phi_1(\phi)$, which induces an effective action

$$S_1(\phi) = S[\phi_1(\phi)] - \log\det\left(1 + \epsilon \frac{\partial}{\partial \phi} \left.\overline{\frac{\partial S}{\partial \phi}}\right|_{\phi}\right). \tag{3.27}$$

This is an action defined on $\mathbb{R}^N$. We would like to apply the holomorphic gradient flow with this

new action S_1 and improve the sign problem again. However, there is a technical complication which is that the effective action S_1 is no longer a holomorphic function of ϕ, most explicitly due to the anti-holomorphic term $\overline{\frac{\partial S}{\partial \phi}}\Big|_{\phi}$.

A way to circumvent the problem is to realize that the manifold flows from the real plane, so that the flow equation Eq. (3.26) could be equivalently defined as

$$\phi_1(\phi) = \phi + \epsilon \, \overline{\frac{\partial S}{\partial \phi}}\Big|_{\bar{\phi}} . \tag{3.28}$$

The last term means that one evaluates the complex conjugate of $\frac{\partial S}{\partial \phi}$ at the complex conjugate $\bar{\phi}$. This map defines exactly the same manifold as $\mathcal{M}_1$ as $\phi = \bar{\phi}$ on $\mathbb{R}^N$, but at the same time offers a holomorphic map in the complex plane. Thus using this map, we modify the induced action as

$$S_1(\phi) = S[\phi_1(\phi)] - \log\det\left(1 + \epsilon \frac{\partial}{\partial \phi} \, \overline{\frac{\partial S}{\partial \phi}}\Big|_{\bar{\phi}}\right), \tag{3.29}$$

which is holomorphic.

Given the effective action S_1 as a holomorphic function in the complex plane of ϕ, we apply the holomorphic gradient flow again by a small flow time ϵ

$$\phi_2(\phi) = \phi + \epsilon \, \overline{\frac{\partial S_1}{\partial \phi}}\Big|_{\bar{\phi}} . \tag{3.30}$$

The map from the real plane to the resulting new manifold $\mathcal{M}_2$ is given by composing two flows, ϕ_1 and ϕ_2, as $\phi_2(\phi)$. The quenched partition function on $\mathcal{M}_2$ is guaranteed to be strictly smaller than that of $\mathcal{M}_1$ (unless the manifold $\mathcal{M}_1$ had no local sign problems) and thus the sign problem is improved.

The parameterization of manifolds $\mathcal{M}_i$ at each flow step is not unique. Let us denote a parameterization of manifold $\mathcal{M}_i$ as $p_i : \mathbb{C}^N \to \mathbb{R}^N$, and each flow map as $\phi_i : \mathbb{R}^N \to \mathbb{C}^N$. (In the demonstration above, p_1 was taken to be the inverse of ϕ_1.) Then the manifold will be improved as

$$\begin{aligned} \mathcal{M}_1 &= \{\phi_1(\phi), \phi \in \mathbb{R}^N\} \\ \mathcal{M}_i &= \{\phi_i(p_{i-1}(\tilde{\phi})), \tilde{\phi} \in \mathcal{M}_{i-1}\} \end{aligned} \tag{3.31}$$

One can repeat the process of parameterization of manifolds by p_i and flow ϕ_i via Eq. (3.17) using the effective actions to keep improving the manifold of integration while reducing the sign problem.

As we repeat the small flow, the quenched partition function Z_Q keeps decreasing. There are two possible end results after a large number of flows. One possibility is that a manifold reaches a "fixed point" where the manifold will not be moved by the holomorphic gradient flow any more. The other possibility is that some singular behavior of the manifold is introduced and the parameterization via the real plane $\mathbb{R}^N$ becomes no longer possible. There is no formal proof that such singular behavior does not occur. Examples where such behavior of the manifold is observed are currently investigated.

The first scenario where small flows let the manifold of integration reach a fixed point $\mathcal{M}_f$ is when we find a locally perfect manifold. When denoting the final effective action as S_f, at the fixed point, the flow equation Eq. (3.26) does change the manifold, meaning that the flow vectors $\overline{\frac{\partial S_f}{\partial \phi}}$ lie entirely in the real plane and thus the imaginary part of S_f does not vary with ϕ.

Equivalently, in Eq. (3.25), the quenched partition function does not change, meaning that

$$e^{-\operatorname{Re} S}\left(\frac{\operatorname{Im} S}{\partial\phi_i}\right)^2 = 0 \tag{3.32}$$

for all i. Therefore, unless the quenched Boltzmann factor $e^{-\operatorname{Re} S}$ vanishes, the phase of the Boltzmann factor $e^{-i\operatorname{Im} S}$ is guaranteed to be constant. Thus the manifold $\mathcal{M}_f$ may be separated to segments by the "zeros" of the Boltzmann factor, but each segment is guaranteed to have a fixed phase. Nevertheless, segments may possess different phases and a cancellation may occur between segments. We call such manifolds as locally perfect, but not globally perfect manifolds — $\mathcal{M}_f$ may possess a global sign problem. Such a vanishing Boltzmann factor is not a uncommon scenario. For example, the Boltzmann factor of QCD in the Schwinger-Keldysh formalism at zero and finite chemical potential has zeros in the complex plane. To obtain globally perfect manifolds for QCD, such zeros need to be avoided while drawing the manifold of integration. There is no formal proof which guarantees the availability of such construction of manifolds without zeros. On the other hand, the Boltzmann factor of bosonic lattice field theories in the Schwinger-Keldysh formalism in general does not vanish except at infinities — their actions consist only of the polynomials of bosonic fields. Thus, it is likely that globally perfect manifolds exist for bosonic lattice field theories, such as the ϕ^4 scalar field theory and $SU(N)$ gauge theories.

A similarity and a difference between the fixed-point manifold $\mathcal{M}_f$ and the Lefschetz thimbles should be emphasized. When a fixed point manifold is parameterized by the real plane, the resulting effective action has no phase fluctuation in each segments separated by the zeros of the Boltzmann factor. Similarly, when a Lefschetz thimble is parameterized by the real plane, it

consists of several segments separated by the points with vanishing Boltzmann factor and may introduce a global sign problem. The key difference between two kinds of manifolds is that, on a Lefschetz thimbles, each segment has constant phase from the physical action but still possesses a phase fluctuation in the effective action on the real plane due to the Jacobian. Thus the Lefschetz thimbles can possess both local and global sign problems, in contrast to the fixed point manifold having only global sign problems. The presence of a global sign problem in a Lefschetz thimble does not guarantee the presence of a global sign problem on a fixed-point manifold as was shown in an example in [17].

3.4.2 Existence of complex normalizing flows

Normalizing flows give an alternative framework to construct perfect manifolds, based on the fact that complex normalizing flows always generate perfect manifolds. To illustrate the construction of perfect manifolds via complex normalizing flows, let us consider a family of actions $S(\phi;\lambda)$ which are smoothly connected by the parameter λ. In this family of actions, we include an action $S(\phi;\lambda_0)$ which has no sign problems and $S(\phi;\lambda_t)$ which possesses a sign problem. Our goal is to construct a perfect manifold, or equivalently a complex normalizing flow for the action $S(\phi;\lambda_t)$.

Normalizing flows exist for the action $S(\phi;\lambda_0)$, which we denote as $\phi = f_0(x;\lambda_0)$. To further proceed and construct a complex normalizing flow for $S(\phi;\lambda_t)$, the key point of view is to think of the action $S(\phi;\lambda_0)$ as the function of the parameter λ_0, and so as the normalizing flow, defined by

$$\det\left(\frac{\partial f_0(x;\lambda_0)}{\partial x}\right) e^{-S(f_0(x;\lambda_0))} = \mathcal{N} g_N(\vec{x}). \tag{3.33}$$

Here the normalization of the Boltzmann factor was introduced as $\mathcal{N}$. When the normalizing flow $\phi = f_0(x; \lambda_0)$ is an analytic function of λ_0, then one can simply perform analytic continuation of the normalizing flow $f_0(x; \lambda_0)$ in the parameter space of λ towards λ_t to obtain a normalizing flow for $S(\phi; \lambda_t)$, which I denote as $\phi = f_t(x; \lambda_t)$. Now we use the map $f(x; \lambda_t)$ to generate a perfect manifold by mapping all points $x \in \mathbb{R}^N$ to $\phi \in \mathbb{C}^N$.

The analyticity of normalizing flows as a function of action's parameters for sign-free actions is not generically proven. To show one example where the normalizing flow is an analytic function of action's parameters, we take real scalar field theory with ϕ^4 interaction

$$S = \sum_{ij} \phi_i M_{ij} \phi_j + \lambda \sum_i \Lambda_i \phi_i^4. \tag{3.34}$$

Here i, j denote lattice sites. The matrix M represents the mass terms and kinetic terms together, λ is the coupling strength. Here we leave the expression for the action generic so that with one's choice of M and Λ, the action represents real scalar field theory with arbitrary Schwinger-Keldysh contours. In the following, we derive normalizing flows analytically up to the first order in weak-coupling and then strong-coupling expansion while leaving M, Λ in such generic forms.

To start, for a general action S_0 with a perturbing term $\mathcal{O}$

$$S = S_0 + g\mathcal{O} \tag{3.35}$$

let us consider a map $\tilde{\phi}(\phi)$ from $e^{-S(\tilde{\phi})}$ to $e^{-S_0(\phi)}$:

$$\det\left(\frac{\partial \tilde{\phi}}{\partial \phi}\right) e^{-S(\tilde{\phi}(\phi))} = \mathcal{N} e^{-S_0(\phi)} \tag{3.36}$$

The map is $\tilde{\phi}(\phi) = \phi$ when $g = 0$. For small g, we expand the map $\tilde{\phi}(\phi)$ as a power series in g as $\tilde{\phi}(\phi) = \phi + g\Delta^{(1)}(\phi) + \cdots$. By expanding Eq. (3.36) up to the first order in g, we obtain the following differential equation for $\Delta^{(1)}(\phi)$

$$\nabla \cdot \Delta^{(1)} - \Delta^{(1)} \cdot \nabla S_0 = \mathcal{O} - \langle \mathcal{O} \rangle. \tag{3.37}$$

Here the expectation value $\langle \mathcal{O} \rangle$ is evaluated with the distribution e^{-S_0}. The perturbed map $\Delta^{(1)}$ can be derived by solving Eq. (3.37), although the solution is in general not unique.

In the weak coupling limit of the action Eq. (3.34), the map $\tilde{\phi}(\phi)$ defined in Eq. (3.36) is well-approximated by a perturbative flow $\tilde{\phi}(\phi) = \phi + \lambda\Delta^{w,(1)}(\phi)$ where $\Delta^{w,(1)}$ satisfies Eq. (3.37) with $\mathcal{O} = \sum_i \Lambda_i \phi_i^4$. One of the simplest solutions is

$$\Delta_i^{w,(1)} = -\sum_j \left[\frac{1}{2} M_{ij}^{-1} \Lambda_j \phi_j^3 + \frac{3}{4} M_{ij}^{-1} M_{jj}^{-1} \Lambda_j \phi_j \right]. \tag{3.38}$$

To construct a perturbative normalizing flow with $\Delta^{w,(1)}$, we additionally need a map $\phi(x)$ from $e^{-S_0(\phi)}$ to the Gaussian distribution $g(x)$. Since the free action S_0 is already quadratic, such a map is simply a linear rotation $\phi(x) = Ux$. The entire pertirbative map from $e^{-S}(\tilde{\phi})$ to the Gaussian distribution is

$$\tilde{\phi}(x) = \phi(Ux) + \Delta^{w,(1)}(\phi(Ux)). \tag{3.39}$$

The map U and $\Delta^{w,(1)}$ are both analytic functions of M and Λ except when $\det M$ vanishes. Therefore, in principle one can perform analytic continuation of the perturbative normalizing flow at weak couplings from a sign-free action to Schwinger-Keldysh actions with a real-time extent. However, such normalizing flows will not provide an induced manifold with a desired

asymptotic behavior.

In the derivation of the normalizing flow above, I obtained the expression for perturbative normalizing flows for arbitrary Schwinger-keldysh contours determined by M, Λ. One may think of directly using the perturbative flow as a good approximation to the normalizing flows for the Schwinger-Keldysh scalar action at weak coupling. It is unlikely that this will work — a manifold generated by the perturbavative flow does not have the correct asymptotic behavior. For manifolds to be in the asymptotically-safe region, we must study the behavior of normalizing flows at large ϕ, or in other words, the strong coupling limit of λ.

To obtain a perturbative flow at a strong coupling, I first decompose the map $\phi^s(x)$ into four pieces:

$$\phi^s(x) = \left[F_4 \circ F_3 \circ F_2 \circ F_1\right](x). \tag{3.40}$$

The first map $F_1 : \mathbb{R} \to \mathbb{R}$ maps the distribution e^{-x^2} to $e^{-\phi^4}$ at each site i. Following the prescription in Eq. (3.11), the map can be written by the sequence of two cumulative distribution functions Π and P as

$$\begin{aligned} F_1(x) &= \Pi^{-1} \circ P, \text{ with} && (3.41)\\ \Pi(x) &= \frac{1}{2} + \frac{1}{2}\left(1 - \frac{\Gamma\left[1/4, x^4\right]}{\Gamma(1/4)}\right) \text{sgn}x && (3.42)\\ P(x) &= \frac{1}{2}\left(1 + \text{Erf}(x/\sqrt{2})\right). && (3.43) \end{aligned}$$

The second map $F_2 : \mathbb{R} \to \mathbb{R}$ rotates and scales the complex plane to map the distribution $e^{-\phi^4}$ to $e^{-\Lambda\psi^4}$. The map is simply

$$F_2(\phi) = \phi/\Lambda_i^{1/4} \tag{3.44}$$

On most sites on a Schwinger-Keldysh contour, the map performs the rotation of a complex plane, except an additional scaling by a factor of $2^{1/8}$ at the corners of the Schwinger-Keldish contour.

The map $F_3 : \mathbb{R}^N \to \mathbb{R}^N$ maps the distribution $e^{-S_0(\phi)}$ with $S_0 = \sum_i \Lambda\phi_i^4$ to $e^{-S'(\psi)}$ with

$$S'(\psi) = \sum_i \Lambda_i \psi_i^4 + \frac{1}{\sqrt{\lambda}} \sum_{ij} \psi_i M_{ij} \psi_j \tag{3.45}$$

This is where we perform the strong coupling expansion and write the ith component of the map as $F_{3,i}(\phi) = \phi_i + \frac{1}{\sqrt{\lambda}}\Delta_i^{s,(1)}(\phi)$. The perturbative part $\Delta^{s,(1)}(\phi)$ satisfies Eq. (3.37) with $S_0 = \sum_i \Lambda\phi_i^4$ and $\mathcal{O} = \sum_{ij} \phi_i M_{ij} \phi_j$. Its expectation value $\langle\mathcal{O}\rangle$ must be evaluated with S_0. By introducing $f_i = \Delta_i^{s,(1)}(\phi) e^{-\Lambda_i\phi_i^4}$ and using the fact that $\langle\phi_i\phi_j\rangle$ vanishes when $i \neq j$, one can choose for the each map f_i to satisfy

$$\frac{\partial f_i}{\partial \phi_i} e^{\Lambda_i\phi_i^4} - \sum_j M_{ij}\phi_i\phi_j = -M_{ii}\langle\phi_i^2\rangle. \tag{3.46}$$

The expectation value is analytically computed to be $\langle\phi_i^2\rangle = \frac{\Gamma(3/4)}{4\Gamma(5/4)\sqrt{\Lambda_i}}$. The fact that only diagonal and nearest-neighbor elements in M are non-zero simplifies the differential equation further. The solution is

$$\begin{aligned}\Delta_i^{s,(1)}(\phi) &= e^{\Lambda_i\phi_i^4} M_{ii} \left[-\frac{\phi_i^3 \Gamma[\frac{3}{4}, \Lambda_i\phi_i^4]}{4(\Lambda_i\phi_i^4)^{3/4}} + \frac{\langle\phi_i^2\rangle\phi_i \Gamma[\frac{1}{4}, \Lambda_i\phi_i^4]}{4(\Lambda_i\phi_i^4)^{1/4}} \right] \\ &+ \sum_{j\in\{i-1,i+1\}} e^{\Lambda_i\phi_i^4} \frac{\sqrt{\pi}}{4\sqrt{\Lambda_i}} \left[\mathrm{Erf}(\sqrt{\Lambda_i}\phi_i^2) - C \right] M_{ij}\phi_j. \end{aligned} \tag{3.47}$$

Here, $(\cdot)^{1/4}$ refers to the principle fourth root and a specific choice of $C = 1$ gives a solution which is oscillation-free and vanishes at $\psi_i \to \infty$.

The final map, $F_4 : \mathbb{R} \to \mathbb{R}$, rescales the field by a factor of $\lambda^{1/4}$

$$F_4(\phi) = \phi/\lambda^{1/4}. \tag{3.48}$$

to obtain the distribution with the desired action S in Eq. (3.34).

Given analytic expressions for all maps in Eq. (3.40), let us examine if the perturbative normalizing flow ϕ^s is an analytic function of the parameters of the action M, Λ. Among four maps, only F_2 and F_3 depend on M, Λ. Both the map F_2 in Eq. (3.44) and F_3 in Eq. (3.47) are analytic functions of M and Λ except at vanishing Λ. Thus as long as we avoid $\Lambda = 0$, analytic continuation of the normalizing flow of the Euclidean real scalar fields (S with real-valued M and Λ in Eq. (3.34) gives the perturbtive normalizing flows for the action S for a Schwinger-Keldysh contour with a real-time extent.

Although the purpose of the exercise above was to show the analyticity of the perturbative normalizing flow for the lattice scalar field theory without a sign problem, a general expression for a perturbative normalizing flow of an arbitrary Schwinger-Keldysh contour in the strong coupling limit was derived in Eq. (3.40). The perturbative normalizing flow ϕ^s should approximate the full normalizing flow $\phi(x)$ defined as

$$\det\left(\frac{\partial\phi}{\partial x}\right) e^{-S(\phi)} = g_N(x) \tag{3.49}$$

in the strong coupling regime. Now, let us use this perturbative map and test its performance by measuring the average sign and real-time correlators on a $0+1$-dimensional lattice. To be more

precise, our action is

$$S_\phi = \sum_{t,x} \frac{(\phi_{x,t} - \phi_{x,t+1})^2}{2a_0(t)} + \sum_t \frac{a_0(t) + a_0(t-1)}{2} \left[\sum_{\langle xx' \rangle} \frac{(\phi_{x,t} - \phi_{x',t})^2}{2a_x^2} + \sum_x \left(\frac{m^2}{2} \phi_{x,t}^2 + \frac{\lambda}{4!} \phi_{x,t}^4 \right) \right]. \tag{3.50}$$

with the "S" contour in the Schwinger-Keldysh formalism, defined as

$$a_0(t) = \begin{cases} -i & t \in [0, N_t) \\ 1 & t \in [N_t, N_t + N_\beta/2) \\ i & t \in [N_t + N_\beta/2, 2N_t + N_\beta/2) \\ 1 & t \in [2N_t + N_\beta/2, 2N_t + N_\beta) \end{cases}. \tag{3.51}$$

Here N_t and N_β denote the number of time steps in real-time and imaginary-time respectively. In Figure 3.3, the average sign of the manifold generated from the perturbative map is plotted for a 12-sites ($N_\beta = 2, N_t = 5$) with $m = 0.5$ with varying coupling λ. As expected, the average sign is larger at strong couplings, meaning that manifolds of integration generated by the perturbative flow almost remove the sign problem for large coupling. However at sufficiently small couplings, the average sign is small, meaning that the perturbative flow cannot provide a sign-free manifold of integration. Note that as the perturbative normalizing flow is only approximately correct, the Boltzmann factor needed to be reweighted following Eq. (3.13) and Eq. (3.14).

To check the correctness of the normalizing flows, real-time correlators $\langle \phi(t)\phi(0) \rangle$ are evaluated with the flow while fixing $m = 0.5, \lambda/24 = 0.33$. The lattice has 14 sites with $N_\beta = 2$ and $N_t = 6$. The simulated results are compared with the exact Hamiltonian calculations shown in black dots to show a consistent agreement. The average sign was estimated to be $\langle \sigma \rangle =$

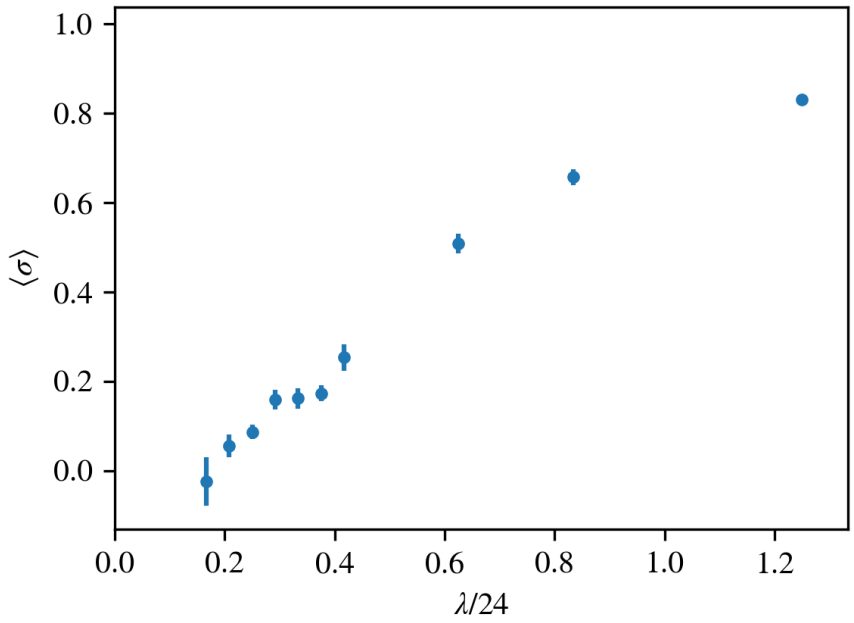

Figure 3.3: The average sign of the manifold generated from the perturbative map for a 12-sites ($N_\beta = 2, N_t = 5$) with $m = 0.5$ with varying coupling λ.

$0.096(5)$.

In this section, the construction of perfect manifolds by analytic continuation of normalizing flows was discussed. As a study case, perturbative normalizing flows for the ϕ^4 real scalar field theory were derived for the weak and strong coupling limits. It was shown that except for particular choices of the parameters of the action, the perturbative normalizing flows are analytic functions of action's parameters. As a byproduct, the perturbative flow in the strong coupling limit was used to approximate the normalizing flow for ϕ^4 scalar field theory, and the average sign and real-time correlators were evaluated on a $0 + 1$ dimensional lattice. The perturbative evaluation of normalizing flows up to higher orders does not seem to be practical, and thus would not be a solution to the real-time sign problem in ϕ^4 scalar field theory. The same will be true for other lattice field theories. Thus, in practice, another (potentially numerical) method will be required for searching complex normalizing flows, or equivalently perfect manifolds. The

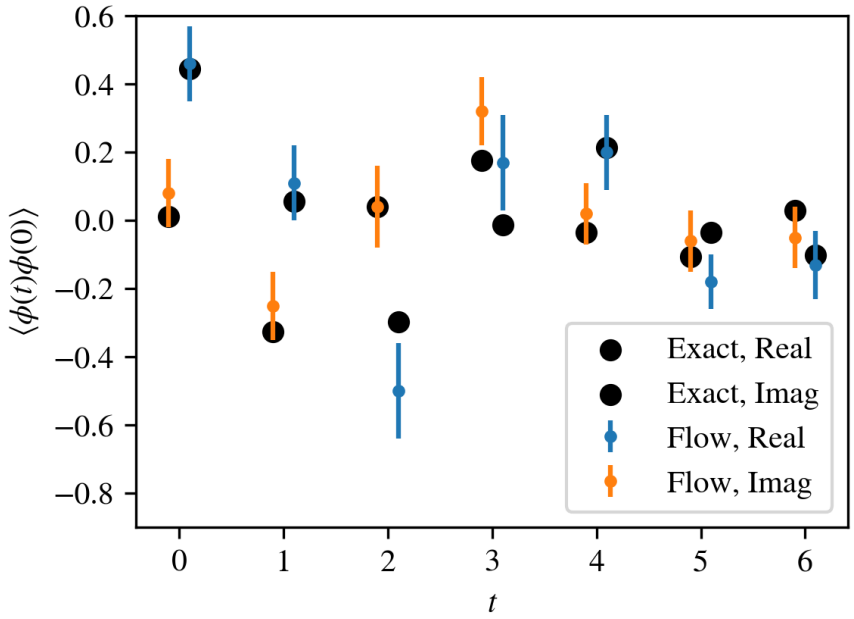

Figure 3.4: Real-time correlators $\langle\phi(t)\phi(0)\rangle$ evaluated with the perturbative normalizing flow while fixing $m = 0.5, \lambda/24 = 0.33$, $N_\beta = 2$ and $N_t = 6$.

application of tools from machine learning for searching normalizing flows will be explored in Sec. 3.5.

When a global sign problem cannot be removed, a normalizing flow does not exist either. One cause of such cases is, from the manifold deformation point of view, the zeros of the Boltzmann factor as was discussed in the last section. When a locally perfect manifold intersects with a point in the field space at which the Boltzmann factor vanishes, the manifold may possess a global sign problem due to the change of the phase across the zero. In such a case, we should also see the failure of the construction of a globally perfect manifold in the context of analytic continuation of normalizing flows. Going back to the definition of the normalizing flow,

$$\det\left(\frac{\partial\phi}{\partial x}\right) e^{-S(\phi)} = \mathcal{N} g_N(x) \tag{3.52}$$

we see that one of the followings has to happen at the singularities $\phi_0 = \phi(x_0)$ with $e^{-S(\phi_0)} = 0$:

1. The Jacobian diverges: $\det\left(\frac{\partial\phi}{\partial x}\right)_{\phi\to\phi_0} = \infty$ while x_0 stays finite.

2. The normalizing flow ϕ will send the point x_0 to infinity, $|x_0| \to \infty$ as the manifold approaches ϕ_0.

In Sec. 3.4.3, a toy model is introduced to demonstrate the first case and resulting failure of the construction of a normalizing flow.

3.4.3 Examples

The construction of perfect manifolds via analytic continuation of normalizing flows was discussed in the previous section. In this section, firstly a one-dimensional model was employed to demonstrate analytic continuation of normalizing flows and resulting construction of perfect manifolds. Then I will introduce another toy model which does not have globally perfect manifolds, and demonstrate how analytic continuation of normalizing flows fails to construct globally perfect manifolds.

3.4.3.1 Analytic continuation of normalizing flows

The first one-dimensional model is

$$e^{-S(y;a)} = \frac{1}{\sqrt{8\,(1+2\,a\,i)\,y+1-4\,i\,a-4a^2}}, \qquad 0<y<1 \tag{3.53}$$

where a can be any values in $\mathbb{C}$. We choose to let the denominator take the second principle root. When a takes any purely imaginary values, the Boltzmann factor does not cause sign problems

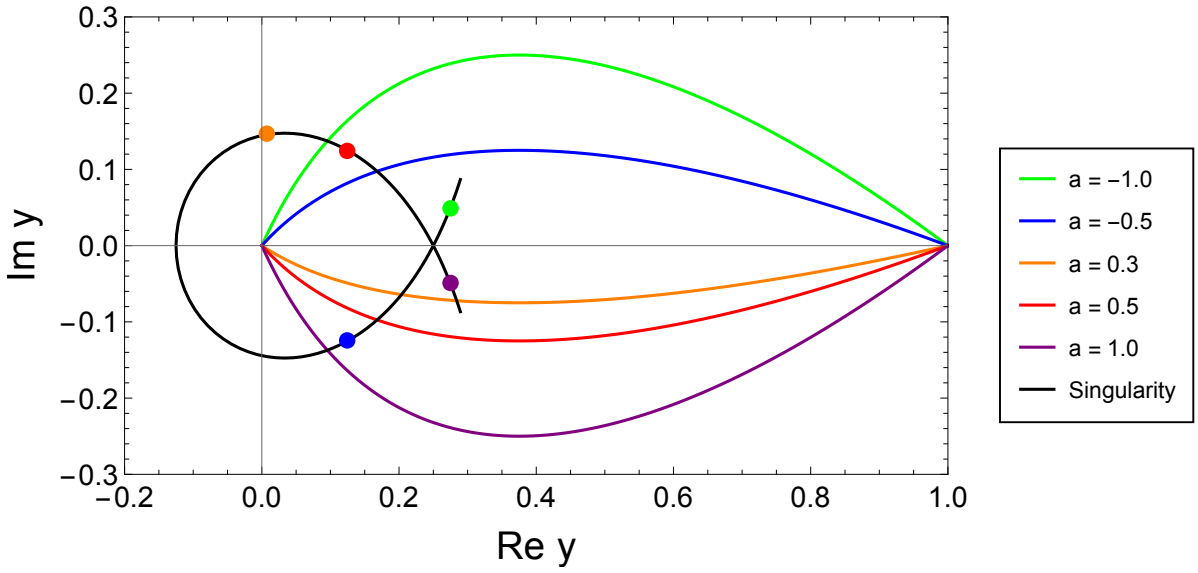

Figure 3.5: The manifold of integration drawn by the normalizing flow Eq. (3.55) with $a = -1.0, -0.5, 0.3, 0.5, 1.0$. Singularities for these values of a are in dots with the same color scheme. The black line shows the location of the singular point for $-1.1 < a < 1.1$.

and we have a normalizing flow. The normalizing flow $y(x)$ is the map from the Boltzmann factor above to the uniform distribution:

$$\frac{\mathrm{d}y(x;a)}{\mathrm{d}x}\frac{1}{\sqrt{8\,(1+2\,a\,i)\,y(x;a)+1-4\,i\,a-4a^2}}=1. \tag{3.54}$$

The normalizing flow can be simply written as

$$y(x;a)=\left(\frac{1}{2}+a\,i\right)x^2+\left(\frac{1}{2}-a\,i\right)x \tag{3.55}$$

When a takes a general complex value, a sign problem arises. As the Boltzmann factor is a holomorphic function of y in its complex plane except at one singularity $y=\frac{i(i+2a)^2}{8i-16}$, manifold deformation methods can be applied. When a perfect manifold is constructed while avoiding the singularity, the manifold should give correctly expectation values. The normalizing flow

Eq. (3.55) can be utilized to construct such perfect manifolds. Simply, we insert a complex-valued a to the normalizing flow equation while varying x in $[0, 1]$ to draw perfect manifolds, as is shown in Figure 3.4.3.1. In Figure 3.4.3.1, manifolds are drawn for $a = -1.0, -0.5, 0.3, 0.5, 1.0$. The Black line shows the location of the singularity of the Boltzmann factor while varying $-1.1 < a < 1.1$. For $a = -0.5, 0.3, 0.5$, singularities are outside the area closed by their manifolds and the real axis, and the manifolds give correct expectation values. However, for $a = -1.0, 1.0$, the singular points are inside the area closed by their manifolds and the real axis, and thus the manifolds give wrong answers. This issue comes from the original setting of the problem, which is that the principle root is taken for the square root in the Boltzmann factor.

3.4.3.2 Zeros of the Boltzmann factor

The second toy model is the following Boltmann factor

$$e^{-S_\epsilon(\theta)} = \cos(\theta) + \epsilon, \qquad \theta \in [0, 2\pi) \tag{3.56}$$

The domain of integration is the circle, and the corresponding complexified domain is the cylinder $S^1 \times \mathbb{R}$. The action possesses a sign problem when $-1 \leq \epsilon \leq 1$, and otherwise does not have a sign problem, as one can see from the plot of the Boltzmann factor in Figure 3.4.3.2. The average sign scales like ϵ for small ϵ.

In the presence of a sign problem, we complexify θ to increase the average sign, which turns out not to work. This can be shown by examining the behavior of the quenched partition function on the cylinder

$$Z_Q = \int_0^{2\pi} |\cos(\theta + i\phi(\theta)) + \epsilon| \tag{3.57}$$

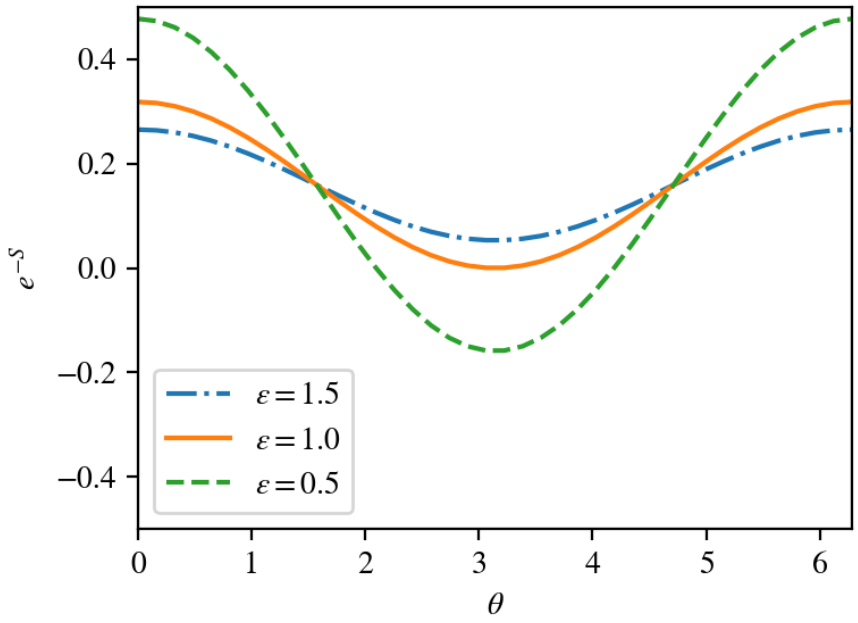

Figure 3.6: The Boltzmann factor Eq. (3.56) with $\epsilon = 0.5, 1.0, 1.5$

where $\phi(\theta)$ gives the shift of points ϕ into the complex plane. The magnitude of the Boltzmann factor is

$$|\cos(\theta + i\phi(\theta)) + \epsilon|^2 = \frac{1}{8}\left(\cos(2\theta) + \cosh(2\phi) + \epsilon\cos(\theta)\cosh(\phi)/2 + \epsilon^2\right) \tag{3.58}$$

which is minimum when $\phi = 0$ for all θ. Therefore the circle at $\phi = 0$ has the largest average sign, and we conclude that there is no globally perfect manifold which gives the average sign of 1 in the cylinder. The circle with $\phi = 0$ is still a locally perfect manifold divided by "zeros" at $\theta = \cos^{-1}(\epsilon)$. Segments divided by those zeros cancel with each other and cause a sign problem.

The failure of the construction of globally perfect manifolds due to the zeros can also be observed from the point of view of the normalizing flow. As the manifold of integration is compact, the normalizing flow is defined to be a map from the distribution in Eq. (3.56) to the

uniform distribution in $[0, 2\pi)$. Thus the normalizing flow $\theta(x)$ satisfies

$$\frac{\mathrm{d}\theta(x)}{\mathrm{d}x}\frac{\cos(\theta(x))+\epsilon}{\epsilon} = 1. \tag{3.59}$$

The inverse of the map, $x(\theta)$ is

$$x(\theta) = \left(\sin(\theta) + \epsilon\theta\right)/\epsilon \tag{3.60}$$

which is invertible when $\epsilon \geq 1$, as are plotted in Figure 3.4.3.2. Now we lower the parameter ϵ and get into the regime with the sign problem. As ϵ is lowered, the normalizing flow $\theta(x)$ becomes a multi-value map, and thus can no longer work as a map. The cause of this issue can be seen in the definition of the normalizing flow in Eq. (3.59). When $\epsilon = 0$, the Boltzmann factor vanishes at $\theta = \pi$. For the equality Eq. (3.59) to still hold, the Jacobian $\frac{\mathrm{d}\theta(x)}{\mathrm{d}x}$ needs to diverge, as is seen in Figure 3.4.3.2. Now as we lower ϵ, the slope of the inverse map $x(\theta)$ becomes negative at $\theta = \pi$, while the Jacobian diverges at $\theta = \pm\cos^{-1}(\epsilon)$ and the map $\theta(x)$ is forced to be multi-valued. Therefore, the map $\theta(x)$ can no longer be used as a normalizing flow.

The study of the behavior of normalizing flows with a vanishing Boltzmann factor was motivated by lattice QCD. The Boltzmann factor of QCD at finite density has vanishing Dirac determinant. In [17], it was shown that a perfect manifold does not exist for the $0+1$- dimensional Thirring model in the mean-field approximation. However, neither the demonstration above nor the Thirring model in the mean-field approximation serves as the proof of the non-existence of perfect manifolds and normalizing flows for the finite-density sign problem. The existence of perfect manifolds for the finite-density sign problem remains an important open question.

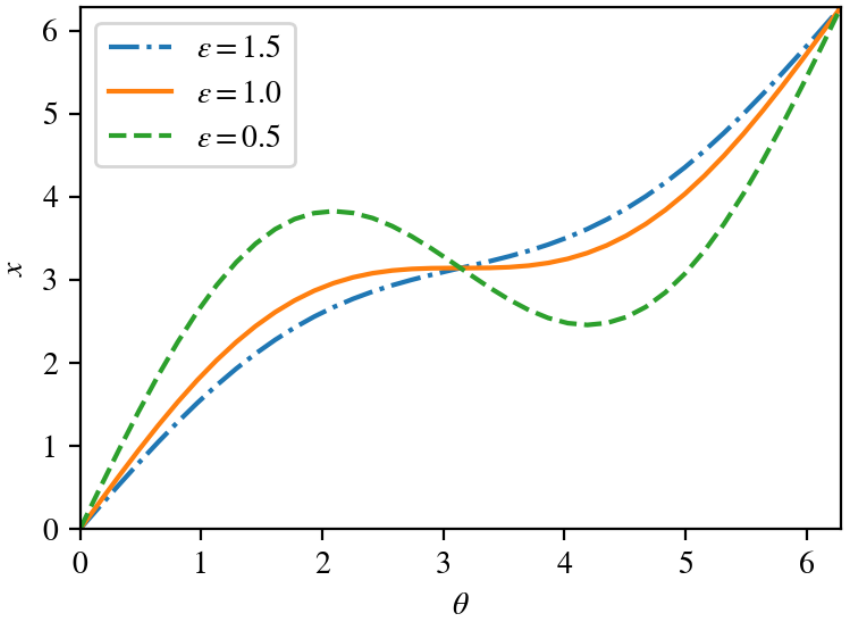

Figure 3.7: The inverse of the normalizing flow, $x(\theta)$ in Eq. (3.60), with $\epsilon = 0.5, 1.0, 1.5$.

3.5 Numerical search of complex normalizing flows

Lattice field theories of our interest usually have a large number of degrees of freedom due to the number of lattice sites and the number of degrees of freedom of fields on each site. As a result, the search for complex normalizing flows amounts to solving the single equation defining the map:

$$\det\left(\frac{\partial\phi}{\partial x}\right) e^{-S(\phi)} = \mathcal{N} g_N(x) \tag{3.61}$$

for a large number N. The differential equation above may be intractable via analytical approaches — even perturbatively as done in Sec. 3.4.2, analytical calculations of the perturbative maps for higher orders in the expansion parameter seem to be a tough exercise. Thus one is lead to consider numerical searches for approximate normalizing flows or perfect manifolds. In either case, perfect manifolds or normalizing flows, one robust way to numerically search them is to

start by preparing a large family of candidates. As was demonstrated in [141] the sign-optimized manifold method starts by preparing a family of manifolds and optimizes the sign problem within the family. To search for a perfect manifold, such manifolds without a sign problem has to be included in the family to begin with. The search for normalizing flows [146, 147, 148, 149, 150] is done with the same spirit. One prepares a neural network which represents the map, and trains the neural network such that the it well-approximates the normalizing flow. This idea of "training the map within a large family" can be directly applied to the search of complex normalizing flows, although some technical difficulties arise as will be discussed later in the section.

As a demonstration of the search for normalizing flows via machine learning, I consider a "perturbing flow" in the following [17]. Inspired by the derivation of the peturbative maps in Sec. 3.4.2, I take the ϕ^4 lattice scalar field theory in Eq. (3.50) and consider evaluating the expectation value of an observable $\mathcal{O}$. To formulate this into a problem of finding a normalizing flow, I perturb the action S_ϕ with $\mathcal{O}$ as in Eq. (3.35) but now its S_0 should be thought of as the full action S_ϕ in Eq. (3.50). The perturbing flow Δ is a map from the Boltzmann factor e^{-S_ϵ} with $S_\epsilon = S_\phi + \epsilon\mathcal{O}$ to e^{-S_ϕ} up to the linear order in the perturbation ϵ. The perturbing flow should satisfy the following differential equation:

$$\nabla \cdot \Delta - \Delta \cdot \nabla S_\phi = \mathcal{O} - \langle \mathcal{O} \rangle. \tag{3.62}$$

where the expectation value on the RHS is evaluated with S_ϕ, which is what I aim to estimate. Thus, we regard $\langle \mathcal{O} \rangle$ as a parameter and train it along with the perturbing flow Δ. The map Δ is represented with a multi-layer Perceptron (MLP) with a set of parameters W. I train these

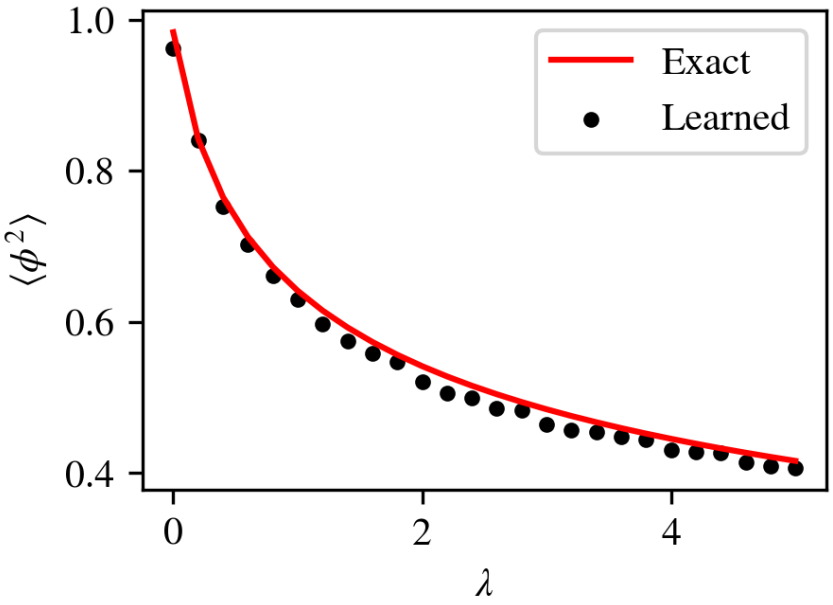

Figure 3.8: The expectation values of ϕ^2 in the scalar field theory Eq. (3.50) are estimated with the perturbing flow on a lattice with $N_\beta = 10$, $N_t = 0$, $m = 0.5$ with varying coupling λ and shown in black dots. The exact expectation values are shown in the red solid line.

parameters W such that the cost function, the LHS minus RHS of Eq. (3.62)

$$C(W, E) = \int \mathrm{d}\phi \, e^{-\phi^2/2} \times \left| \nabla \cdot \Delta_W(\phi) - \Delta_W(\phi) \cdot \nabla S_\phi(\phi) - \langle \mathcal{O} \rangle + \mathcal{O}(\phi) \right|^2 . \tag{3.63}$$

is minimized. The cost function was estimated by a random sampling from the Gaussian distribution.

The demonstration with $0 + 1$-dimensional scalar field theory with no time-evolution is shown in Figure 3.8. Lattice parameters are $N_\beta = 10$, $N_t = 0$, $m = 0.5$ with varying coupling λ. The expectation value of ϕ^2 was estimated. A two-layer MLP was used with hyperbolic tangent as an activation function. The expectation values estimated with the perturbing flow are seen to have reasonable agreements with the exact answer across the wide range of couplings.

This method has several issues that should be mentioned. First of all, the errors in estimating

the expectation values $\langle\phi^2\rangle$ come not only from insufficient statistics in training Δ_W but also from the choice of the parameterization W itself. Thus a faithful estimate of errors on the expectation values is impossible within a training of the perturbing flow. Secondly, as the perturbing map is defined between S_ϕ and its perturbation via $\mathcal{O}$, a natural cost function is

$$C'(W,E) = \int \mathrm{d}\phi\, e^{-S_\phi} \times \left|\nabla\cdot\Delta_W(\phi) - \Delta_W(\phi)\cdot\nabla S_\phi(\phi) - E + \mathcal{O}(\phi)\right|^2 \tag{3.64}$$

where the field values are sampled from e^{-S_ϕ} to estimate the cost function. This process itself possesses a sign problem when the real-time evolution is present. The estimate of the naive cost function in Eq. (3.63) can be done without a sign problem, but the estimated perturbing map Δ is not necessarily a good approximation to the true perturbing map. In addition to that, as we take the magnitude in these cost functions, we lose some information about the map in the training process. In particular, the phase of the map Δ_W is completely discarded while the cost function is computed. This could be another cause of the mismatch between the estimated Δ and the true perturbing map. To demonstrate these issues, we trained the perturbing flow as well as the expectation value of the correlator as shown in Figure 3.9. Lattice parameters used are $N_\beta = 2, m = 0.5, \lambda = 0.2$, and various time evolution N_t. Although the expectation values estimated with the perturbing map capture some features of the exact answers in dots, it is fair to conclude that the perturbing flow could not estimate them with the naive cost function in Eq. (3.63).

Some of the lessons learned in the demonstration above can be utilized in the numerical search for the normalizing flows. When searching for a normalizing flow, the honest cost function is exactly Eq. (3.63). Thus unlike for the perturbing flow above, the estimate of the cost function

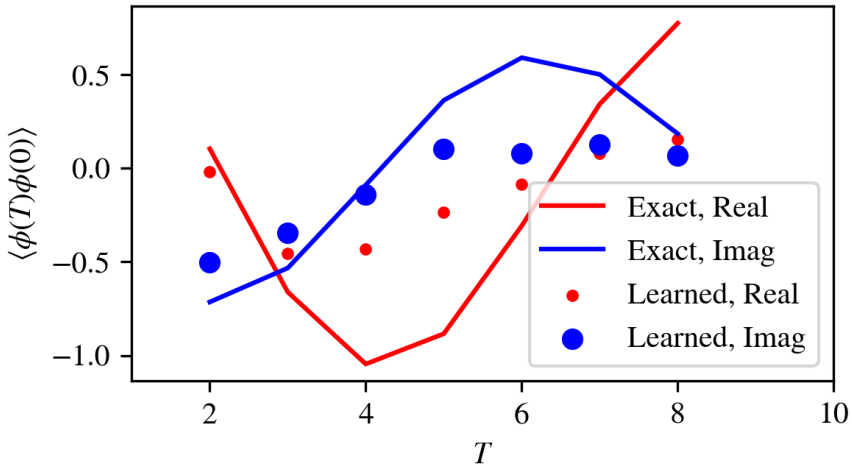

Figure 3.9: The expectation values of ϕ^2 in the scalar field theory Eq. (3.50) are estimated with the perturbing flow on a lattice with $N_\beta = 2, m = 0.5, \lambda = 0.2$, and various time evolution N_t and are shown in solid lines. Exact expectation values are shown in dots.

is done with the sampling from the Gaussian distribution function and yields no sign problems. However, another issue seen here will appear in the search for normalizing flows as well. It comes from the fact that the magnitude of the LHS minus RHS of Eq. (3.62) needs to be taken when evaluating the cost function. While taking the magnitude, one loses information about the phase of the normalizing flow. Thus it is probably necessary to train the neural network slowly enough so that such phase information will not be missed too badly. Such technical details of the machine learning based algorithms for searching normalizing flows are currently being investigated.

Chapter 4: Summary

This thesis discusses algorithms for simulating real-time dynamics of quantum field theories on the lattice. Both quantum algorithms described in Chapter 2 and classical algorithms in Chapter 3 require further work until one obtains results from lattice QCD that can be compared to experiments.

In Chapter 2, quantum algorithms for simulating general lattice gauge theories, including the mapping of their Hilbert space onto qubits, the construction of time-evolution operators, and algorithms for evaluating expectation values of Wilson loops, were discussed. As a demonstration, the time evolution of D_4 (the dihedral group) gauge theory on a two-plaquette lattice was simulated and the expectation values of a plaquette and a temporal Wilson loop were computed. The time-evolution operator was constructed from the primitive D_4 register gates: the inversion gate, the multiplication gate, the trace gate, the Fourier transform gate, and the phase gate in Appendix A. To simulate other gauge theories on a lattice within the framework described in Chapter 2, these primitive register gates need to be designed accordingly. For $SU(N)$ gauge theories, the Hilbert space on each gauge link needs to be truncated and a suitable time-evolution operator needs to be constructed.

In Sec. 2.4, quantum algorithms for computing parton distribution functions (PDFs) were discussed. Quantum computation of PDFs can be generalized to generalized PDFs, for which

appropriate algorithms for initial state preparation and measurement of relevant correlators should be developed. The quantum cost, *i.e.* the required number of qubits and depth of quantum circuit, for such algorithms should be discussed.

In Sec. 2.5, quantum algorithms for computing the transport coefficients in relativistic hydrodynamics were discussed. In this section, firstly, naive ideas for quantum algorithms for the state preparation of a thermal state of QCD were described. The details of these algorithms need to be filled in and the quantum cost of those algorithms should be estimated. Regarding the measurement of the correlators of the energy-momentum tensor, from which one extracts the transport coefficients, the finite-volume effects and the effects of thermal fluctuation in relativistic hydrodynamics should be studied — these corrections are present in heavy-ion collisions.

In Chapter 3, the application of normalizing flows to sign problems in lattice QCD was discussed. A normalizing flow, in the context of lattice field theories, is a map $\mathbb{R}^N \to \mathbb{R}^N$ which transforms the N-dimensional Gaussian distribution (or other trivial N-dimensional distributions) to the Boltzmann factor e^{-S}. Here N is the number of degrees of freedom on the lattice taking values in $\mathbb{R}$. To apply normalizing flows to a lattice field theory with a sign problem, whose Boltzmann factor takes negative or even complex values, a normalizing flow needs to map variables in $\mathbb{R}^N$ to complex values in $\mathbb{C}^N$ — the space of complexified field variables on the lattice. We call such a map a "complex normalizing flow", which induces a deformed manifold of integration in the complex plane of the original fields in the lattice field theory. Thus the complex normalizing flow method is conceptually equivalent to the manifold deformation methods as was discussed in Chapter 3. Moreover, the manifold of integration induced by a complex normalizing flow has no sign problem, which I referred to as a "perfect manifold".

Using both the manifold deformation methods and the complex normalizing flow, the

existence of a perfect manifold of integration (which has no sign problem), and equivalently an ideal complex normalizing flow, were discussed in Sec. 3.4. For bosonic lattice field theories, such as ϕ^4 real scalar field theory and $SU(N)$ gauge theories, such perfect manifolds are likely to exist, based on the construction of locally perfect manifolds using the holomorphic gradient flow and analytic continuation of complex normalizing flows as were discussed in this section. As the next step toward solving the real-time sign problem for bosonic field theories of our interest, algorithms based on tools from machine learning for searching perfect manifolds or complex normalizing flows are currently studied.

When the Boltzmann factor can vanishes in the complex plane of field variables, the existence of a perfect manifold is no longer guaranteed as was discussed in Sec. 3.4. When a deformed manifold of integration intersects with such a point with vanishing e^{-S} in the complex plane, a "global sign problem" may be introduced. In lattice QCD, the Boltzmann factor can vanish in both Minkowski lattice QCD and Euclidean lattice QCD at finite density. When the quark degrees of freedom are integrated out from the lattice QCD path integral, the path integral obtains the fermion determinant, which can vanish in the complex plane. Nevertheless, contour deformation methods and complex normalizing flows may be able to alleviate sign problems enough and let us extract useful information about QCD from the lattice calculations. The applicability of these methods to sign problems in lattice QCD should be explored. In parallel with such numerical tests, one should explore other ways to treat fermions on the lattice in which the Boltzmann factor does not vanish in the complex plane. If such a method is found, the existence of a perfect manifold may be guaranteed, and thus sign problem may be solved.

Appendix A: Primitive circuits for the D_4 gauge theory

The dihedral group D_4 is the symmetry group of the square. In a matrix representation, its eight elements can be written as a combination of two matrices: the $\pi/2$ rotation matrix and the reflection matrix

$$O = \begin{pmatrix} i & 0 \\ 0 & -i \end{pmatrix} \text{ and } R = \begin{pmatrix} 0 & 1 \\ 1 & 0 \end{pmatrix}. \tag{A.1}$$

respectively. Eight elements of the group are represented as $g = M_{rot}^n M_{ref}^m$ with $n = 0, 1$ and $m = 0, 1, 2, 3$. Therefore on a quantum computer, the eight elements $|abc\rangle$ $(a, b, c = 0, 1)$ can be implemented using three qubits to represent matrices

$$\left[\begin{pmatrix} 0 & 1 \\ 1 & 0 \end{pmatrix}\right]^a \left[\left[\begin{pmatrix} i & 0 \\ 0 & -i \end{pmatrix}\right]^{2b+c}\right]. \tag{A.2}$$

Here, two qubits denoted by b and c specify the amount of rotation $(2b + c)\pi/2$ and the qubit a performs the reflection if $a = 1$. This is our design of the D_4 register.

Having the D_4 register designed, the primitive gates to act on registers — the inversion gate Eq. (2.20), the multiplication gate Eq. (2.21), the trace gate Eq. (2.22), and the Fourier transformation gate Eq. (2.23) — need to be implemented. The inversion can be implemented

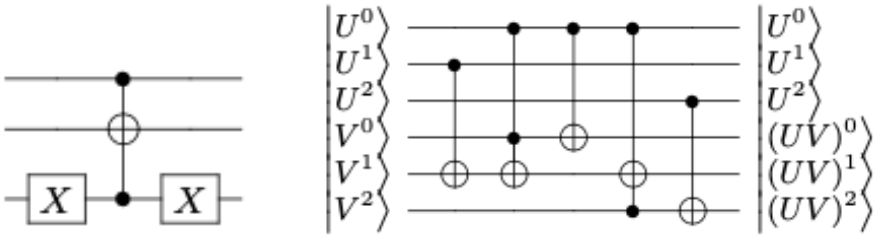

Figure A.1: The inversion gate and multiplication gate for D_4 register.

simply as is shown in FIG. A.1. For the D_4 group, the inverse of each element is

$$I \leftrightarrow I, \;\; O \leftrightarrow O^3, \;\; O^2 \rightarrow O^2, \;\; R \leftrightarrow R, \;\; RO \leftrightarrow RO, \;\; RO^2 \leftrightarrow RO^2, \;\; RO^3 \leftrightarrow RO^3. \quad \text{(A.3)}$$

Therefore, with the D_4 register in Eq. (A.2), only when $a = 0$ and $c = 1$, b needs to be flipped, and otherwise no operation should happen. Such circuit can be implemented by three-qubit controlled gate with a, c serving as control qubits and b being the target qubit. In the common convention, the target qubit is flipped when the controlled gate is "1". Thus a qubit needs to be flipped before the controlled gate and then flipped back by Pauli-X gates. This construction leads to the circuit on the left in FIG. A.1, where the three lines represent qubits in the order c, b, a from the top.

The multiplication gate is more complicated as is shown in the right panel of FIG. A.1. Ultimately the circuit should perform operations on two registers following the multiplication table of the group in Table. A.1. Let us denote three indices of two registers (a_1, b_1, c_1) and (a_2, b_2, c_2), and the resulting multiple of the two register on the second register as (a, b, c):

$$\mathfrak{U}_\times |a_1 b_1 c_1\rangle |a_2 b_2 c_2\rangle = |a_1 b_1 c_1\rangle |abc\rangle. \quad \text{(A.4)}$$

Thus the multiplication gate should be implemented such that (a_1, b_1, c_1) which can be regarded

	$(0,0,0)$	$(0,0,1)$	$(0,1,0)$	$(0,1,1)$	$(1,0,0)$	$(1,0,1)$	$(1,1,0)$	$(1,1,1)$
$(0,0,0)$	$(0,0,0)$	$(0,0,1)$	$(0,1,0)$	$(0,1,1)$	$(1,0,0)$	$(1,0,1)$	$(1,1,0)$	$(1,1,1)$
$(0,0,1)$	$(0,0,1)$	$(0,1,0)$	$(0,1,1)$	$(0,0,0)$	$(1,1,1)$	$(1,0,0)$	$(1,0,1)$	$(1,1,0)$
$(0,1,0)$	$(0,1,0)$	$(0,1,1)$	$(0,0,0)$	$(0,0,1)$	$(1,1,0)$	$(1,1,1)$	$(1,0,0)$	$(1,0,1)$
$(0,1,1)$	$(0,1,1)$	$(0,0,0)$	$(0,0,1)$	$(0,1,0)$	$(1,0,1)$	$(1,1,0)$	$(1,1,1)$	$(1,0,0)$
$(1,0,0)$	$(1,0,0)$	$(1,0,1)$	$(1,1,0)$	$(1,1,1)$	$(0,0,0)$	$(0,0,1)$	$(0,1,0)$	$(0,1,1)$
$(1,0,1)$	$(1,0,1)$	$(1,1,0)$	$(1,1,1)$	$(1,0,0)$	$(0,1,1)$	$(0,0,0)$	$(0,0,1)$	$(0,1,0)$
$(1,1,0)$	$(1,1,0)$	$(1,1,1)$	$(1,0,0)$	$(1,0,1)$	$(0,1,0)$	$(0,1,1)$	$(0,0,0)$	$(0,0,1)$
$(1,1,1)$	$(1,1,1)$	$(1,0,0)$	$(1,0,1)$	$(1,1,0)$	$(0,0,1)$	$(0,1,0)$	$(0,1,1)$	$(0,0,0)$

Table A.1: Multiplication table for dihedral D_4 group. Each element are represented by the three indices as in Eq. (A.2) in the form (a,b,c).

as the column and (a_2,b_2,c_2) as the row of Table. A.1 give the corresponding multiplication of them to the resulting second register (a,b,c).

The largest structure which determines a is that when $a_1=0$, $a=a_2$, and otherwise a_2 needs to be flipped. This can be simply achieved by two-qubit controlled gate on a_1 and a_2 with a_1 serving as control qubit and a_2 being the target qubit.

Having a taken care of, I can now focus b and c. The next largest structure one can see in Table. A.1 is the contrast between cases $a_2=0$ and $a_2=1$. The multiplication with $a_2=1$ cases can be obtained by applying the following operation to the multiplication for $a_2=0$ cases but with the same other a_1,b_1,c_1,b_2,c_2:

$$\text{flip } b_1 \text{ when } a_2=1 \text{ and } c_1=1$$

This operation can be achieved by a three-qubit controlled gate with a_2,c_1 controlled and b_1 being the target qubit. Between cases $a_2=0,1$, c is the same as long as other as and bs are the same.

Now that I have implemented the difference between $a_2=0$ and $a_2=1$ cases, I can focus on $a_2=0$ cases (the left half of Table. A.1) and investigate how b and c are determined from b_1,b_2,c_1 and c_2. We find that the relation between b_1,c_1,b_2,c_2,b,c is a simple addition in the

binary representation:

$$2b + c = 2b_1 + c_1 + 2b_2 + c_2 \pmod 4 \tag{A.5}$$

Thus, regarding b, b_2 should be flipped when $b_1 = 1$, and flipped again when $c_1 = 1$ and $c_2 = 1$. Regarding c, c_2 should be flipped when $c_1 = 1$ but otherwise $c = c_2$. Thus, one should first apply two controlled gates to change b_2 to an appropriate b as this operation depends on c_2: a two-qubit gate with b_1 control and b_2 target, and a three-qubit gate with c_1, c_2 control and b_2 target. Then one changes c_2 to an appropriate c by applying a two-qubit controlled gate with c_1 being the control qubit and c_2 being the target qubit. The whole circuit consists of five controlled gates as shown in FIG. A.1, where again the three lines represent qubits in the order c, b, a from the top for the register U and V.

The trace gate $\mathfrak{U}_{\mathrm{Tr}}$ acts on a single register. The trace of D_4 group elements are non-zero only when $a = 0$ and $c = 0$, and $\mathfrak{U}_{\mathrm{Tr}}(\theta)|000\rangle = e^{-2i\theta}|000\rangle$, $\mathfrak{U}_{\mathrm{Tr}}(\theta)|010\rangle = e^{2i\theta}|010\rangle$. Thus the trace gate can be implemented with a controlled phase gate (a, c are the control and b is the target).

The Fourier transform gate $\mathfrak{U}_F$ which acts on a single register is given in the following

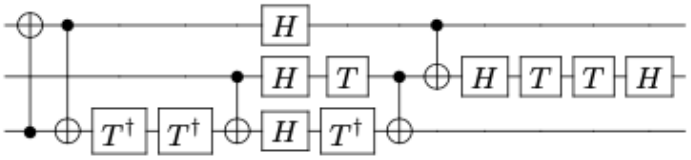

Figure A.2: The Fourier transform gate for D_4 register.

matrix form

$$F = \begin{pmatrix} \frac{1}{\sqrt{8}} & \frac{1}{\sqrt{8}} & \frac{1}{\sqrt{8}} & \frac{1}{\sqrt{8}} & \frac{1}{\sqrt{8}} & \frac{1}{\sqrt{8}} & \frac{1}{\sqrt{8}} & \frac{1}{\sqrt{8}} \\ \frac{1}{\sqrt{8}} & \frac{1}{\sqrt{8}} & \frac{1}{\sqrt{8}} & \frac{1}{\sqrt{8}} & \frac{-1}{\sqrt{8}} & \frac{-1}{\sqrt{8}} & \frac{-1}{\sqrt{8}} & \frac{-1}{\sqrt{8}} \\ \frac{1}{\sqrt{8}} & -\frac{1}{\sqrt{8}} & \frac{1}{\sqrt{8}} & -\frac{1}{\sqrt{8}} & \frac{1}{\sqrt{8}} & -\frac{1}{\sqrt{8}} & \frac{1}{\sqrt{8}} & -\frac{1}{\sqrt{8}} \\ \frac{1}{\sqrt{8}} & -\frac{1}{\sqrt{8}} & \frac{1}{\sqrt{8}} & -\frac{1}{\sqrt{8}} & -\frac{1}{\sqrt{8}} & \frac{1}{\sqrt{8}} & -\frac{1}{\sqrt{8}} & \frac{1}{\sqrt{8}} \\ \frac{1}{2} & 0 & -\frac{1}{2} & 0 & \frac{1}{2} & 0 & -\frac{1}{2} & 0 \\ 0 & -\frac{1}{2} & 0 & \frac{1}{2} & 0 & \frac{1}{2} & 0 & -\frac{1}{2} \\ 0 & \frac{1}{2} & 0 & -\frac{1}{2} & 0 & \frac{1}{2} & 0 & -\frac{1}{2} \\ \frac{1}{2} & 0 & -\frac{1}{2} & 0 & -\frac{1}{2} & 0 & \frac{1}{2} & 0 \end{pmatrix} . \tag{A.6}$$

such that it diagonalizes the D_4 momentum operator. To find a circuit for this matrix, a *classical* simulated annealing search was performed and the circuit in FIG. A.2 was found to exactly implement the matrix operation above. The basic gates used are Hadamard gate, CNOT gate, and $\frac{\pi}{8}$ gate (T). After the kinetic term of the Hamiltonian Eq. (2.38) is diagonalized, an appropriate phase gate $\mathfrak{U}_{\text{phase}}$ should be applied. The phase gate can be simply implemented by two phase gates: a phase gate on qubit a and a controlled phase on the state $a = b = c = 0$:

$$\mathfrak{U}_{\text{phase}}|abc\rangle = e^{i\theta_1 \delta_{a0}\delta_{b0}\delta_{c0}} e^{i\theta_2 a}|abc\rangle \ . \tag{A.7}$$

The constants θ_1, θ_2 are coupling dependent.

Bibliography

[1] H. Fritzsch, Murray Gell-Mann, and H. Leutwyler. Advantages of the Color Octet Gluon Picture. *Phys. Lett. B*, 47:365–368, 1973.

[2] Chen-Ning Yang and Robert L. Mills. Conservation of Isotopic Spin and Isotopic Gauge Invariance. *Phys. Rev.*, 96:191–195, 1954.

[3] David J. Gross and Frank Wilczek. Ultraviolet Behavior of Nonabelian Gauge Theories. *Phys. Rev. Lett.*, 30:1343–1346, 1973.

[4] H. David Politzer. Reliable Perturbative Results for Strong Interactions? *Phys. Rev. Lett.*, 30:1346–1349, 1973.

[5] Richard P. Feynman. Very high-energy collisions of hadrons. *Phys. Rev. Lett.*, 23:1415–1417, 1969.

[6] Kenneth G. Wilson. Confinement of Quarks. *Phys. Rev. D*, 10:2445–2459, 1974.

[7] Paulo F. Bedaque and Ubirajara van Kolck. Effective field theory for few nucleon systems. *Ann. Rev. Nucl. Part. Sci.*, 52:339–396, 2002.

[8] Robert B. Wiringa, V. G. J. Stoks, and R. Schiavilla. An Accurate nucleon-nucleon potential with charge independence breaking. *Phys. Rev. C*, 51:38–51, 1995.

[9] S. R. Beane, E. Chang, S. D. Cohen, William Detmold, H. W. Lin, T. C. Luu, K. Orginos, A. Parreno, M. J. Savage, and A. Walker-Loud. Light Nuclei and Hypernuclei from Quantum Chromodynamics in the Limit of SU(3) Flavor Symmetry. *Phys. Rev. D*, 87(3):034506, 2013.

[10] L. Contessi, A. Lovato, F. Pederiva, A. Roggero, J. Kirscher, and U. van Kolck. Ground-state properties of ^{4}He and ^{16}O extrapolated from lattice QCD with pionless EFT. *Phys. Lett. B*, 772:839–848, 2017.

[11] Anton Andronic, Peter Braun-Munzinger, Krzysztof Redlich, and Johanna Stachel. Decoding the phase structure of QCD via particle production at high energy. *Nature*, 561(7723):321–330, 2018.

[12] Bjoern Schenke, Sangyong Jeon, and Charles Gale. (3+1)D hydrodynamic simulation of relativistic heavy-ion collisions. *Phys. Rev. C*, 82:014903, 2010.

[13] Henry Lamm, Scott Lawrence, and Yukari Yamauchi. General Methods for Digital Quantum Simulation of Gauge Theories. *Phys. Rev. D*, 100(3):034518, 2019.

[14] Henry Lamm, Scott Lawrence, and Yukari Yamauchi. Parton physics on a quantum computer. *Phys. Rev. Res.*, 2(1):013272, 2020.

[15] Thomas D. Cohen, Henry Lamm, Scott Lawrence, and Yukari Yamauchi. Quantum algorithms for transport coefficients in gauge theories. *Phys. Rev. D*, 104(9):094514, 2021.

[16] Andrei Alexandru, Gokce Basar, Paulo F. Bedaque, and Neill C. Warrington. Complex paths around the sign problem. *Rev. Mod. Phys.*, 94(1):015006, 2022.

[17] Scott Lawrence and Yukari Yamauchi. Normalizing Flows and the Real-Time Sign Problem. *Phys. Rev. D*, 103(11):114509, 2021.

[18] Richard Phillips Feynman and Albert Roach Hibbs. *Quantum mechanics and path integrals*. International series in pure and applied physics. McGraw-Hill, New York, NY, 1965.

[19] John B. Kogut. An Introduction to Lattice Gauge Theory and Spin Systems. *Rev. Mod. Phys.*, 51:659, 1979.

[20] John B. Kogut. A Review of the Lattice Gauge Theory Approach to Quantum Chromodynamics. *Rev. Mod. Phys.*, 55:775, 1983.

[21] Rajan Gupta. Introduction to lattice QCD: Course. In *Les Houches Summer School in Theoretical Physics, Session 68: Probing the Standard Model of Particle Interactions*, pages 83–219, 7 1997.

[22] Sundance O. Bilson-Thompson, Derek B. Leinweber, and Anthony G. Williams. Highly improved lattice field strength tensor. *Annals Phys.*, 304:1–21, 2003.

[23] Holger Bech Nielsen and M. Ninomiya. No Go Theorem for Regularizing Chiral Fermions. *Phys. Lett. B*, 105:219–223, 1981.

[24] John B. Kogut and Leonard Susskind. Hamiltonian Formulation of Wilson's Lattice Gauge Theories. *Phys. Rev. D*, 11:395–408, 1975.

[25] David B. Kaplan. A Method for simulating chiral fermions on the lattice. *Phys. Lett. B*, 288:342–347, 1992.

[26] Owe Philipsen. The QCD equation of state from the lattice. *Prog. Part. Nucl. Phys.*, 70:55–107, 2013.

[27] Philippe de Forcrand. Simulating QCD at finite density. *PoS*, LAT2009:010, 2009.

[28] Sergio Caracciolo, Giuseppe Curci, Pietro Menotti, and Andrea Pelissetto. The Energy Momentum Tensor for Lattice Gauge Theories. *Annals Phys.*, 197:119, 1990.

[29] Paul Romatschke and Ulrike Romatschke. Viscosity Information from Relativistic Nuclear Collisions: How Perfect is the Fluid Observed at RHIC? *Phys. Rev. Lett.*, 99:172301, 2007.

[30] A. K. Chaudhuri. Saturation of elliptic flow and shear viscosity. *arXiv preprint arXiv:0708.1252 [nucl-th]*, 2007.

[31] Huichao Song and Ulrich W. Heinz. Suppression of elliptic flow in a minimally viscous quark-gluon plasma. *Phys. Lett. B*, 658:279–283, 2008.

[32] K. Dusling and D. Teaney. Simulating elliptic flow with viscous hydrodynamics. *Phys. Rev. C*, 77:034905, 2008.

[33] Derek Teaney. The Effects of viscosity on spectra, elliptic flow, and HBT radii. *Phys. Rev. C*, 68:034913, 2003.

[34] Huichao Song, Steffen A. Bass, Ulrich Heinz, Tetsufumi Hirano, and Chun Shen. 200 A GeV Au+Au collisions serve a nearly perfect quark-gluon liquid. *Phys. Rev. Lett.*, 106:192301, 2011. [Erratum: Phys.Rev.Lett. 109, 139904 (2012)].

[35] P. Kovtun, Dan T. Son, and Andrei O. Starinets. Viscosity in strongly interacting quantum field theories from black hole physics. *Phys. Rev. Lett.*, 94:111601, 2005.

[36] Scott Lawrence. Resurrecting the Strong KSS Conjecture. *arXiv preprint arXiv:2111.08158 [hep-lat]*, 2021.

[37] Paul Romatschke and Ulrike Romatschke. *Relativistic Fluid Dynamics In and Out of Equilibrium*. Cambridge Monographs on Mathematical Physics. Cambridge University Press, 5 2019.

[38] Berk Hess. Determining the shear viscosity of model liquids from molecular dynamics simulations. *The Journal of chemical physics*, 116(1):209–217, 2002.

[39] Pavel Kovtun. Lectures on hydrodynamic fluctuations in relativistic theories. *J. Phys. A*, 45:473001, 2012.

[40] Paul Romatschke. New Developments in Relativistic Viscous Hydrodynamics. *Int. J. Mod. Phys. E*, 19:1–53, 2010.

[41] Juan Martin Maldacena. The Large N limit of superconformal field theories and supergravity. *Adv. Theor. Math. Phys.*, 2:231–252, 1998.

[42] Edward Witten. Anti-de Sitter space and holography. *Adv. Theor. Math. Phys.*, 2:253–291, 1998.

[43] Dam T. Son and Andrei O. Starinets. Minkowski space correlators in AdS / CFT correspondence: Recipe and applications. *JHEP*, 09:042, 2002.

[44] Giuseppe Policastro, Dam T. Son, and Andrei O. Starinets. From AdS / CFT correspondence to hydrodynamics. *JHEP*, 09:043, 2002.

[45] Pavel K. Kovtun and Andrei O. Starinets. Quasinormal modes and holography. *Phys. Rev. D*, 72:086009, 2005.

[46] Richard P. Feynman. Simulating physics with computers. *Int. J. Theor. Phys.*, 21:467–488, 1982.

[47] Marcela Carena, Henry Lamm, Scott Lawrence, Ying-Ying Li, Joseph D. Lykken, Lian-Tao Wang, and Yukari Yamauchi. Practical Quantum Advantages in High Energy Physics. *Snowmass 2021 LOI*, TF10-077, 2020.

[48] Pascual Jordan and Eugene P. Wigner. About the Pauli exclusion principle. *Z. Phys.*, 47:631–651, 1928.

[49] F. Verstraete and J. I. Cirac. Mapping local Hamiltonians of fermions to local Hamiltonians of spins. *J. Stat. Mech.*, 0509:P09012, 2005.

[50] Erez Zohar and J. Ignacio Cirac. Eliminating fermionic matter fields in lattice gauge theories. *Phys. Rev.*, B98(7):075119, 2018.

[51] James D. Whitfield, Vojtěch Havlíček, and Matthias Troyer. Local spin operators for fermion simulations. *Physical Review A*, 94:030301, September 2016.

[52] Daniel C. Hackett, Kiel Howe, Ciaran Hughes, William Jay, Ethan T. Neil, and James N. Simone. Digitizing Gauge Fields: Lattice Monte Carlo Results for Future Quantum Computers. *Phys. Rev. A*, 99(6):062341, 2019.

[53] Andrei Alexandru, Paulo F. Bedaque, Siddhartha Harmalkar, Henry Lamm, Scott Lawrence, and Neill C. Warrington. Gluon Field Digitization for Quantum Computers. *Phys. Rev. D*, 100(11):114501, 2019.

[54] Yao Ji, Henry Lamm, and Shuchen Zhu. Gluon Field Digitization via Group Space Decimation for Quantum Computers. *Phys. Rev. D*, 102(11):114513, 2020.

[55] Andrei Alexandru, Paulo F. Bedaque, Ruairí Brett, and Henry Lamm. The spectrum of qubitized QCD: glueballs in a $S(1080)$ gauge theory. *arXiv preprint arXiv:2112.08482 [hep-lat]*, 2021.

[56] Yao Ji, Henry Lamm, and Shuchen Zhu. Gluon Digitization via Character Expansion for Quantum Computers. *arXiv preprint arXiv:2203.02330 [hep-lat]*, 2022.

[57] Natalie Klco and Martin J. Savage. Digitization of scalar fields for quantum computing. *Phys. Rev. A*, 99(5):052335, 2019.

[58] Natalie Klco, Jesse R. Stryker, and Martin J. Savage. SU(2) non-Abelian gauge field theory in one dimension on digital quantum computers. *Phys. Rev. D*, 101(7):074512, 2020.

[59] Anthony Ciavarella, Natalie Klco, and Martin J. Savage. Trailhead for quantum simulation of SU(3) Yang-Mills lattice gauge theory in the local multiplet basis. *Phys. Rev. D*, 103(9):094501, 2021.

[60] Ramesh Anishetty, Manu Mathur, and Indrakshi Raychowdhury. Prepotential formulation of SU(3) lattice gauge theory. *J. Phys. A*, 43:035403, 2010.

[61] Indrakshi Raychowdhury. *Prepotential Formulation of Lattice Gauge Theories*. PhD thesis, Calcutta U., 2013.

[62] Indrakshi Raychowdhury. Low energy spectrum of SU(2) lattice gauge theory: An alternate proposal via loop formulation. *Eur. Phys. J. C*, 79(3):235, 2019.

[63] Indrakshi Raychowdhury and Jesse R. Stryker. Solving Gauss's Law on Digital Quantum Computers with Loop-String-Hadron Digitization. *Phys. Rev. Res.*, 2(3):033039, 2020.

[64] Indrakshi Raychowdhury and Jesse R. Stryker. Loop, string, and hadron dynamics in SU(2) Hamiltonian lattice gauge theories. *Phys. Rev. D*, 101(11):114502, 2020.

[65] Zohreh Davoudi, Indrakshi Raychowdhury, and Andrew Shaw. Search for efficient formulations for Hamiltonian simulation of non-Abelian lattice gauge theories. *Phys. Rev. D*, 104(7):074505, 2021.

[66] E. A. Martinez et al. Real-time dynamics of lattice gauge theories with a few-qubit quantum computer. *Nature*, 534:516–519, 2016.

[67] N. Klco, E. F. Dumitrescu, A. J. McCaskey, T. D. Morris, R. C. Pooser, M. Sanz, E. Solano, P. Lougovski, and M. J. Savage. Quantum-classical computation of Schwinger model dynamics using quantum computers. *Phys. Rev.*, A98(3):032331, 2018.

[68] Alexei Bazavov, Yannick Meurice, Shan-Wen Tsai, Judah Unmuth-Yockey, and Jin Zhang. Gauge-invariant implementation of the Abelian Higgs model on optical lattices. *Phys. Rev.*, D92(7):076003, 2015.

[69] Jin Zhang, J. Unmuth-Yockey, J. Zeiher, A. Bazavov, S. W. Tsai, and Y. Meurice. Quantum simulation of the universal features of the Polyakov loop. *Phys. Rev. Lett.*, 121(22):223201, 2018.

[70] Judah F. Unmuth-Yockey. A gauge-invariant, rotor Hamiltonian from dual variables of 3D U(1) gauge theory. 2018.

[71] Judah Unmuth-Yockey, Jin Zhang, Alexei Bazavov, Yannick Meurice, and Shan-Wen Tsai. Universal features of the Abelian Polyakov loop in 1+1 dimensions. *Phys. Rev.*, D98(9):094511, 2018.

[72] T. V. Zache, F. Hebenstreit, F. Jendrzejewski, M. K. Oberthaler, J. Berges, and P. Hauke. Quantum simulation of lattice gauge theories using Wilson fermions. *Sci. Technol.*, 3:034010, 2018.

[73] Christine Muschik, Markus Heyl, Esteban Martinez, Thomas Monz, Philipp Schindler, Berit Vogell, Marcello Dalmonte, Philipp Hauke, Rainer Blatt, and Peter Zoller. U(1) Wilson lattice gauge theories in digital quantum simulators. *New J. Phys.*, 19(10):103020, 2017.

[74] Yoshihito Kuno, Kenichi Kasamatsu, Yoshiro Takahashi, Ikuo Ichinose, and Tetsuo Matsui. Real-time dynamics and proposal for feasible experiments of lattice gauge–Higgs model simulated by cold atoms. *New J. Phys.*, 17(6):063005, 2015.

[75] Tim Byrnes and Yoshihisa Yamamoto. Simulating lattice gauge theories on a quantum computer. *Phys. Rev.*, A73:022328, 2006.

[76] D. Banerjee, M. Bögli, M. Dalmonte, E. Rico, P. Stebler, U. J. Wiese, and P. Zoller. Atomic Quantum Simulation of U(N) and SU(N) Non-Abelian Lattice Gauge Theories. *Phys. Rev. Lett.*, 110(12):125303, 2013.

[77] Uwe-Jens Wiese. Ultracold Quantum Gases and Lattice Systems: Quantum Simulation of Lattice Gauge Theories. *Annalen Phys.*, 525:777–796, 2013.

[78] Erez Zohar, J. Ignacio Cirac, and Benni Reznik. Cold-Atom Quantum Simulator for SU(2) Yang-Mills Lattice Gauge Theory. *Phys. Rev. Lett.*, 110(12):125304, 2013.

[79] Christian Kokail et al. Self-verifying variational quantum simulation of lattice models. *Nature*, 569(7756):355–360, 2019.

[80] Alberto Peruzzo, Jarrod McClean, Peter Shadbolt, Man-Hong Yung, Xiao-Qi Zhou, Peter J Love, Alán Aspuru-Guzik, and Jeremy L O'brien. A variational eigenvalue solver on a photonic quantum processor. *Nature communications*, 5:4213, 2014.

[81] Daniel S. Abrams and Seth Lloyd. A Quantum algorithm providing exponential speed increase for finding eigenvalues and eigenvectors. *Phys. Rev. Lett.*, 83:5162–5165, 1999.

[82] Nathan Wiebe and Chris Granade. Efficient bayesian phase estimation. *Phys. Rev. Lett.*, 117:010503, Jun 2016.

[83] Edward Farhi, Jeffrey Goldstone, Sam Gutmann, and Michael Sipser. Quantum computation by adiabatic evolution. *arXiv preprint quant-ph/0001106*, 2000.

[84] David B. Kaplan, Natalie Klco, and Alessandro Roggero. Ground States via Spectral Combing on a Quantum Computer. *arXiv preprint arXiv:1709.08250 [quant-ph]*, 2017.

[85] Henry Lamm and Scott Lawrence. Simulation of Nonequilibrium Dynamics on a Quantum Computer. *Phys. Rev. Lett.*, 121(17):170501, 2018.

[86] Siddhartha Harmalkar, Henry Lamm, and Scott Lawrence. Quantum Simulation of Field Theories Without State Preparation. *arXiv preprint arXiv:2001.11490 [hep-lat]*, 1 2020.

[87] Henry Lamm, Scott Lawrence, and Yukari Yamauchi. Suppressing Coherent Gauge Drift in Quantum Simulations. *arXiv preprint arXiv:2005.12688 [quant-ph]*, 5 2020.

[88] Minh C. Tran, Yuan Su, Daniel Carney, and Jacob M. Taylor. Faster Digital Quantum Simulation by Symmetry Protection. *PRX Quantum*, 2:010323, 2021.

[89] Jad C. Halimeh, Haifeng Lang, and Philipp Hauke. Gauge protection in non-abelian lattice gauge theories. *New J. Phys.*, 24(3):033015, 2022.

[90] Michael Creutz. Gauge Fixing, the Transfer Matrix, and Confinement on a Lattice. *Phys. Rev. D*, 15:1128, 1977.

[91] Jesse R. Stryker. Oracles for Gauss's law on digital quantum computers. *Phys. Rev. A*, 99(4):042301, 2019.

[92] G. Ortiz, J. E. Gubernatis, E. Knill, and R. Laflamme. Quantum algorithms for fermionic simulations. *Phys. Rev. A*, 64:022319, 2001. [Erratum: Phys.Rev.A 65, 029902 (2002)].

[93] M. Tanabashi et al. Review of particle physics. *Phys. Rev. D*, 98:030001, Aug 2018.

[94] U. Aglietti, Marco Ciuchini, G. Corbo, E. Franco, G. Martinelli, and L. Silvestrini. Model independent determination of the shape function for inclusive B decays and of the structure functions in DIS. *Phys. Lett.*, B432:411–420, 1998.

[95] Keh-Fei Liu. Parton degrees of freedom from the path integral formalism. *Phys. Rev.*, D62:074501, 2000.

[96] A. J. Chambers, R. Horsley, Y. Nakamura, H. Perlt, P. E. L. Rakow, G. Schierholz, A. Schiller, K. Somfleth, R. D. Young, and J. M. Zanotti. Nucleon Structure Functions from Operator Product Expansion on the Lattice. *Phys. Rev. Lett.*, 118(24):242001, 2017.

[97] Xiangdong Ji. Parton Physics on a Euclidean Lattice. *Phys. Rev. Lett.*, 110:262002, 2013.

[98] A. V. Radyushkin. Quasi-parton distribution functions, momentum distributions, and pseudo-parton distribution functions. *Phys. Rev.*, D96(3):034025, 2017.

[99] Yan-Qing Ma and Jian-Wei Qiu. Extracting Parton Distribution Functions from Lattice QCD Calculations. *Phys. Rev.*, D98(7):074021, 2018.

[100] Alan C Santos. The ibm quantum computer and the ibm quantum experience. *Revista Brasileira de Ensino de Física*, 39(1), 2017.

[101] Andrew W Cross, Lev S Bishop, John A Smolin, and Jay M Gambetta. Open quantum assembly language. *arXiv preprint arXiv:1707.03429*, 2017.

[102] J. S. Pedernales, R. Di Candia, I. L. Egusquiza, J. Casanova, and E. Solano. Efficient quantum algorithm for computing n-time correlation functions. *Phys. Rev. Lett.*, 113:020505, Jul 2014.

[103] Gert Aarts and Jose Maria Martinez Resco. Transport coefficients, spectral functions and the lattice. *JHEP*, 04:053, 2002.

[104] Harvey B. Meyer. Transport Properties of the Quark-Gluon Plasma: A Lattice QCD Perspective. *Eur. Phys. J. A*, 47:86, 2011.

[105] Yasuhiro Kohno, Masayuki Asakawa, and Masakiyo Kitazawa. Shear viscosity to relaxation time ratio in SU(3) lattice gauge theory. *Phys. Rev. D*, 89(5):054508, 2014.

[106] Gert Aarts, Chris Allton, Alessandro Amato, Pietro Giudice, Simon Hands, and Jon-Ivar Skullerud. Electrical conductivity and charge diffusion in thermal QCD from the lattice. *JHEP*, 02:186, 2015.

[107] Etsuko Itou and Yuki Nagai. Sparse modeling approach to obtaining the shear viscosity from smeared correlation functions. *JHEP*, 07:007, 2020.

[108] Johannes Roßnagel, Samuel T Dawkins, Karl N Tolazzi, Obinna Abah, Eric Lutz, Ferdinand Schmidt-Kaler, and Kilian Singer. A single-atom heat engine. *Science*, 352(6283):325–329, 2016.

[109] Ronnie Kosloff and Amikam Levy. Quantum heat engines and refrigerators: Continuous devices. *Annual Review of Physical Chemistry*, 65(1):365–393, 2014.

[110] Scott Lawrence. *Sign Problems in Quantum Field Theory: Classical and Quantum Approaches*. PhD thesis, Maryland U., 2020.

[111] Niklas Mueller, Torsten V. Zache, and Robert Ott. Thermalization of Gauge Theories from their Entanglement Spectrum. *arXiv preprint arVix:2107.11416 [quant-ph]*, 7 2021.

[112] Xiang-Qian Luo, Shuo-Hong Guo, Helmut Kroger, and Dieter Schutte. Improved lattice gauge field Hamiltonian. *Phys. Rev. D*, 59:034503, 1999.

[113] Jesse Carlsson and Bruce H. J. McKellar. Direct improvement of Hamiltonian lattice gauge theory. *Phys. Rev. D*, 64:094503, 2001.

[114] Xiang-Qian Luo, Qi-Zhou Chen, Guo-cai Xu, and Jun-Qin Jiang. Improved Hamiltonians for lattice gauge theory with fermions. *Phys. Rev. D*, 50:501–508, 1994.

[115] Yukari Yamauchi and Scott Lawrence. Normalizing flows for the real-time sign problem. In *38th International Symposium on Lattice Field Theory*, 12 2021.

[116] P. E. Gibbs. Lattice Monte Carlo Simulations of QCD at Finite Baryonic Density. *Phys. Lett. B*, 182:369–372, 1986.

[117] Matthias Troyer and Uwe-Jens Wiese. Computational complexity and fundamental limitations to fermionic quantum Monte Carlo simulations. *Phys. Rev. Lett.*, 94:170201, 2005.

[118] Gert Aarts. Introductory lectures on lattice QCD at nonzero baryon number. *Journal of Physics: Conference Series*, 706:022004, apr 2016.

[119] Z. Fodor and S. D. Katz. A New method to study lattice QCD at finite temperature and chemical potential. *Phys. Lett. B*, 534:87–92, 2002.

[120] Gert Aarts and Ion-Olimpiu Stamatescu. Stochastic quantization at finite chemical potential. *JHEP*, 09:018, 2008.

[121] Kurt Langfeld and Biagio Lucini. Form the density-of-states method to finite density quantum field theory. *Acta Phys. Polon. Supp.*, 9:503–514, 2016.

[122] Andrei Alexandru, Manfried Faber, Ivan Horvath, and Keh-Fei Liu. Lattice QCD at finite density via a new canonical approach. *Phys. Rev. D*, 72:114513, 2005.

[123] Philippe de Forcrand and Slavo Kratochvila. Finite density QCD with a canonical approach. *Nucl. Phys. B Proc. Suppl.*, 153:62–67, 2006.

[124] Shailesh Chandrasekharan. Fermion Bag Approach to Fermion Sign Problems. *Eur. Phys. J. A*, 49:90, 2013.

[125] Philippe de Forcrand and Owe Philipsen. The Chiral critical line of N(f) = 2+1 QCD at zero and non-zero baryon density. *JHEP*, 01:077, 2007.

[126] Scott Lawrence. Perturbative Removal of a Sign Problem. *Phys. Rev. D*, 102(9):094504, 2020.

[127] Marco Cristoforetti, Francesco Di Renzo, and Luigi Scorzato. New approach to the sign problem in quantum field theories: High density QCD on a Lefschetz thimble. *Phys. Rev. D*, 86:074506, 2012.

[128] Marco Cristoforetti, Francesco Di Renzo, Abhishek Mukherjee, and Luigi Scorzato. Monte Carlo simulations on the Lefschetz thimble: Taming the sign problem. *Phys. Rev. D*, 88(5):051501, 2013.

[129] M. Cristoforetti, F. Di Renzo, A. Mukherjee, and L. Scorzato. Quantum field theories on the Lefschetz thimble. *PoS*, LATTICE2013:197, 2014.

[130] Luigi Scorzato. The Lefschetz thimble and the sign problem. *PoS*, LATTICE2015:016, 2016.

[131] Andrei Alexandru, Gokce Basar, Paulo F. Bedaque, Gregory W. Ridgway, and Neill C. Warrington. Sign problem and Monte Carlo calculations beyond Lefschetz thimbles. *JHEP*, 05:053, 2016.

[132] Andrei Alexandru, Gokce Basar, Paulo Bedaque, Gregory W. Ridgway, and Neill C. Warrington. Study of symmetry breaking in a relativistic Bose gas using the contraction algorithm. *Phys. Rev. D*, 94(4):045017, 2016.

[133] Jun Nishimura and Shinji Shimasaki. Combining the complex Langevin method and the generalized Lefschetz-thimble method. *JHEP*, 06:023, 2017.

[134] Andrei Alexandru, Gokce Basar, Paulo F. Bedaque, Gregory W. Ridgway, and Neill C. Warrington. Monte Carlo calculations of the finite density Thirring model. *Phys. Rev. D*, 95(1):014502, 2017.

[135] Masafumi Fukuma and Naoya Umeda. Parallel tempering algorithm for integration over Lefschetz thimbles. *PTEP*, 2017(7):073B01, 2017.

[136] Andrei Alexandru, Gokce Basar, Paulo F. Bedaque, and Neill C. Warrington. Tempered transitions between thimbles. *Phys. Rev. D*, 96(3):034513, 2017.

[137] Andrei Alexandru, Gokce Basar, Paulo F. Bedaque, Sohan Vartak, and Neill C. Warrington. Monte Carlo Study of Real Time Dynamics on the Lattice. *Phys. Rev. Lett.*, 117(8):081602, 2016.

[138] Andrei Alexandru, Gokce Basar, Paulo F. Bedaque, and Gregory W. Ridgway. Schwinger-Keldysh formalism on the lattice: A faster algorithm and its application to field theory. *Phys. Rev. D*, 95(11):114501, 2017.

[139] Andrei Alexandru, Gökçe Başar, Paulo F. Bedaque, Henry Lamm, and Scott Lawrence. Finite Density QED_{1+1} Near Lefschetz Thimbles. *Phys. Rev. D*, 98(3):034506, 2018.

[140] Andrei Alexandru, Paulo F. Bedaque, Henry Lamm, and Scott Lawrence. Deep Learning Beyond Lefschetz Thimbles. *Phys. Rev. D*, 96(9):094505, 2017.

[141] Andrei Alexandru, Paulo F. Bedaque, Henry Lamm, and Scott Lawrence. Finite-Density Monte Carlo Calculations on Sign-Optimized Manifolds. *Phys. Rev. D*, 97(9):094510, 2018.

[142] Yuto Mori, Kouji Kashiwa, and Akira Ohnishi. Toward solving the sign problem with path optimization method. *Phys. Rev. D*, 96(11):111501, 2017.

[143] Andrei Alexandru, Paulo F. Bedaque, Henry Lamm, Scott Lawrence, and Neill C. Warrington. Fermions at Finite Density in 2+1 Dimensions with Sign-Optimized Manifolds. *Phys. Rev. Lett.*, 121(19):191602, 2018.

[144] Scott Lawrence. Beyond Thimbles: Sign-Optimized Manifolds for Finite Density. *PoS*, LATTICE2018:149, 2018.

[145] Cédric Villani. *Topics in optimal transportation*. Number 58. American Mathematical Soc., 2003.

[146] M. S. Albergo, G. Kanwar, and P. E. Shanahan. Flow-based generative models for Markov chain Monte Carlo in lattice field theory. *Phys. Rev. D*, 100(3):034515, 2019.

[147] Gurtej Kanwar, Michael S. Albergo, Denis Boyda, Kyle Cranmer, Daniel C. Hackett, Sébastien Racanière, Danilo Jimenez Rezende, and Phiala E. Shanahan. Equivariant flow-based sampling for lattice gauge theory. *Phys. Rev. Lett.*, 125(12):121601, 2020.

[148] Denis Boyda, Gurtej Kanwar, Sébastien Racanière, Danilo Jimenez Rezende, Michael S. Albergo, Kyle Cranmer, Daniel C. Hackett, and Phiala E. Shanahan. Sampling using $SU(N)$ gauge equivariant flows. *Phys. Rev. D*, 103(7):074504, 2021.

[149] Kim A. Nicoli, Shinichi Nakajima, Nils Strodthoff, Wojciech Samek, Klaus-Robert Müller, and Pan Kessel. Asymptotically unbiased estimation of physical observables with neural samplers. *Phys. Rev. E*, 101(2):023304, 2020.

[150] Kim A. Nicoli, Christopher J. Anders, Lena Funcke, Tobias Hartung, Karl Jansen, Pan Kessel, Shinichi Nakajima, and Paolo Stornati. Estimation of Thermodynamic Observables in Lattice Field Theories with Deep Generative Models. *Phys. Rev. Lett.*, 126(3):032001, 2021.